Dimming and brightening in observations and CMIP6

Investigation of surface solar radiation variations from 1961 to 2014, focusing on the effects of cloud cover and aerosol emissions.

Ingeborg Rian Julsrud

Thesis submitted for the degree of
Master in Meteorology and Oceanography
60 credits

Department of Geosciences
Faculty of mathematics and natural sciences

UNIVERSITY OF OSLO

Autumn 2020

Dimming and brightening in observations and CMIP6

Investigation of surface solar radiation variations from 1961 to 2014, focusing on the effects of cloud cover and aerosol emissions.

Ingeborg Rian Julsrud

Dimming and brightening in observations and CMIP6

http://www.duo.uio.no/

Printed: Reprosentralen, University of Oslo

Abstract

Periods of *dimming* and *brightening* are observed in incoming solar radiation at the Earth's surface (surface solar radiation, SSR) between the mid-20th century and present day. Many atmospheric components affect SSR, including aerosols and clouds, and observational studies disagree somewhat in their conclusions about the relative effect of each component in different regions. In addition, current Earth System Models (ESMs) are unable to simulate the extent of global dimming/brightening, which raises doubts about ESM projections for the future. In this thesis, an investigation has been conducted to uncover the relative effects of changes in cloud cover and aerosol emissions on SSR trends between 1961 and 2014. The regions studied are China, Japan, Europe and the United States. In this effort, observational data sets from GEBA, CRU TS and ISCCP and emission data from CEDS have been compared and analyzed. An effort has been made to separate the effects of cloud cover variations from the observed all-sky SSR by calculating a cloud-free version of SSR dubbed "no-cloud SSR". Historical model runs from 42 ESMs participating in CMIP6 have also been studied and compared.

The main findings are: The calculated "no-cloud" SSR data indicates that certain apparent trends exhibited by GEBA are almost completely masked by cloud cover, namely a renewed dimming in China, Japan and Europe after 2000, and a brightening in the United States after 1995. Summed anthropogenic aerosol emission trends are found to be in anticorrelation with the observed no-cloud SSR trends in all regions except Europe during initial dimming periods, suggesting aerosols as the main cause of dimming. In relation to subsequent brightening trends, the effects of individual aerosol/precursor species' contributions are proposed as causal, most notably black and organic carbon. It is also found that ESMs are able to simulate dimming and

brightening in Europe reasonably well, but they remain unable to reproduce the magnitude of observed SSR trends in China, Japan and the United States. The apparent effect of aerosol emissions on SSR is computed from observations and ESM output, and is found to be much larger – relative to observations – over Europe than in the other three regions.

Contents

Acknowledgements

First of all, I would like to thank my supervisors, Trude Storelvmo (University of Oslo) and Michael Schulz (MET Norway), for the opportunity to work on this thesis and for help along the way. Many thanks, also, to Kine Onsum Moseid (MET Norway), for constructive criticism and invaluable advice during my thesis work. Furthermore, I am extremely grateful to Martin Wild (ETH Zürich) for prompt, thorough email replies regarding all things dimming and brightening, and to Ian Harris (University of East Anglia) for helping me understand the cloud data I have used. I would also like to acknowledge helpful email correspondence with Liu Yawen (Nanjing University) and Robert Giseke (Potsdam Institute for Climate Impact Research). In addition, I must mention the technical assistance I, and many others at MetOs, have been provided with by Johannes Tobiassen Langvatn.

Finally, I gratefully acknowledge the enlightening discussions I have had with my father, Stein Julsrud – whose knowledge is unparalleled – and I am also deeply indebted to my entire family for unrelenting support during the past two years.

Ingeborg Rian Julsrud

November 2020

Romedal

Chapter 1

Introduction

1.1 Motivation

Solar radiation propagates through the entire atmosphere before it reaches the Earth's surface, and interacts with a range of different gases and particles along its path. Many atmospheric constituents absorb and/or scatter radiation within certain wavelength ranges, and therefore the solar radiation reaching the ground is a fraction of the radiation that enters the top of the atmosphere. While around 340 W/m² enter the atmosphere on average globally, the amount that is left when it reaches the surface is only around 185 W/m² (Wild, Folini, Schär et al. 2013). However, these are global averages of values that largely vary between different regions, seasons and of course throughout the diurnal cycle.

Since the middle of the 20th century, large changes in the incoming solar radiation at the surface have been observed globally (Wild 2016). For the period 1950-1980, a widespread decrease in surface solar radiation (SSR) of on average about 4 W/m² was documented, now often referred to as "global dimming" (Wild 2012). Since the 1980s, a regionally dependent slight increase in SSR has followed, aptly termed "brightening" (Wild, Gilgen et al. 2005). Still, in some regions, the dimming period has continued (Wild 2012).

Some evidence suggests that trends in observed SSR during the dimming period were generally caused by changes in aerosol concentration in the atmosphere – meaning

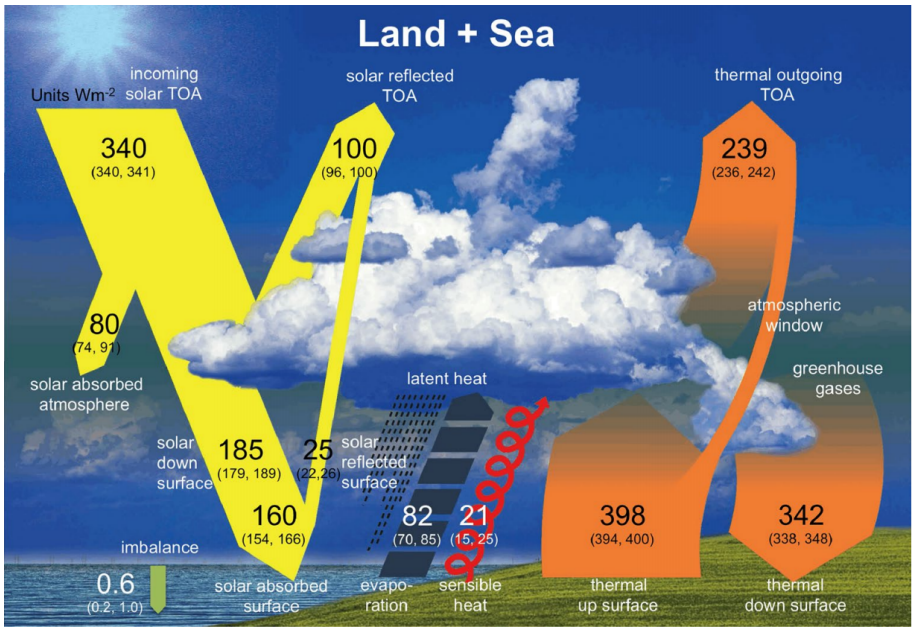

Figure 1.1: Schematic diagram of the global mean energy balance of the Earth. Numbers indicate estimates of the magnitudes of globally averaged energy balance components during the beginning of the 21st century, together with their uncertainty ranges. Units are W/m². From Wild, Folini, Hakuba et al. 2015.

SSR decreased with increasing amounts of aerosols (Wild 2012 and references therein). Other evidence suggests that cloud cover variations independent of aerosol presence have played a crucial role in the SSR trends regionally (e.g. Norris and Wild 2009; Pfeifroth et al. 2018; Long et al. 2009). No consensus has been reached on the relative roles of clouds, aerosols and other mechanisms in the causation of the SSR trends (Wild 2016).

Regardless of the mechanisms responsible, dimming and brightening have, indeed, been observed (Wild 2016). However, Earth System Models (ESMs) have not been able to reproduce the magnitude of the observed SSR trends (Allen, Norris and Wild 2013; Storelvmo et al. 2018; Moseid et al. 2020). Since variations in SSR have effects on the Earth's energy budget and a variety of atmospheric processes, it is vital to understand why the ESMs cannot reproduce observed variations in SSR. Furthermore, this ESM shortcoming raises doubts about ESM projections for future climate change, which can have substantial consequences, because these projections serve as the scientific basis of wide-reaching political decision making (Juckes et al. 2020).

To understand why ESMs are unable to reproduce the observed trends, it is essential

to understand which atmospheric components interact with solar radiation. Relevant atmospheric components in this regard are the extinction agents in the atmosphere – meaning all atmospheric components that either scatter or absorb solar radiation. Figure 1.1 illustrates the various components that interact with radiation throughout the Earth-atmosphere system. Examples of these are ozone, water vapor, clouds and aerosols. The latter two components – clouds and aerosols – are highly important.

Clouds are the Earth's most effective shield against sunlight. Clouds scatter and reflect solar radiation, and on average globally, about 30% of incoming solar radiation is blocked by clouds (NASA 1999). Locally, cloud cover variations are large. With cyclones and convective activity come more cloud cover and lower SSR, but for long-term trends in SSR to be caused by cloud cover, there must also be long-term trends in cloud cover. Such cloud cover trends have been observed regionally as a result of climate change, but the trends are different in both sign and magnitude across different regions (Norris, Allen et al. 2016).

Aerosols represent another atmospheric component that can have a substantial effect on the radiative transmissivity of the atmosphere (Wild 2016). Aerosols enter the atmosphere as a result of both natural and anthropogenic emissions. Some aerosols are fully formed upon emission, while others form after emission, upon reacting with other atmospheric components. The emissions leading to the latter type are called aerosol precursors. In this thesis, anthropogenic emissions of aerosols and aerosol precursors are studied. Important emissions in this regard are SO_2 (precursor), NH_3 (precursor), black carbon (aerosol), organic carbon (aerosol), NO_x (precursor) and NMVOC (precursor) (Boucher et al. 2013; Myhre, Myhre et al. 2013). The global emissions of aerosols and aerosol precursors have changed substantially during the dimming and brightening periods (Wild 2012), but the timelines are different in different regions (Streets, Wu and Chin 2006).

To make things more complicated: In addition to clouds and aerosols being independent factors that affect SSR, they also interact with each other (Boucher 2015). Specifically, clouds' optical properties and lifetimes can change drastically because of aerosols, and an aerosol's lifetime can be affected upon interaction with a cloud.

This complicated picture results in high uncertainty tied to aerosols and clouds in

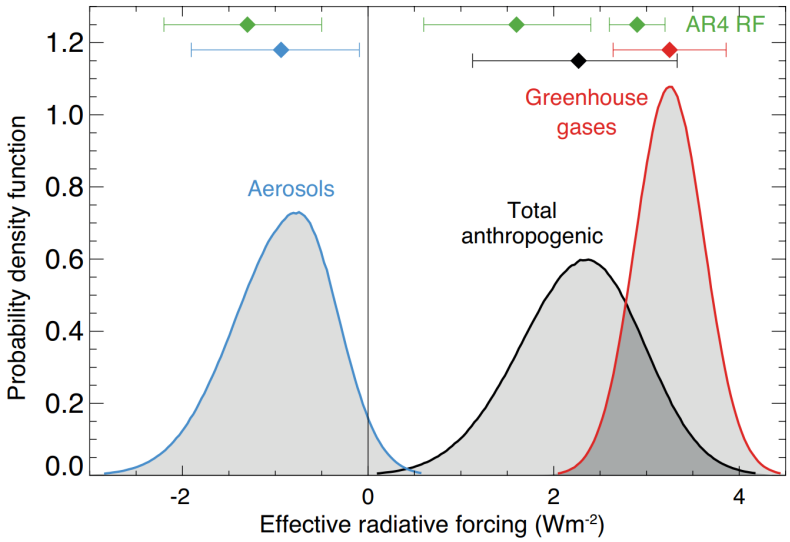

Figure 1.2: Probability density function (PDF) of "effective radiative forcing" due to greenhouse gases, aerosol forcing and total anthropogenic forcing, according to IPCC Assessment Report 5. The effective radiative forcing quantifies the increase in energy into the Earth system due to these components, after allowing the system to adjust. The effective radiative forcing due to aerosols include the contribution from aerosols' effects on clouds. From Myhre, Shindell et al. 2013.

ESM projections. According to the 5^{th} Assessment Report from the Intergovernmental Panel on Climate Change (IPCC), aerosols and clouds continue to contribute the largest uncertainty to modeling of the Earth's changing energy budget (Boucher et al. 2013). This is because their respective effects on the radiative budget are highly important, while their properties vary at scales significantly smaller than those resolved in climate models. Their interactions are also quite nuanced (Boucher et al. 2013). Figure 1.2 is a well-known figure from the IPCC's 5^{th} Assessment Report, which illustrates the uncertainty of the estimate of the total radiative effects of anthropogenic aerosols as well as its effect on the ability of ESMs to estimate total anthropogenic effect on the Earth's climate. This uncertainty is especially important when considering the potential climate effects of reducing aerosol emissions, since aerosols have – and continue to – offset global warming due to greenhouse gases (Hansen et al. 2011).

1.2 Research questions

The main question that is addressed in this thesis is: How did clouds and aerosol emissions affect trends in SSR during the second half of the twentieth century and into the twenty-first? The aim is to advance the understanding of the causes behind dimming and brightening and to understand the bias between modelled SSR and observed SSR. Since dimming and brightening has been studied by many, it is necessary to clearly state what this thesis brings to the table that has not been done in previously published work.

The following research questions are addressed in this thesis:

- How did cloud cover affect SSR in the period 1961-2014?
- How did aerosol emissions affect SSR in the period 1961-2014?
- How well do ESM simulations reproduce SSR trends found in observations, and what are possible causes of bias?

The following tasks have been performed regionally to answer the above questions:

1. Computation and analysis of observed SSR without the contribution from cloud cover variations (dubbed "no-cloud SSR"), compared to observed all-sky SSR.
2. Analysis of changes in the no-cloud SSR data introduced in the first point, compared to changes in aerosol emissions.
3. Analysis of changes in ESM simulations of SSR compared to observations.
4. Computation and analysis of no-cloud SSR from simulations, compared to simulated clear-sky and all-sky SSR.
5. Analysis of changes in simulated SSR compared to input aerosol emissions.
6. Computation and comparison of "apparent effects" of aerosol emissions on no-cloud SSR in observations and simulations.

1.3 Thesis layout

The layout of the rest of the thesis is as follows: The second chapter summarizes the theoretical basis on which this thesis is founded, and it is followed by an updated review of the scientific literature on global dimming and brightening in the third chapter. The fourth chapter introduces the datasets used and describes the methodology of the analysis conducted. The fifth chapter contains results and discussion, and the final chapter summarizes and suggests further research related to the present work.

Chapter 2

Theory

This chapter provides the theoretical basis on which this study is founded, and largely adopts terminology described and used in Olivier Boucher's textbook "Atmospheric Aerosols" (Boucher 2015) and Dennis L. Hartmann's textbook "Global Physical Climatology" (Hartmann 1994).

2.1 Radiative transfer in the atmosphere

The Earth's climate system is ultimately controlled by the energy that enters and the energy that leaves the system. The difference between these two energy fluxes is generally referred to as the radiative balance between the Earth and space.

A radiative balance of zero is necessary to keep the Earth's climate in steady state. Should the radiative balance become non-zero, the temperature of the Earth's surface will change until the system reaches a new steady state. The energy budget is a function of many different variables, both internal and external to the Earth system. Most of the variables are constantly changing. Therefore, the radiative balance and the temperature of the Earth are also constantly changing.

One of the most important variables in the radiative budget is solar irradiance - that is, the amount of sunlight received from the Sun. Indeed, the magnitude of the solar irradiance governs how much energy enters the atmosphere at any given moment.

However, the top of the atmosphere contains very little matter, and therefore this is

not where the Earth largely absorbs solar radiation. Most of the Earth's absorption of solar radiation occurs at the surface, and therefore the solar irradiance at the surface is a very important quantity. Within this thesis, the solar irradiance at the surface will usually be abbreviated SSR (acronym for "surface solar radiation").

Unlike solar irradiance at the top of the atmosphere, SSR is not controlled solely by the Sun's output: Factors internal to the atmosphere are highly important, specifically factors that control atmospheric extinction (Hartmann 1994). Here, extinction refers to the fraction of electromagnetic radiation which is scattered or absorbed on its way through the atmosphere (Hartmann 1994). When the extinction of the atmosphere increases, SSR decreases, and vice versa. The extinction is caused by all atmospheric constituents that are radiatively active in the shortwave spectrum; that is, components which interact with solar radiation on its way down (Hartmann 1994).

All media have an extinction coefficient β_{ext}, where the extinction refers to the total depletion of incident radiation through the medium, including both absorption and scattering. In the case of atmospheric extinction, the medium is all the gases and particles through which the radiation propagates. The extinction coefficient β_{ext} is governed by the density, sizes and optical properties of the particles through which the radiation passes, and can be defined as the product of the particle number concentration and the extinction cross section.

If the vertical slab of medium through which the radiation passes is dz, the extinction α will be $\alpha = \beta_{ext} dz$. Now, integrating the extinction throughout a vertical atmospheric column (from z_{toa} to z_{surf}), the result is the atmospheric *optical depth*, τ:

$$\tau = \int_{z_{surf}}^{z_{toa}} \beta_{ext} dz \tag{2.1}$$

The infinitesimal change in τ in the vertical can be stated as the negative of the extinction α, because τ decreases as the height of the column above decreases (which happens when z increases):

$$d\tau = -\beta_{ext} dz \tag{2.2}$$

It has now been determined that optical depth is the extinction of radiation throughout a vertical atmospheric column. The next task is to define SSR in terms of optical depth.

SSR is the radiation reaching a specific point on the surface of the Earth, but includes radiation from all directions. If incident radiation at some coordinate s is denoted E, then the amount of radiation depleted through an infinitesimal distance ds (may be vertical or slanted, depending on the angle of incident radiation) can be stated in terms of the extinction coefficient β_{ext}:

$$dE = -\beta_{ext} E ds \tag{2.3}$$

Now, Equation 2.3 does not differentiate between different angles of incident radiation. However, optical depth is strictly defined as the extinction throughout a *vertical* atmospheric column. Since the goal is to define SSR in terms of *optical depth*, the equation must be restated using the vertical infinitesimal slice dz. Using some trigonometric intuition, Equation 2.3 can be stated in terms of a zenith angle ϕ and dz ($ds = dz/(-\cos\phi)$):

$$dE = \beta_{ext} E \frac{dz}{\cos\phi} \tag{2.4}$$

As stated in Equation 2.2, the infinitesimal optical depth is defined in terms of the extinction coefficient and dz, meaning it can be substituted into Equation 2.4:

$$dE = -E \frac{d\tau}{\cos\phi} \tag{2.5}$$

Equation 2.5 can now be solved for the atmospheric column between z_{surf} and z_{toa}. The resulting model of SSR (E_{surf}) is called the *Beer-Lambert law* (Swinehart 1962):

$$\begin{aligned}
\frac{1}{E} dE &= -\frac{1}{\cos\phi} d\tau \\
\implies \int_{z_{toa}}^{z_{surf}} \frac{1}{E} dE &= -\frac{1}{\cos\phi} \int_{z_{toa}}^{z_{surf}} d\tau \\
\implies \ln \frac{E_{z_{surf}}}{E_{toa}} &= -\frac{1}{\cos\phi} \tau \\
\implies E_{surf} = E_{toa} \exp(-\frac{\tau}{|\cos\phi|}) &\quad \textbf{Beer-Lambert law}
\end{aligned} \tag{2.6}$$

To repeat, E_{surf} denotes SSR, E_{toa} denotes solar irradiance at the top of the atmosphere, τ denotes atmospheric optical depth and ϕ denotes solar zenith angle.

Of course, the atmosphere is made up of a range of different components that interact with the radiation, which makes optical depth a composite parameter. Assuming optical depth to be additive (Boucher 2015), the optical depth can be expressed as the sum of a handful of atmospheric extinction properties. For instance, the following components can be assumed responsible for all atmospheric extinction: Rayleigh scattering (scattering by air molecules, τ_T), permanent gas absorption (absorption by permanent gases such as CH_4 and CO_2, τ_g), ozone absorption (τ_o), absorption by water vapor (τ_w), absorption/scattering by atmospheric aerosols (τ_a) and absorption/scattering by cloud components (τ_c) (Leckner 1978). Following that assumption, E_{surf} can be stated in terms of all the their respective optical depths:

$$\begin{aligned} E_{surf} &= E_{toa} \exp(-(\tau_T + \tau_g + \tau_o + \tau_a + \tau_c)/\cos\phi) \\ &= E_{toa} \exp((-\tau_T - \tau_g - \tau_o - \tau_a - \tau_c)/\cos\phi) \end{aligned} \tag{2.7}$$

2.2 Cloud effects on SSR

Clouds are collections of suspended liquid or solid water particles in the atmosphere. They can exist within the lowest three layers of the Earth's atmosphere – in the troposphere, the stratosphere and the mesosphere – but only tropospheric clouds have relevance for the Earth's radiative budget. Both liquid and solid water particles interact with solar radiation, and several cloud properties affect the degree to which radiation will be subject to extinction from a cloud. Especially important are the cloud's density, particle shapes and sizes and the ratio of water to ice particles in the cloud (Hartmann 1994):

- With higher cloud density, the extinction of radiation increases due to scattering and absorption (Hartmann 1994), and can cause lower SSR. However, at a certain density level, a continued increase in density will not further affect SSR (Hartmann 1994).
- Because of higher surface area, smaller particles scatter more radiation than

larger ones, assuming the same mass amount of water or ice (Hartmann 1994). Thus, smaller cloud particles can cause lower SSR.

- Solid ice cloud particles tend to be larger and less numerous than their liquid counterparts, meaning more ice particles lead to lower extinction (Mitchell, Senior and Ingram 1989). Thus, a higher fraction of water to ice in a cloud can cause lower SSR.

In conclusion, the effect of clouds on SSR is nuanced and depends on many cloud properties. Therefore, even though it is clear that SSR is subject to extinction by clouds, the relationship between cloud cover and SSR is not simple, and it depends on the specific cloud cover's optical properties.

2.3 Aerosol effects on SSR

Atmospheric aerosols are particles of condensed matter suspended in the atmosphere. The particles can be liquid or solid - or a mix of the two phases. Examples of aerosol types in the atmosphere are mineral dust, soot and sulphuric acid. Strictly, cloud particles are also aerosols, but they are generally not referred to as such. Aerosols stem from a range of different sources, both natural and anthropogenic, and what they all have in common is a relatively low mass, which allows for suspension in the atmosphere's gas mixture. Of course, aerosol mass varies between different aerosol species, and this is an important factor determining a certain aerosol species' atmospheric *residence time*. The residence time is the average time an aerosol species remains suspended before somehow being removed from the atmosphere (discussed further in 2.3.1).

The aerosols' presence affects the climate of the Earth by altering the radiative budget in different ways. Changes in aerosol amounts have direct effects on the incoming radiation, but can also alter the optical properties of other components in the Earth system, such as clouds. Each of these mechanisms have an effect on SSR, meaning they alter the amount of radiation reaching the Earth's surface.

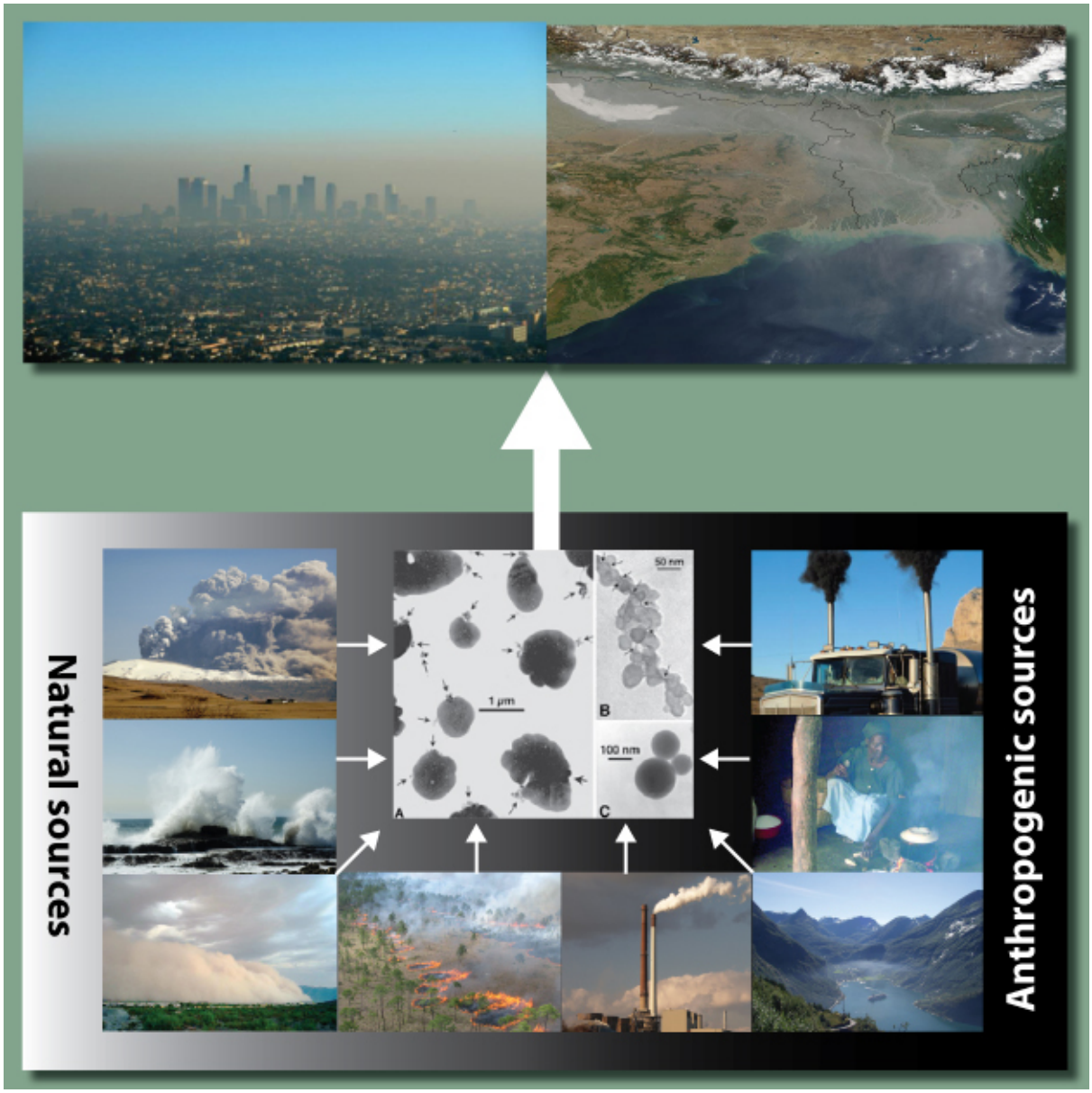

Figure 2.1: Illustration indicating sources and appearance of atmospheric aerosols. Top: local and large scale air pollution. Sources include (bottom, counterclockwise) volcanic eruptions, sea spray, desert storms, savannah biomass burning, coal power plants, ships, cooking and road transport. Center: Electron microscope images of (A) sulphates, (B) soot, (C) fly ash, a product of coal combustion. © 2013 Nature Education Images. All rights reserved. Source: Myhre, Myhre et al. 2013.

Species	Tropospheric residence time
Sulphate	∼1 week
Black carbon (BC)	1 week to 10 days
NO_3	∼1 week
Organic aerosol	∼1 week

Table 2.1: Residence times in the troposphere of important anthropogenic aerosol species. The estimated residence times are derived from simulations in AeroCom models. Source: Boucher et al. 2013

2.3.1 Aerosol residence time

An important concept to introduce when considering interactions between aerosols and radiation, is the concept of *residence time*, which is defined as the average amount of time an aerosol spends in the atmosphere, or:

$$T_{res} = B/S = B/R, \tag{2.8}$$

where B is the vertically integrated aerosol concentration, S is the aerosol source flux and R is the aerosol removal flux (Boucher 2015). According to Boucher 2015, residence time is different from the concept of atmospheric *lifetime* in that residence time is a property that holds only in a reservoir that is sufficiently large that advection in and out of the reservoir can be considered negligible compared to sources and sinks within the reservoir. It should be noted that many publications use these two terms interchangeably.

Sources of aerosols are both natural and anthropogenic, with volcanic eruptions, sea spray, desert sand swiveled up by wind and wildfire emissions representing some natural sources, and anthropogenic biomass burning, coal power plants and cooking representing some anthropogenic ones. Figure 2.1 illustrates this paragraph, with images of many different sources of atmospheric aerosols.

Sinks of aerosols are, most importantly, dry deposition, such as sedimentation under gravity, and wet deposition, which occurs when aerosols fall to the ground with rain drops. The smallest and largest aerosols have residence times of hours to days, while

the bulk of the aerosols in the intermediate size range have residence times on the scale of days to 1-2 weeks (Boucher 2015).

What determines residence time is complicated, because it includes many aspects of aerosol properties. Most obviously, the size and weight of aerosols are highly important in determining the residence time as a function of dry deposition. However, the problem is much more complex, as many other aerosol properties also play a part in an aerosol's residence time. For instance, an aerosol's hygroscopicity (the tendency of a solid aerosol particle to absorb moisture from its surroundings) is important for determining the potential for wet deposition. Table 2.1 shows some important aerosol residence times.

2.3.2 Aerosol-radiation interactions (ARI)

Aerosols affect the incoming solar radiation directly through what is often called aerosol-radiation interactions (ARI): aerosol scattering or absorption of solar radiation on its way through the atmosphere.

Scattering is an umbrella term for particle interaction with a ray's direction of propagation. A ray incident on an aerosol surface may be reflected, refracted or diffracted, depending on the aerosol geometry and composition. In this way, when radiation is incident on a population of aerosols, a fraction of the radiation will be sent right back out to space.

Some aerosols absorb solar radiation. Examples of aerosols that absorb solar radiation to a significant degree are black carbon (soot) and dust particles. When aerosols absorb the solar radiation, they convert some of the shortwave radiation to heat and thereby reduce the amount of solar radiation reaching the surface. This conversion to heat has other potential consequences related to the radiation budget, described in Section 2.3.4. But the direct effect of ARI is a reduced SSR.

2.3.3 Aerosol-cloud interactions (ACI)

Aerosols also affect radiation indirectly through cloud changes: Aerosols act as cloud condensation nuclei upon which water vapor can condense and form cloud droplets,

and their presence affects cloud radiative properties. Such aerosol-cloud interactions (ACI) may cause both an increase and a decrease in SSR, making the picture more complicated than that of ARI. Two kinds of ACI are described in Boucher 2015:

- Assuming the cloud contains a set amount of moisture, the presence of aerosols reduces the average size of cloud droplets in the cloud by increasing the number of them. This ACI was first described by Sean Twomey (Twomey 1977), and is therefore often referred to as the Twomey effect. This effect causes an enhancement of scattering, and reduces SSR.
- Some aerosols can also act as ice-nucleating particles in mixed-phase clouds. An increase in ice-nucleating particles can lead to rapid glaciation of supercooled droplets, causing a quickened hydrometeor growth in the cloud. This quickened growth of relatively few hydrometeors happens due to the difference between saturation vapor pressure over ice as opposed to over water (Lamb and Verlinde 2011). This, in turn, may lead to precipitation, and can thereby quickly turn a non-precipitating cloud into a precipitating one. This could lead to reduced cloud cover and thus an increase in SSR. It should be noted that only a small fraction of aerosols can act as ice nuclei, namely ones that have or can enable a crystalline structure. Examples of such aerosols are dust particles and possibly some black carbon aerosols (Boucher 2015).

2.3.4 Rapid adjustments

The state of the atmosphere in terms of its temperature profile, cloud amount and humidity is fundamental to the Earth's radiative balance. Alterations to these basic properties, therefore, are termed rapid adjustments. Rapid adjustments are not instantaneous effects on the radiative budget, but they modify the radiative budget indirectly through quick atmospheric and surface changes (Boucher et al. 2013). Aerosols can induce several different rapid adjustments:

- Aerosols that largely absorb radiation, such as black carbon, can alter the thermal profile of the atmosphere by locally heating it. However, such alterations can have both positive and negative effects on SSR:
  - Aerosol absorption inside of a cloud layer may heat the air and promote

cloud evaporation, and can thereby cause an increase in SSR (Boucher 2015).

  - An alteration of the thermal profile could also enhance convection through changing the stability of the atmosphere, and thereby may enhance cloud formation (Koch and Del Genio 2010). This effect would cause a decrease in SSR.

- Aerosols may also impact cloud evolution by acting as cloud condensation nuclei. An increase in cloud condensation nuclei can increase the number of cloud droplets and thereby reduce droplet size (Boucher 2015). A reduction in droplet size delays precipitation, and this may cause a decrease in SSR.

Chapter 3

Background and literature review

There already exists a large body of research literature regarding dimming and brightening. This chapter provides an overview of existing literature discussing these subjects. The chapter also attempts to cover disputed areas of study within the field, creating a nuanced picture of the current state of understanding regarding global dimming and brightening. The purpose is to set the stage for the results in this thesis.

Martin Wild's 2012 review "Enlightening Global Dimming and Brightening" (Wild 2012) summarizes the literature on global dimming and brightening up until then. In 2016, he published a follow-up review, "Decadal changes in radiative fluxes at land and ocean surfaces and their relevance for global warming" (Wild 2016). Much of this chapter's contents are inspired by Wild's work.

3.1 Observations: Global dimming and brightening

During the second half of the 20th century, measurements of incoming solar radiation (SSR) exhibited substantial variations in large parts of the world. Ground-based radiometers and sun photometers globally measured large decreases in SSR between the 1950s and the 1980s (Wild 2009).

The discovery of declining SSR trends was initially published in a Europe-focused extended abstract for the 1988 International Radiation Symposium (Ohmura and Lang 1989). Figure 3.1 shows an SSR timeseries from Stockholm, Sweden, which may be

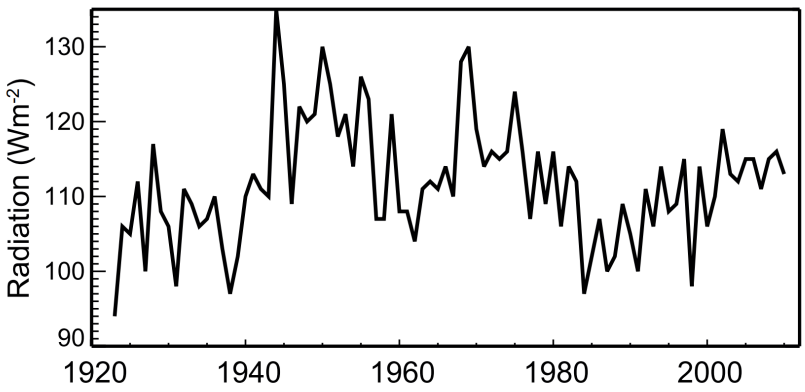

Figure 3.1: Annual mean SSR observed in Stockholm, Sweden, between 1923 to 2010 – the longest SSR record available worldwide. The timeseries shows that Stockholm experienced dimming between the 1950s and the 1980s and a subsequent brightening, and this timeline is generally representative for the European SSR trends in this period. The timeseries also exhibits an "early brightening" from the late 1930s, but this trend is not investigated in this thesis. From: Hartmann et al. 2013

seen as representative of the general SSR trend in large parts of Europe. Throughout the 1990s, many studies were published regarding declining trends in other parts of the world (e.g. Russak 1990; Stanhill and Moreshet 1994; Stanhill and Kalma 1995; Abakumova et al. 1996), and soon the term "global dimming" was coined for the reduction in SSR after the 1950s (Stanhill and Cohen 2001).

It should be noted that the label “global” in global dimming originally did not refer to the global scale at which the SSR reduction was happening, but was rather coined as a shortened version of the technical term "global radiation dimming", where global radiation refers to the sum of direct and diffuse radiation (Wild 2009). However, it is unclear whether all literature uses "global dimming" to refer to this technical term or the global scale of dimming, since it is not always explicitly stated (Wild 2020). For clarity in the rest of this thesis, global dimming will be called simply "dimming".

Both regional and global studies have been published since the discovery of dimming. As quoted in Chapter 1 the overall dimming between the 1950s and the 1980s has been approximated to be a reduction in SSR of about 4 W/m^2 (Wild 2012).

Since the 1980s, the SSR trend has reversed in some parts of the world, namely Europe, North America and some parts of Asia, and this reversal trend has been termed

"brightening" (Wild 2012). Still, in other regions, the dimming period continued for longer, e.g. in India (Soni, Pandithurai and Pai 2016).

3.2 Solar irradiance's effects on dimming and brightening

According to Willson and Mordvinov 2003 and Hoyt and Schatten 1993, variations in the Sun's luminosity during the dimming and brightening period were not nearly substantial enough to cause the SSR trends. In other words, these papers agree that trends in E_{toa} in Equation 2.6 in this thesis (the Beer-Lambert law) could not have been the primary cause of the trend observed at the surface. This suggests that only the transmissivity components of the atmosphere are possible as main contributors to dimming, and since these components can be altered by a multitude of factors, the explanation may be quite complicated. Variations in solar irradiance are not further explored as a potential cause of dimming and brightening in this thesis.

3.3 Radiatively active gases' effects on dimming and brightening

There exist several atmospheric gases that are radiatively active in the solar radiation spectrum, prominently water vapor and ozone (O_3). This means that variations in the presence of such gases have the potential to affect SSR. However, according to Stanhill and Cohen 2001, Wild 2016 and references therein, variations in levels of these gases have not been substantial enough in the relevant period to have caused the dimming and brightening trends. As such, the effects of trends in radiatively active gases are also not further investigated in this thesis.

3.4 Aerosol and cloud effects on dimming and brightening

The previous two sections determined that changes in the Sun's luminosity and variations in the atmospheric load of radiatively active gases are here ruled out as the cause of global dimming and brightening. The components that remain possible as causes are aerosols and clouds. Because of aerosol-cloud interactions (ACI), cloud effects and aerosol effects on SSR are intertwined and difficult to study independently of each other.

A large number of observational studies have been conducted to study cloud and aerosol contributions to SSR trends. From early on, it was thought that the main cause of the wide-reaching dimming trend was extinction from increasing amounts of aerosols in the atmosphere: Stanhill and Cohen 2001, who introduced the term "global dimming", reviewed the literature on dimming that had been published in the decade beforehand, and concluded that the most likely cause of the worldwide dimming was the increase in aerosol emissions, especially due to the aerosol's enhancement of cloud optical depth through ACI. Later studies have nuanced the general picture, with regards to independent effects of cloud cover variations.

For Europe and China, Norris and Wild 2007 and Norris and Wild 2009 found that SSR trends were similar in observed all-sky and clear-sky, suggesting cloud variations could not be the cause of the trends. However, Norris and Wild 2009 found for Japan that cloud cover variations contributed substantially to Japanese SSR trends between 1971 and 2002. Stanhill, Achiman et al. 2014 found for five stations in different climate zones in Europe and Asia that changes in cloud cover rather than aerosol load were possibly the major cause of dimming and brightening at the sites studied. Parding 2014 found for Bergen, Norway, that the initial dimming trend until 1990 was caused by cloud trends, while the subsequent brightening trend was caused instead by a decrease in aerosol optical depth (AOD). However, Pfeifroth et al. 2018 studied satellite data over Europe, and concluded that the majority of the European brightening was due to cloud changes – however, not ruling out indirect effects of aerosols (ACI and rapid adjustments) as potentially causal to the relevant cloud changes. Liley 2009 found

that in New Zealand, SSR trends were consistent with variations in cloudiness. For the United States, Long et al. 2009, Augustine and Dutton 2013 and Augustine 2020 conclude that brightening between 1996 and the late 2000s is not caused primarily by aerosol changes. The latter two studies argue that, for the most part, the brightening trend is seen due to cloud cover changes.

Nonetheless, many papers also continue to substantiate the claim that the general trends are mainly due to aerosol changes. Streets, Wu and Chin 2006 studied the global, interannual changes in SSR between 1980 and 2000, and found that SSR mirrored the trend in emissions of SO_2 and black carbon. They concluded that changes in the aerosol burden due to changing patterns of anthropogenic emissions are likely contributors to the global trends in surface solar radiation. Mishchenko et al. 2007 investigated global AOD from a satellite-measured dataset between 1991 and 2005, and found the global AOD to have decreased in this period, concurrent to a global increase in SSR, suggesting the trend in AOD to have contributed to the SSR trend. One recent study also highlights the importance of variations in atmospheric absorption for the dimming and brightening trends, hinting at contributions from absorbing aerosols, especially black carbon (Schwarz et al. 2020). Other studies arguing that aerosol extinction is central to dimming and brightening trends are Zerefos et al. 2009 and Sanchez-Lorenzo et al. 2009.

In summary: Many studies appear to support the general conclusion that aerosol effects are causal to the long-term trends in SSR since the mid-20th century. However, the influence of cloud trends are still emphasized in certain studies, especially studies with regional focus. Thus, the matter is far from settled. The current literature indicates that the causes of global dimming and brightening may be quite complex.

3.5 Global dimming and brightening in ESMs

Clouds and aerosols remain two of the most uncertain components of Earth System Models (ESMs) to date (Boucher et al. 2013). The net effect of clouds and aerosols on the future climate of the Earth is highly uncertain, and not only the magnitude but also the sign of the net radiative forcing is not clear (Boucher et al. 2013). This means that ESMs do not agree on the mechanisms and effects pertaining to cloud- and aerosol

changes, which affects the accuracy of historical, present and future simulations of the Earth system.

The CMIP (Coupled Model Intercomparison Project) is a standard framework of ESM experiments, designed to compare ESM simulations and study the spread in results, based on identical input variables (Meehl et al. 2000). These experiments allow for assessment and comparison between ESMs, and can facilitate estimation of uncertainties in future projections. For study of global dimming and brightening, the *historical* experiments from CMIP are of interest. These experiments attempt to reproduce the Earth's climate between 1850 and present day. The most recent phase of CMIP is CMIP6.

Dwyer, Norris and Ruckstuhl 2010 studied 13 CMIP3 models' ability to reproduce dimming and brightening. Their study suggested that climate models uniformly underestimated aerosol effects on SSR in China and Japan, since the simulations strongly underestimated dimming and brightening trends in these two countries. Allen, Norris and Wild 2013 studied 42 CMIP5 models' simulation of historical SSR in Europe, China, India and Japan. Similarly, their study shows that none of the included models were able to reproduce the magnitude of dimming in China, India and Japan. The same is true for larger regions, according to Storelvmo et al. 2018, who studied 33 CMIP5 models' historical simulations. The models were found to exhibit little to no dimming in Asia and the Americas, and only weak brightening in Europe. The study concluded that if aerosol emissions are assumed to be the main cause behind the dimming trends seen in observations, ESMs exhibited a too-weak response to the input aerosol emissions. A recently published study by Moseid et al. 2020, investigates 8 CMIP6 models' ability to reproduce dimming and brightening, and find that the included models' historical simulations exhibit accurate SSR trends in Europe, but not in China. The paper argues that since the ESMs are able to translate emissions correctly into radiative effects in Europe, there may be issues with the accuracy of the emission inventory in China.

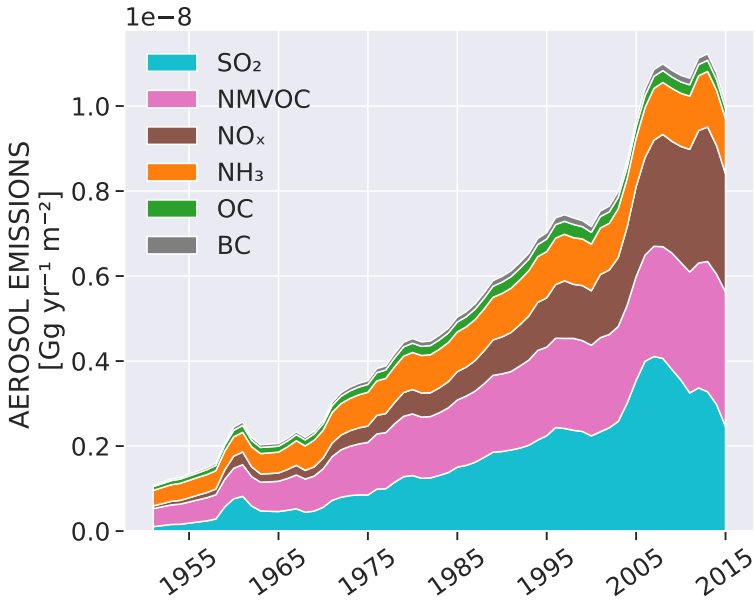

Figure 3.2: Timeseries of the anthropogenic aerosol/precursor emission history between 1950 and 2014 in China. Emissions included are: SO_2, NMVOC, NO_x, NH_3, OC and BC, and the emissions are given in gigagrams per year as a sum from the entire region, divided by the area of the region (China: 9.597×10^{12} m²). Source of data: 2020 CEDS (see Section 4.2.2 for description).

3.6 Aerosol emission histories

Along with increasing demands for energy, anthropogenic emissions of air pollutants globally increased steadily until the late 20th century. The changes in emissions are, however, different between different continents and regions, which is important to acknowledge and address when investigating causes of global dimming. To that end, this section summarizes aerosol emission histories for the regions focused on in this thesis.

3.6.1 China

Significant industrialization in China began only in the mid-20th century, after the founding of the People's Republic of China, but the process of modernizing and catching up with the industrialized Soviet Union and Western world was quick. From still being a country predominantly made up of farmers in the 1950s, China became the globally-leading industrial power (i.t.o. industrial output) in only 60 years (Huang

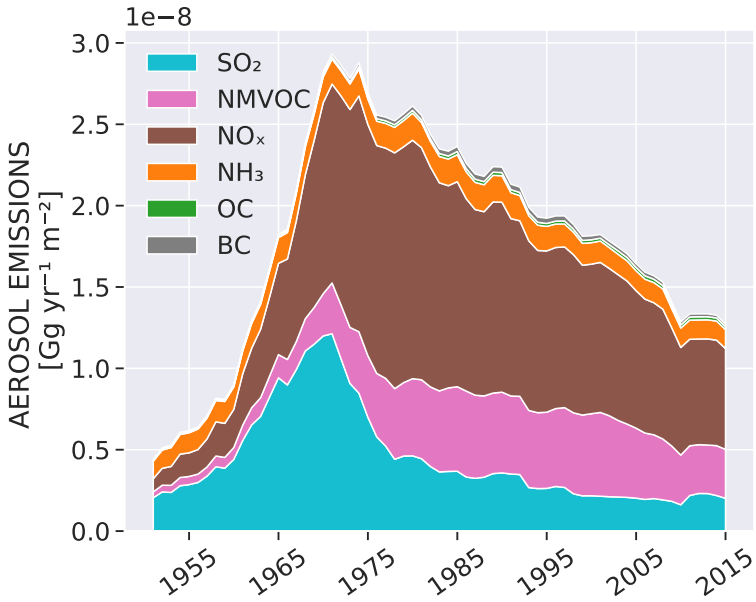

Figure 3.3: Timeseries of the anthropogenic aerosol/precursor emission history between 1950 and 2014 in Japan. Emissions included are: SO_2, NMVOC, NO_x, NH_3, OC and BC, and the emissions are given in gigagrams per year as a sum from the entire region, divided by the area of the region (Japan: 3.77915×10^{11} m²). Source of data: 2020 CEDS (see Section 4.2.2 for description).

2018). Because industrialization involved a dramatic increase in the production of energy from fossil fuel combustion, the industrialization is clear in the country's historical aerosol emission inventory (Jiang et al. 2017). After 2000, legislation was passed to promote better air quality, and reduced emissions of aerosols and precursors are clearly visible in the country's emission inventory (McDuffie et al. 2020). China's emission history between 1950 and 2014 is shown in Figure 3.2.

3.6.2 Japan

Japan's industrialization began during the late 19th century, sparked by foreign influence (Columbia 2020). A new emperor, Emperor Meji, set in motion large structural changes to catch up with the industries in the West and Japan's industrial sector grew quickly (Columbia 2020). With the rapid growth of industry came the rapid increase in emissions of industrial gases and aerosols (Wakamatsu, Morikawa and Ito 2013). From the 1970s, along with the realization that urban pollution levels were harmful to human health and the local environment, the government of Japan

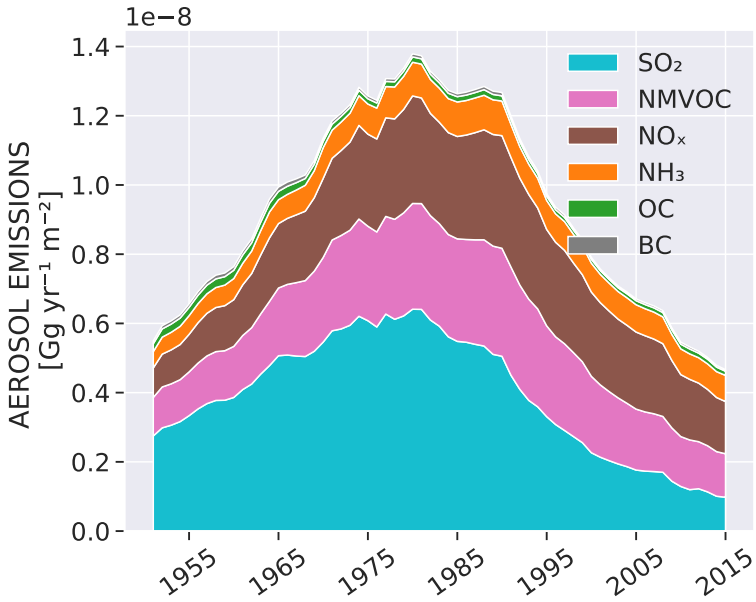

Figure 3.4: Timeseries of the anthropogenic aerosol/precursor emission history between 1950 and 2014 in Europe. Emissions included are: SO_2, NMVOC, NO_x, NH_3, OC and BC, and the emissions are given in gigagrams per year as a sum from the entire region, divided by the area of the region (Europe without Russia: 6.1848×10^{12} m²). Source of data: 2020 CEDS (see Section 4.2.2 for description).

reduced emissions of the polluting particles (Wakamatsu, Morikawa and Ito 2013). Some emissions exhibited a renewed increase during the Japanese price "bubble boom" period between 1986 and 1991 (Wakamatsu, Morikawa and Ito 2013), but this contribution is not clearly distinguishable in Figure 3.3, which shows Japan's emission history between 1950 and 2014.

3.6.3 Europe

Europe's industrialization happened during the 18th and 19th century. In the 1970s, attention was brought to the health hazards of air pollution in the form of aerosol particles, and political will to improve air quality emerged (Sliggers, Kakebeeke and Nations 2004). In addition, the dissolution of the East Bloc in 1989 reduced the industrial activity and thereby also the emissions of aerosols (Krüger, Marks and Graßl 2004). As a result of these factors, Europe's aerosol emissions reached a maximum during the 1980s, and have continued to decrease ever since, as can be seen in Figure 3.4, which shows Europe's emission history between 1950 and 2014.

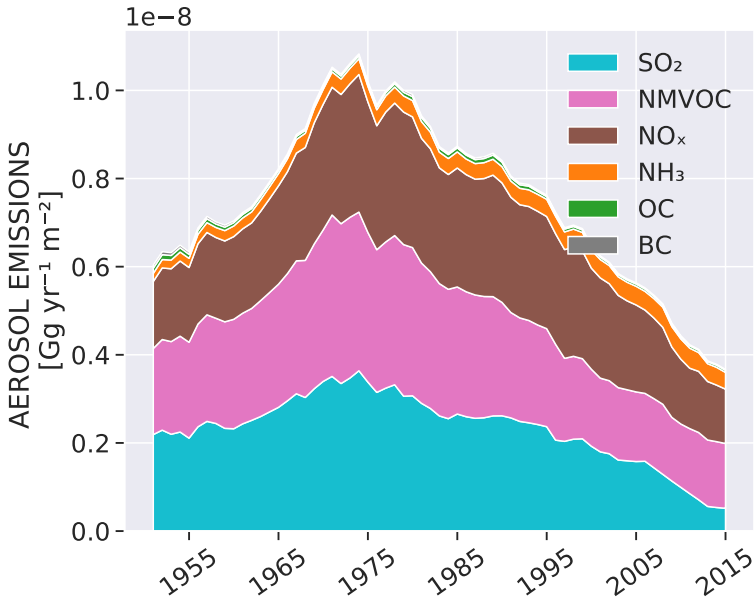

Figure 3.5: Timeseries of the anthropogenic aerosol/precursor emission history between 1950 and 2014 in the United States. Emissions included are: SO_2, NMVOC, NOx, NH_3, OC and BC, and the emissions are given in gigagrams per year as a sum from the entire region, divided by the area of the region (the United States without Alaska: 8.115×10^{12} m². Alaska is omitted due to few SSR stations and low emissions). Source of data: 2020 CEDS (see Section 4.2.2 for description).

3.6.4 United States

The United States' aerosol emissions increased along with population growth and industrialization, up until the 1970s. Like in Japan and Europe, governmental legislation was passed during the 1970s to promote better air quality (Sliggers, Kakebeeke and Nations 2004). This allowed for reduced aerosol emissions and lower levels of aerosols in the atmosphere (Sullivan et al. 2018). The United States' emission history between 1950 and 2014 is shown in Figure 3.5.

Chapter 4

Data and methods

This chapter first introduces datasets, and subsequently describes analysis methods utilized in this thesis. Limitations are also discussed.

4.1 Observational data

The analysis presented in this thesis utilizes observational data from a number of sources. In this chapter, each dataset is presented, and in Appendix B, online sources of the data are provided.

4.1.1 GEBA and ngGEBA

The original Global Energy Balance Archive (GEBA) contains surface energy balance components measured at 2500 locations worldwide (Wild, Ohmura et al. 2017), including measurements of SSR. The original dataset contains substantial temporal gaps during the global dimming and brightening period. To handle this, an altered version of GEBA is studied instead.

The altered GEBA SSR data contains only complete time series between 1961 and 2014, and is dubbed “ngGEBA” (short for "no-gap GEBA") in this thesis. Many stations’ time series were omitted from this version of the dataset, due to insufficient coverage. However, many slightly incomplete SSR time series were filled in using the machine learning method *random forests*. Random forests is described further in Section 4.1.1.1.

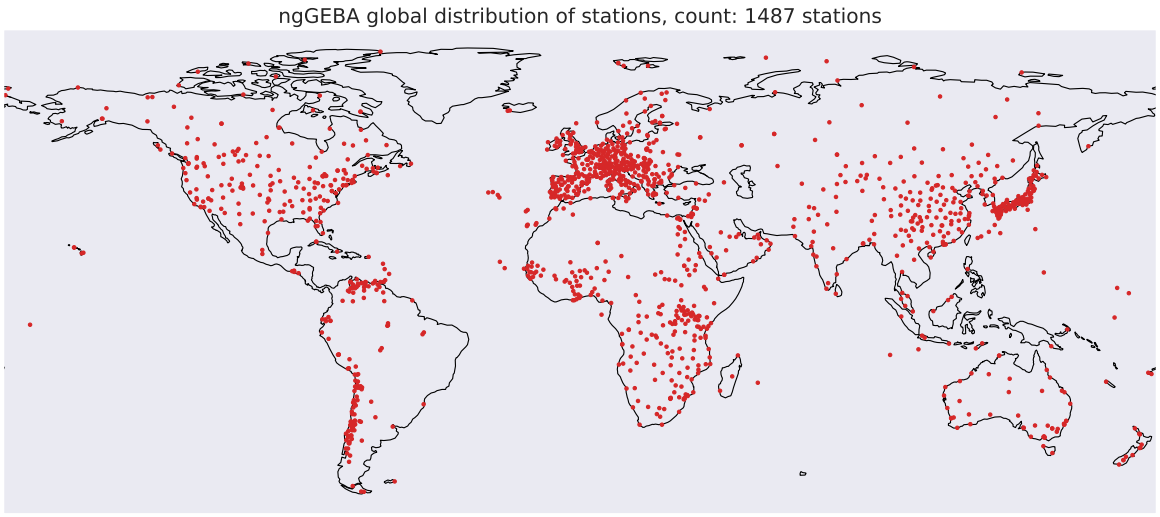

Figure 4.1: Overview of the global distribution of stations contributing to ngGEBA. (ngGEBA is presented in Section 4.1.1.) Station records have been complemented with machine-learning algorithms (random forests).

ngGEBA has 1487 full monthly datasets from between 1961 and 2014, of which 2/3 is generated through the random forests algorithm.

As is clear from Figure 4.1, large regions are not covered by ngGEBA. For the purpose of the present analysis, all data is collocated to these station locations – with the exception of emission data. The limited coverage is the reason why the analysis presented in this thesis is confined to a few regions/countries: Japan, China, Europe (with the exception of Russia) and the United States.

4.1.1.1 The random forests algorithm

Random forests is the machine learning classification algorithm used to fill in the temporal gaps in the GEBA dataset. In short, the random forests algorithm is trained upon GEBA data along with other climatic data that exists as more complete datasets. In this way, the random forests algorithm learns to predict the GEBA SSR data from other climatic data, and GEBA can be filled in using these more complete datasets. The algorithm is trained upon temporal and geographical data from the datasets TBASE (NCAR 2017) and GRUMP (SEDAC 2017), as well as time series of a number of climatic

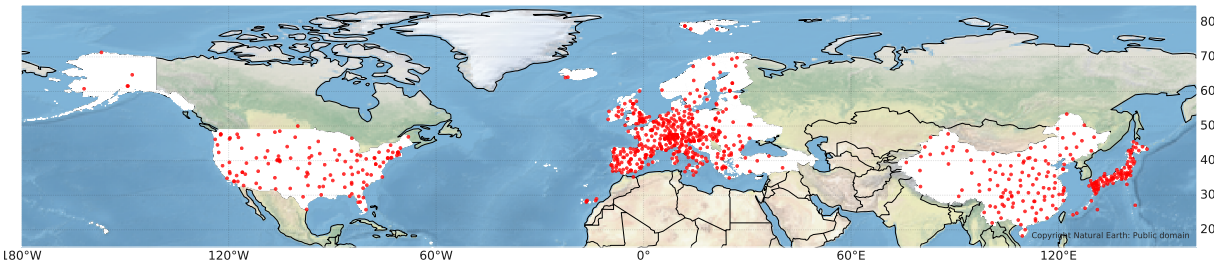

Figure 4.2: Map of GEBA stations (marked with red dots) included in this thesis. The regions studied are indicated in white: China, Japan, Europe (without Russia) and the United States. Same station locations as indicated in Figure 4.1.

variables contained in the gridded dataset CRU TS v4.00 (Harris, Osborn et al. 2020). Specifically, the climatic variables that are used to train the random forests algorithm are maximum temperature, mean temperature, daily temperature range, cloud cover, minimum temperature, vapour pressure, ground frost days, number of rain days and monthly precipitation. The random forests algorithm will not be described thoroughly in this thesis, but is extensively explained and illustrated in Breiman 2001.

4.1.1.2 Stations in each region

As stated, the regions that are chosen for study in this thesis are China, Japan, Europe (without Russia) and the United States. These are chosen based on the number of ngGEBA stations located in each of the regions. Russia is left out because the density of stations is very low, as can be seen in Figure 4.1: With only 32 stations, it is difficult to assume averaged measurements to be representative for the whole country.

There are still other issues with the resulting data. For instance, station density is low in Western China and in Scandinavia, but these regions are kept when computing region averages.

Figure 4.2 shows the distribution of ngGEBA stations that are used in this thesis. Table 4.1 shows the number of stations in each region.

Region	ngGEBA stns.	To be noted
China	119	
Japan	100	
Europe	471	Not incl. Russia (32 stations)
United States	122	

Table 4.1: The number of ngGEBA stations located in each of the regions of focus in this thesis. The number of stations in Russia (32) is already subtracted in the "ngGEBA stns." column for Europe.

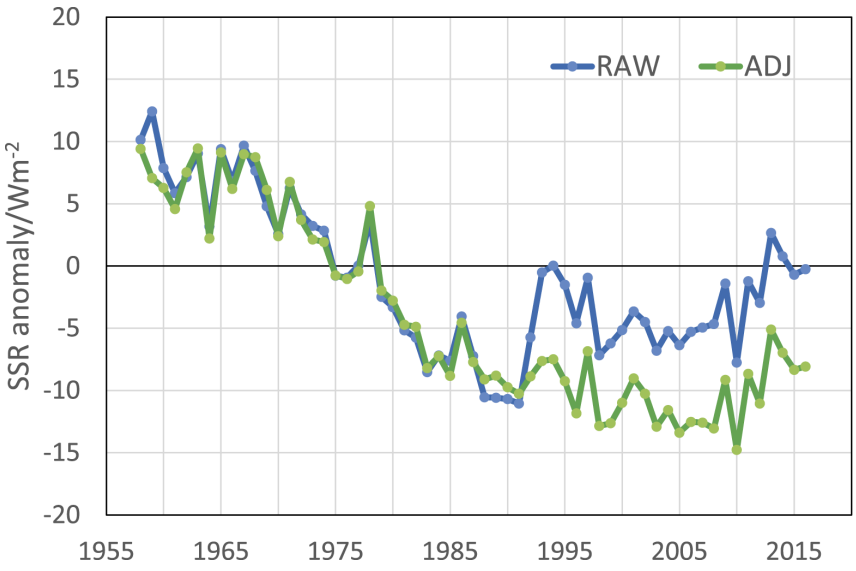

Figure 4.3: Area-weighted average SSR anomaly series over China for the period 1958–2016 as derived from raw (blue) and homogenized (green) SSR data at 119 CMA stations. From: Yang, Wang and Wild 2018.

4.1.1.3 China's 1990s instrumentation change

During the 1990s, there were substantial and widespread changes made to the ground-based network of SSR instruments in China. A large number of instruments were switched out in the early 1990s (Yang, Wang and Wild 2018), and changes were made to instrument locations and the frequency of measurements. It is proposed by Wang and Wild 2016 that these changes were the main cause of a reversal and exaggerated trend in the Chinese national average SSR series during the 1990s.

An attempt has been made to create a homogenized version of the Chinese SSR timeseries. Yang, Wang and Wild 2018 performed assessments of the homogeneity

of Chinese SSR data, from China Meteorological Agency (CMA) weather stations, using nearby surface sunshine duration data as reference. An adjusted version of the SSR timeseries was produced. Figure 4.3 shows the resulting national average SSR timeseries, in its raw and adjusted form. As is clear from the figure, the original timeseries exhibits an apparent "jump" of 10 W/m² in the early 1990s, while the adjusted timeseries exhibits a levelling off during the 1990s, and a slow dimming of $\sim$2 W/m² until the early 2000s.

A similar 1990s "jump" is present in ngGEBA, but to the knowledge of the present author, a homogenized version of ngGEBA does not exist at the present time. Thus, for the purpose of the analysis herein, a crude attempt is made to "homogenize" the Chinese trendline in Section 5.2, along the lines of Yang, Wang and Wild 2018.

4.1.2 CRU TS v4.02 cloud percentage cover

CRU TS v4.02 is a high-resolution ($0.5^\circ \times 0.5^\circ$), gridded monthly observational dataset covering land areas, excluding Antarctica (Harris, Osborn et al. 2020). The dataset contains values from 1901 and onward and includes, among other parameters, historical time series of cloud percentage cover. The cloud parameter is partially based on direct station observations of cloud cover, and partially on proxy measurements of other observed variables, such as sun hour measurements and daily temperature range (Harris, Jones et al. 2014). It should be noted that the exact fraction of data that is computed from proxies is unknown for the period 1961-2014. The CRU dataset is interpolated, and contains no gaps within its domain. The interpolation method is thoroughly described in Harris, Jones et al. 2014. The completeness of the dataset allows for collocation with the GEBA stations (see Section 4.1.1) for the time period 1961-2014.

The temporal coverage of CRU cloud cover is unique. This has its caveats, because there are few alternatives to test CRU against. However, one study tested CRU against satellite and reanalysis data: Calbó and Sanchez-Lorenzo 2009 compare CRU cloud cover data with two other gridded cloud cover datasets over the Iberian peninsula: ISCCP D2 (satellite retrieved cloud cover) and ERA-40 (reanalysis). They find contradictory trends in CRU compared to the other data.

An investigation of CRU has been conducted to study its relevance for comparison with SSR data. The study is included in the appendices, Section E.1. CRU is compared to satellite data from ISCCP (briefly introduced below, in Section 4.1.3), and the two datasets are shown to exhibit different levels and trends of cloud cover in the regions of study. Next, short-term variability in the cloud cover datasets are compared to short-term variability in ngGEBA SSR. The study finds strong anticorrelation in the short-term between CRU and ngGEBA, suggesting that CRU is relevant for comparison with the SSR data.

The appendices also contain an exploration of a possible issue with CRU's conversion from the sun hour proxy to cloud cover (Section E.2). The issue regards the general threshold for measuring a sun hour, which is set to 120 W/m^2: Any atmospheric extinction strong enough to bring SSR lower than 120 W/m^2 is presumably recorded as a cloud, and this investigation attempts to find out what aerosol optical depth is necessary for CRU to mistake the aerosols for cloud cover. The study concludes that the sun hour proxy can wrongfully detect a cloud in periods of high aerosol pollution, especially when the sun is low in the sky.

4.1.3 ISCCP H-series

As stated above, cloud cover data from ISCCP has been included in this study as a supplement to CRU. However, ISCCP is not a part of the main analysis in this thesis.

ISCCP is a global dataset ($1^\circ \times 1^\circ$) of cloud variables based on satellite imagery (Rossow and Schiffer 1999). Specifically, the ISCCP data used is the H-series monthly average total cloud cover. There are caveats with satellite data, even though the dataset is directly based on cloud observations. The analysis that is done on satellite imagery to pull out cloud information has trouble distinguishing clouds over icy, white areas of the surface, and they also have issues detecting optically thin clouds (Rossow and Schiffer 1999).

4.2 Aerosol/precursor emission data

CEDS (Community Emissions Data System) emission data is a widely used gridded global emission dataset, which includes estimates of historical emissions of gases and aerosols, along with future predictions of emissions (Smith et al. 2015). The data is used in the Coupled Model Intercomparison Project (CMIP), serving as the input data for the participating Earth System Models (ESMs). In this study, CEDS anthropogenic aerosol emissions are utilized to compare with SSR and cloud data. The emissions included are anthropogenic emissions of SO_2, NH_3, black carbon, organic carbon, NO_x and NMVOC.

4.2.1 CMIP6 CEDS

CMIP6 CEDS is the emission forcing data used for the 6th Coupled Model Intercomparison Project, CMIP6 (Smith et al. 2015), and it is the latest officially released version of CEDS. In this thesis, CMIP6 CEDS is utilized when analyzing effects of aerosol/precursor emissions on ESM simulations, because CMIP6 CEDS is the simulations' input emission data.

4.2.2 2020 CEDS

For the observational analysis performed in this thesis, the latest unofficial version of CEDS emission data (McDuffie et al. 2020) is utilized. This version is currently (per the submission of this thesis) not the official version of CEDS; however, it is arguably the most updated and accurate version, and is thus the most fitting for the observational analysis. There are some differences in the historical emission trajectories of 2020 CEDS and CMIP6 CEDS. In general, 2020 CEDS exhibits some post-2000 reversals in a number of species' emission trends, perhaps most notably in China, and these are not seen in CMIP6 CEDS (McDuffie et al. 2020). However, the general magnitude of summed aerosol/precursor emissions is similar between CMIP6 CEDS and 2020 CEDS in the regions studied here (McDuffie et al. 2020).

4.2.3 Sum of anthropogenic aerosol/precursor emissions

For a large part of the analysis in this thesis, a simple *sum* of six *anthropogenic* aerosol/precursor species is dubbed "aerosol emissions": SO_2 (precursor), NH_3 (precursor), black carbon (aerosol), organic carbon (aerosol), NO_x (precursor) and NMVOC (precursor). These aerosol/precursor species are the main species from anthropogenic sources (Boucher et al. 2013). The emissions are given in units of mass per time, which means that for the purpose of studying surface solar radiation (SSR) effects of anthropogenic aerosol/precursor emissions, the species-dependent optical properties and the added mass with chemical conversion of a precursor to an aerosol adds to the uncertainty of the analysis.

It has been suggested that the role of absorbing aerosols is highly important in SSR trends (Schwarz et al. 2020). Black carbon is the main anthropogenic absorbing aerosol (Myhre, Myhre et al. 2013), but its relative weight is small compared to the total emissions of aerosols and precursors. To shed some light on the effects of black carbon and other less massive emissions, this thesis also investigates the contributions to SSR trends of some individual species.

4.2.4 Whole-region sum of emissions

The aerosol emissions that are analyzed in this thesis are *not* collocated with ngGEBA stations, and are rather a total sum of the emissions in each respective region. Clearly, aerosol emissions are not static, and depending on wind conditions, may undergo significant transport both horizontally and vertically. Thus, emissions from one region can move out of the region quickly, and instead affect SSR in a different region. Also, the ngGEBA stations are not distributed uniformly across each region, meaning the comparison will be imperfect. However, using emissions from the whole region is arguably a better strategy than using collocated emission data, since the emissions often travel quickly between grid boxes. Also, emissions tend to be spatially heterogeneous and concentrated in industrialized/urban grid boxes.

To facilitate comparison between regions, the summed emissions are divided by the region areas. Alaska is omitted from the United States due to very few ngGEBA stations, low emissions and large relative area. The following areas are used:

- China: 9.597×10^{12} m^2
- Japan: 3.77915×10^{11} m^2
- Europe without Russia: 6.1848×10^{12} m^2
- The United States without Alaska: 8.115×10^{12} m^2

It should be noted that this attempt at normalizing the emissions is imperfect, since emissions are not uniformly distributed, and one could argue that more low-emission regions should have been omitted from these areas. However, it is not a straightforward task to perform a completely fair normalization. This issue may cause the normalized emissions to appear too low, possibly in China, Europe and/or the United States. Japan, on the other hand, is an island country and the smallest region studied, which means that it loses a larger fraction of its emissions to the surroundings. Thus, for Japan, it is reasonable to assume that the normalized emissions give an inflated impression of the aerosol load compared to the other regions.

4.3 CMIP6 model data

For comparison with the SSR and cloud cover data, this analysis studies output from the CMIP6 historical experiment. These historical simulations are initiated from preindustrial control simulations, and are forced with observations and emission data. Most of the simulations start in 1850 and end in 2014, but for the purpose of this thesis work, the years 1961-2014 were studied. Historical simulations from 42 ESMs are included here, and while some model centers do offer several ensemble members (differently perturbed simulations), only one ensemble member from each model is included here. Table 4.2 shows the CMIP6 historical variables considered from the historical experiment. The names and resolutions of the ESMs are provided in the appendices, listed in Table B.1.

Variable	Full name and explanation
rsds	Surface downwelling solar radiation. Equivalent to SSR (surface solar radiation).
rsdscs	Clear-sky surface downwelling solar radiation. SSR when removing the radiative effects of clouds.
clt	Cloud cover total in percent.

Table 4.2: Variable names in CMIP6 model historical runs analyzed in this thesis and explanations of them.

4.4 Correlation

In this thesis, one of the most important things to determine is the behavior of one variable compared to another, in time. To determine the degree of covariation between two variables, a data analyst can determine the *correlation* between the variables.

Pearson's correlation coefficient, also known as R, tells the data analyst something about the strength of the linear association between two continuous variables. R takes a value between -1 and 1. If two variables have an R close to 1, that means the variables are strongly correlated: When one variable increases, the other tends to increase as well. On the other hand, if the R value is close to -1, that means that the variables are strongly anticorrelated: When one variable decreases, the other tends to increase. If there is no such correlation relationship between two variables (they increase or decrease independent of each other), then R takes a value close to zero.

The formula for Pearson's correlation coefficient (R) between two variables is:

$$R = \frac{\sum(x_i - \overline{x})(y_i - \overline{y})}{\sqrt{\sum(x_i - \overline{x}^2)\sum(y_i - \overline{y})^2}} \tag{4.1}$$

Here, x_i and y_i denote the values of variables x and y and $\overline{x}$ and $\overline{y}$ denote the mean values of variables x and y.

When calculating R between two variables, it is important to make sure that the two are independent of each other. There should not be a common cause for certain variation in both. For instance, when handling time series data of two components

where both are dependent on seasonal changes, seasonal variations of each have to be subtracted or smoothed out of the time series before calculating R. For this reason, all correlation coefficients computed in this thesis are computed between either annually- or decadally averaged variables.

4.5 Linear relationship assumption

The next chapter (Chapter 5) contains correlation analyses between aerosol emissions and SSR, where the linear relationships between these components are determined by the computations of correlation coefficients. As introduced in the previous section, Section 4.4, Pearson's correlation coefficient computes the strength of the *linear* relationship between two variables. As such, Pearson's correlation coefficient cannot generally be utilized for computing the magnitude of correlation in exponential relationships. As was introduced in Section 2.1, the relationship between SSR and optical depth is exponential (Beer-Lambert law):

$$E_{surf} = E_0 \exp(\tau / \cos\phi) \tag{2.6}$$

Here, E_{surf} is proportional to $\exp(\tau)$ at a certain solar zenith angle. However, in this thesis, the aerosol parameter studied is aerosol *emissions*. Optical depth τ is an entirely different variable (see Section 2.1) from aerosol emissions, and these two variables cannot necessarily be assumed proportional. This is because higher aerosol concentrations introduce more aerosol coagulation and condensation (Boucher 2015), which means that emissions into an atmosphere already burdened by aerosols will cause weaker radiative effects than emissions into a pristine atmosphere (Stevens 2015). These processes can also give the aerosols shorter lifetimes, which complicates even more. The complex processes related to aerosols are also an important reason why ESM simulations substantially disagree with each other and with observations when it comes to aerosol effects on the radiative budget (Stevens 2015). The relationship between aerosol emissions and optical depth is, in other words, complicated. In turn, this means that it is unclear what mathematical function can describe the relationship between SSR and aerosol emissions.

Nonetheless, approximations can be made, based on a set of assumptions. One such estimation was made in Stevens 2015. The model proposed therein assumes that

the direct effect of aerosols on the radiative budget at the top of the atmosphere is linearly proportional to emissions of aerosols. The model also proposes a logarithmic proportionality with aerosol-cloud interactions. These assumptions can be made for optical depths sufficiently low (Charlson et al. 1992). If these top-of-the-atmosphere relationships are applied also to the relationship between surface solar radiation and aerosol emissions, then it makes sense to compare SSR directly with aerosol emissions and to compute correlations between them.

4.6 Computing "no-cloud SSR"

The purpose of creating a no-cloud SSR timeseries from observations is to be able to separate the effects on SSR of cloud cover variations from those of other extinction agents such as aerosol emissions. For clarity, it is important to distinguish between this calculated no-cloud SSR and clear-sky SSR provided by ESMs, since these are substantially different. In clear-sky SSR, all contributions from clouds are removed, but in no-cloud SSR, changes to the clouds optical properties are still captured.

4.6.1 Procedure

The procedure to compute no-cloud SSR is based on an assumption that SSR during cloudy conditions takes a constant value. One large difference between clear-sky SSR and no-cloud SSR is that any aerosol-cloud interactions (ACI) resulting in different cloud optical properties are still captured in no-cloud SSR. Also, cloud optical properties change depending on changing weather- and climate factors such as cloud height, altitude and humidity (Matuszko 2012), and these cloud properties will still affect no-cloud SSR. It should be noted that only annual- and decadal averages are considered in this thesis, meaning that weather/seasonal factors are averaged out of consideration.

If an average cloud SSR (E_{cloudy}) is assumed, the "no-cloud SSR" ($E_{no-cloud}$) may be computed from all-sky SSR ($E_{all-sky}$) and cloud cover fraction (CLD) using the following logic:

$$E_{all-sky} = E_{cloudy}(CLD) + E_{no-cloud}(1 - CLD) \tag{4.2}$$

$$\implies E_{no-cloud} = \frac{E_{all-sky} - E_{cloudy} \times CLD}{1 - CLD} \tag{4.3}$$

In addition to the aforementioned potential issues with assuming a constant cloud SSR (E_{cloudy}), this computation depends on the accuracy of both the SSR dataset and the cloud dataset, meaning that uncertainty from both datasets is introduced when computing no-cloud SSR.

4.6.2 Constant cloud SSR from observations

Now, the choice of the constant E_{cloudy} is not trivial, and the computation of no-cloud SSR, $E_{no-cloud}$, is sensitive to the choice made. Matuszko 2012 presents a set of values that relate cloud area fraction with SSR, depending on the angular position of the Sun above the horizon. Matuszko 2012's values are generalizations based upon measurements between 2004 and 2007 in Krakow, Poland, but if the properties of clouds are assumed constant as a function of solar zenith angle, the Krakow values for E_{cloudy} may also be used for the entirety of Europe as well as China, Japan and the United States. Assuming average annual solar zenith angles lie between 60° and 70° for all four regions (Cronin 2014), the relevant E_{cloudy} is 109 W/m² according to Matuszko 2012.

For the observational analysis in this thesis, no-cloud SSR is computed using three different assumptions for E_{cloudy}: 90 W/m², 109 W/m² and 120 W/m². Only E_{cloudy} using 109 W/m² is presented and analyzed in the main text, but a sensitivity study is included in Appendix A, Section A.1.

4.6.3 Constant cloud SSR from ESM simulations

This thesis also contains analysis of simulated (CMIP6) SSR data. Since the CMIP6 ESMs provide both all-sky and clear-sky SSR output, along with cloud area fraction, all variables in Equation 4.3 are direct output from the models, except for E_{cloudy}. Thus, E_{cloudy}'s value can be computed. This serves as a study into how much E_{cloudy} varies

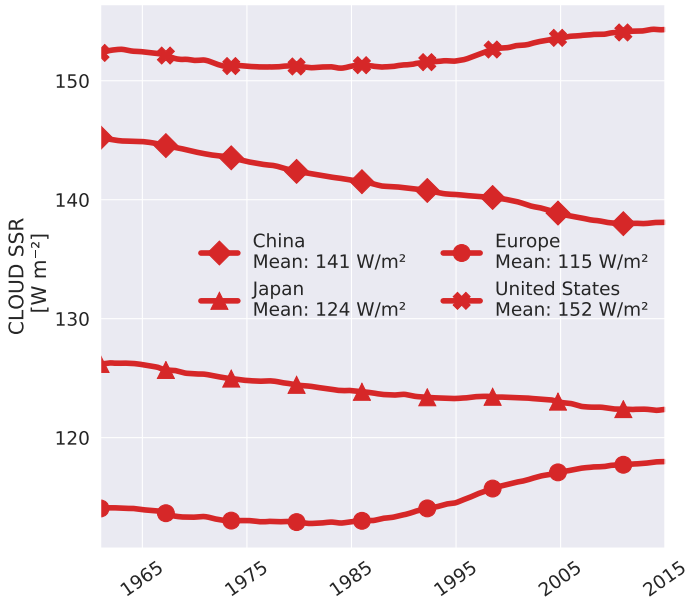

Figure 4.4: Decadal running average of the value of E_{cloudy} as computed from the average of CMIP6 simulations, collocated to the ngGEBA stations in each region. The mean values computed from these trendlines (printed in the figure) are utilized as the "constant" cloud SSR when creating no-cloud SSR from the simulations, analyzed in Section 5.5.

with time in simulations, presumably due to effects such as ACI that change the optical properties of clouds.

Figure 4.4 shows the computed E_{cloudy} from the CMIP6 model means. Clearly, the value of E_{cloudy} is larger in the simulations than in the observations from Krakow (Matuszko 2012) – however, the European simulated mean is quite close. The figure also shows that the general level of E_{cloudy} in simulations differs between regions. One might think that the general level is latitudinally dependent, but since the United States has the highest general level – and China is located closer to the Equator than the United States – latitude is clearly not the only factor in determining E_{cloudy} in simulations. This instead indicates that cloud cover in the United States is optically thin compared to that in China.

It is also clear from Figure 4.4 that E_{cloudy} is not completely stationary: In the span of the period 1961-2014, the value has a trend in all the regions, however not with the same magnitude:

- In China: Simulated E_{cloudy} decreases by about 7 W/m²

- In Japan: Simulated E_{cloudy} decreases by about 4 W/m²
- In Europe: Simulated E_{cloudy} increases by about 5 W/m²
- In the United States: Simulated E_{cloudy} increases by about 3 W/m²

These changes are quite possibly due to the changes in aerosol emissions in these regions, as shown in Section 3.6. Higher emissions may cause lower E_{cloudy} due to a higher number of cloud condensation nuclei and smaller cloud droplet sizes, as explained in Section 2.3.3. This hypothesis does not directly explain what is happening in Japan, since the Japanese emissions decreased rapidly in the 1961-2014 period. However, the simulated transport of aerosols from the Asian mainland may be affecting the Japanese clouds to a significant degree, causing E_{cloudy} to increase there, too.

Chapter 5

Results and discussion

For readability, the following abbreviations are used in Chapter 5:

- "Trendline" and "trend" refer to a 10-year rolling average.
- "Correlation coefficient" refers to Pearson's correlation coefficient
- "Correlation"/"anticorrelation" refers to correlation/anticorrelation between two trendlines in a specific time period. See Section 4.4 for a brief introduction to correlation.

5.1 Cloud effects on observed SSR

The goal in this section is to determine to what degree long-term (decadal and multidecadal) *trends* in SSR may be caused by certain trends in cloud cover. In this endeavor, the original ngGEBA all-sky SSR is compared to the "no-cloud SSR" computed from ngGEBA SSR and CRU TS v4.02 cloud cover, using the method described in Section 4.6. This section contains figures showing the trends in all-sky SSR and no-cloud SSR.

To facilitate discussion, the vertical scaling is identical in all the figures. As will become obvious, the general variations in SSR are much smaller in Europe and the United States than in China and Japan. Thus, Section A.1 in the appendices provides re-scaled versions of the figures for Europe and the United States, to facilitate detailed analysis.

Figure 5.1 compares no-cloud SSR with all-sky SSR in all four regions of focus. The first thing to notice is the difference in general level of no-cloud and all-sky SSR, indicated by the vertical axis labels in colors matching their respective trendlines. As expected, no-cloud SSR is higher than all-sky SSR in general magnitude. Also to note is the variation across regions: The SSR level (no-cloud and all-sky) is somewhat affected by aerosol load in the atmosphere, but it is also largely a function of latitude, since latitude dictates the average solar zenith angle. Europe, being located farthest north, has the lowest SSR level. China, Japan and the United States are located at similar latitudes, which causes them to have similar no-cloud SSR levels. That said, no-cloud SSR is obviously also a function of aerosol load and other extinction agents that vary between regions.

In terms of trends, Figure 5.1 shows that for all regions, the no-cloud SSR trend exhibits larger variations than the observed ngGEBA all-sky trend. This indicates that cloud cover has a dampening effect on both dimming and brightening trends in observed all-sky SSR, and that cloud cover trends do not appear responsible for dimming and brightening in the regions studied here.

In China (Figure 5.1a), the general shape of the all-sky trendline is mainly retained in the no-cloud trendline, but amplified. Interestingly, however, a renewed apparent dimming after 2000 is quite clear from the no-cloud SSR trend, while in the all-sky SSR trend it is hardly visible. Now, as stated in Section 4.1.1.3, some inhomogeneity issues have been discovered with the ground-based SSR data in China, affecting the trendline change during the 1990s. The implications of this are further investigated in Section 5.2.1.

In Japan (Figure 5.1b), the no-cloud trendline exhibits an apparent renewed dimming after 2000, while the all-sky trend only exhibits weak dimming (hardly discernible), suggesting clouds strongly counteract other effects that reduce SSR in that period.

In Europe (Figure 5.1c), the initial dimming from the 1950s to the 1980s (Wild 2012) is not clearly discernible from Figure 5.1c in either of the trendlines. In a scaled version of the figure, Figure A.3b (the middle figure) in Appendix A, one can study the trendline in more detail. The most interesting feature of Figure 5.1c is the renewed apparent dimming in the European no-cloud SSR after 2000. The all-sky trendline exhibits no

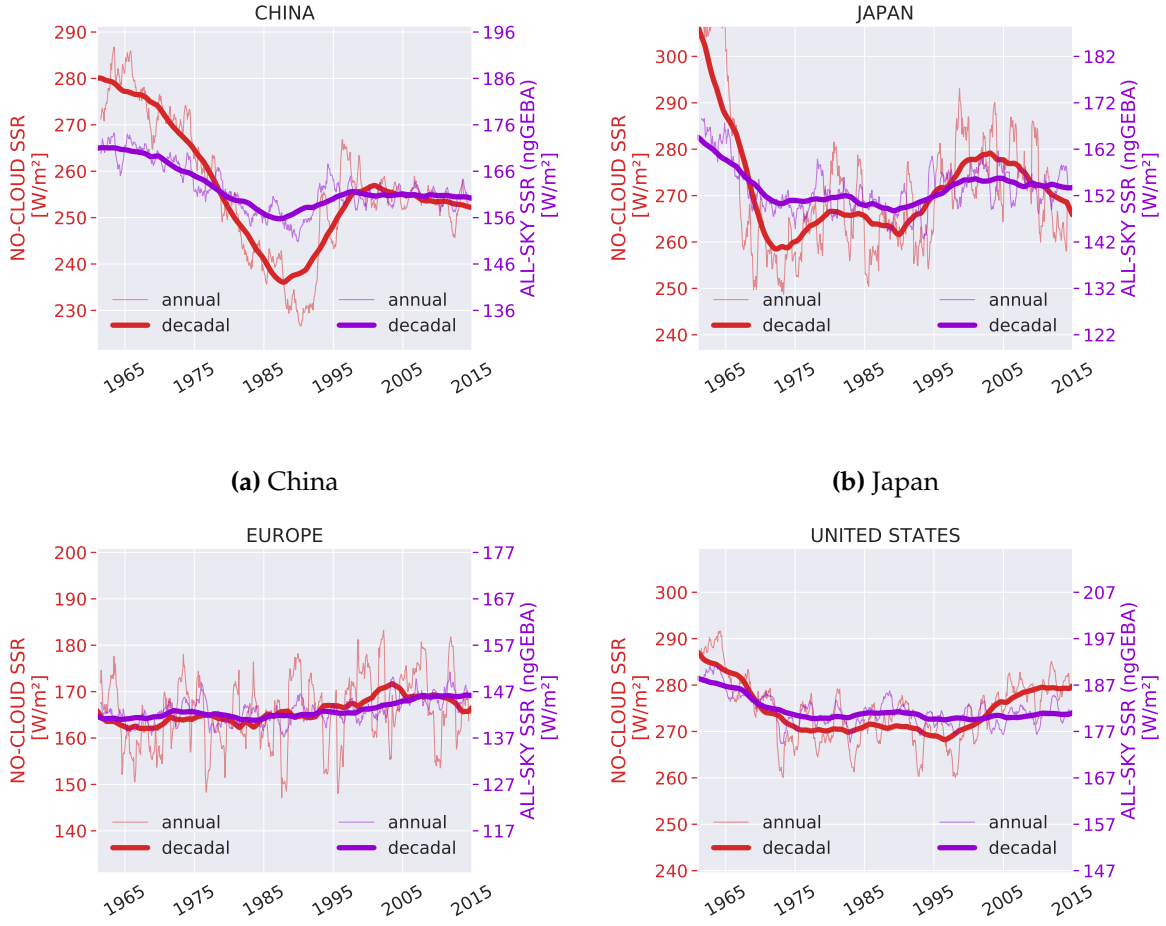

(a) China

(b) Japan

(c) Europe

(d) The United States

Figure 5.1: No-cloud SSR (red) and all-sky SSR (purple) between 1961 and 2014 at ngGEBA stations. Decadal running means are shown in boldface and annual running means are shown in lightface. The computation of no-cloud SSR is described in Section 4.6.

clear sign of a reversal, suggesting that reduced cloud cover during the early 2000s practically concealed the renewed European dimming. Section A.3 in Appendix A shows that the renewed dimming can also be found in the no-cloud SSR trendline produced using ngGEBA and ISCCP cloud cover.

Another interesting feature of the European no-cloud trendline is the fact that it is highly sensitive to the choice of the constant cloud SSR. The previously referenced Figure A.3 contains, for each region, three versions of Figure 5.1c, with three different choices for the constant cloud SSR: 90 W/m², 109 W/m² (same as Figure 5.1c) and 128 W/m². Figure A.3 shows that especially the timing of the initial switch from dimming to brightening is highly dependent upon the choice of cloud SSR. The two higher choices (128 W/m² and 109 W/m²) indicate an early switch to brightening, already in the 1960s. The lower choice (90 W/m²) indicates that brightening begins in the late 1980s. None of the other regions' transient changes in no-cloud SSR exhibit such a high sensitivity to the choice of cloud SSR (all regions are shown in Figure A.3).

Figure 5.1d shows the variations in all-sky and no-cloud SSR in the United States. The general pattern is retained in the no-cloud SSR trend, but a brightening trend between the late 1990s and 2014 is much more distinguishable in the no-cloud SSR trend than in the all-sky SSR trend. This suggests that the increased cloud cover between the late 1990s and the late 2000s masked the brightening in the all-sky SSR trend in the United States. A re-scaled version of Figure 5.1d is placed in Appendix A, Figure A.4b, to allow for more detailed analysis.

5.2 Aerosol effects on observed SSR

In this section, the goal is to determine how aerosol emissions affected observed SSR in 1961-2014. To investigate, the no-cloud SSR trendlines are compared to aerosol emission trendlines to distinguish what effect aerosols have on no-cloud SSR – without the potential masking effect from cloud variations. One should keep in mind that the subtraction method used to produce the no-cloud SSR time series did not subtract out potential effects of aerosols on cloud optical properties. This section compares aerosol/precursor emission trends along with the no-cloud SSR trends for all four regions of focus, and the purpose is to find the most probable cause of the trends seen

in no-cloud SSR.

Figure 5.2 shows the trajectories of total aerosol emissions and no-cloud SSR for each region. It can be gathered from the figure that the initial dimming seen in China, Japan and the United States happens simultaneous to general increase in aerosol/precursor emissions, as can be seen in the correlation coefficients above each subfigure. This suggests that aerosol effects cause the initial decrease in no-cloud SSR in these regions.

After the initial dimming, however, China, Japan and the United States no longer exhibit a clear anticorrelation with the emission trends. Thus, the sum total aerosol/precursors cannot explain the subsequent brightening or stabilization seen in no-cloud SSR. The correlation coefficients covering the entire period 1961-2014 quantify the weakened relationship compared to the initial dimming period (above each subfigure). This is further discussed in Section 5.2.2.

It should be noted that Japan is a small region, and it is arguably strongly influenced by other regions' aerosol emission trends, especially due to its position downwind from the Asian mainland (because of prevailing westerly winds). China is one region upwind from Japan, and it has a substantially different trendline of aerosol emissions. It is highly possible that the no-cloud SSR trendline over Japan is increasingly affected by the Chinese emissions through the period in question, since the Chinese emissions increase in magnitude almost throughout. Hypothetically, an aerosol emission trendline including Japan and countries upwind from Japan may exhibit a trend more anticorrelated with no-cloud SSR than that of only Japanese emissions shown in Figure 5.2b.

In Europe (Figure 5.2c), the initial dimming is not apparent in ngGEBA in the period of study (1961-2014), since the European dimming began already in 1950. However, the maximum in emissions is reached during the late 1970s, which means that the summed aerosol/precursor emissions cannot explain the relative stability in no-cloud SSR throughout the 1960s and 1970s in Europe. The renewed apparent dimming after year 2000 is also not expected. As for Japan, one can speculate whether Europe, too, is influenced by aerosol emissions from elsewhere. In this analysis, Russian emissions are not included; however, in reality Europe's airspace is arguably sensitive to Russia's emissions. Since Russia's industrial activity has continuously increased since the

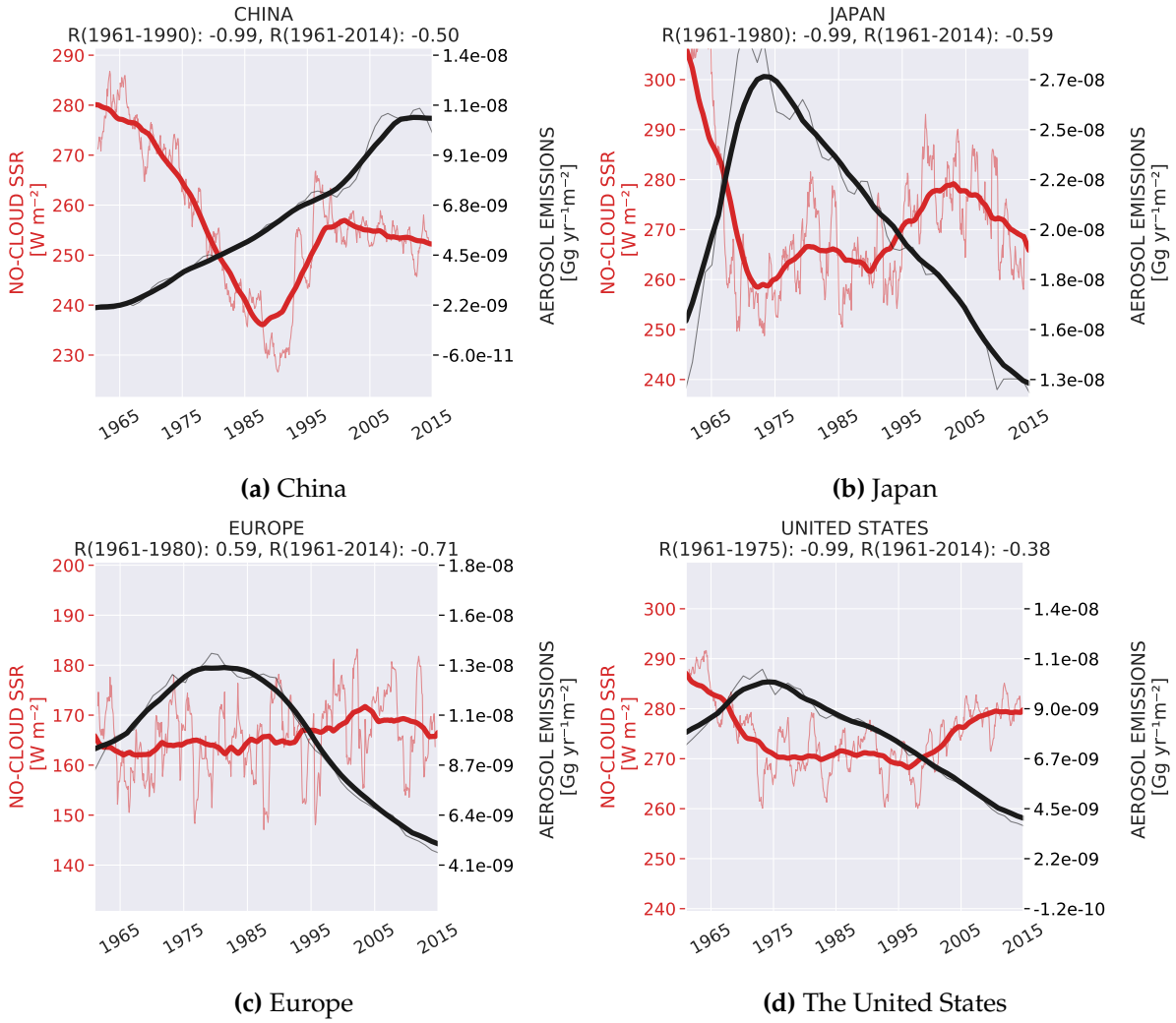

(a) China **(b)** Japan

(c) Europe **(d)** The United States

Figure 5.2: Trendline comparison of no-cloud SSR from ngGEBA and aerosol/precursor emissions from 2020 CEDS (sum of SO_2, NH_3, black carbon, organic carbon, NO_x and NMVOC). Decadal running means in boldface and annual running means in lightface. Assumed constant cloud SSR: 109 W/m². Above each subfigure: Pearson's correlation coefficient (R) between each trendlines computed for two time periods: the initial dimming period in the respective region and the entire period 1961-2014.

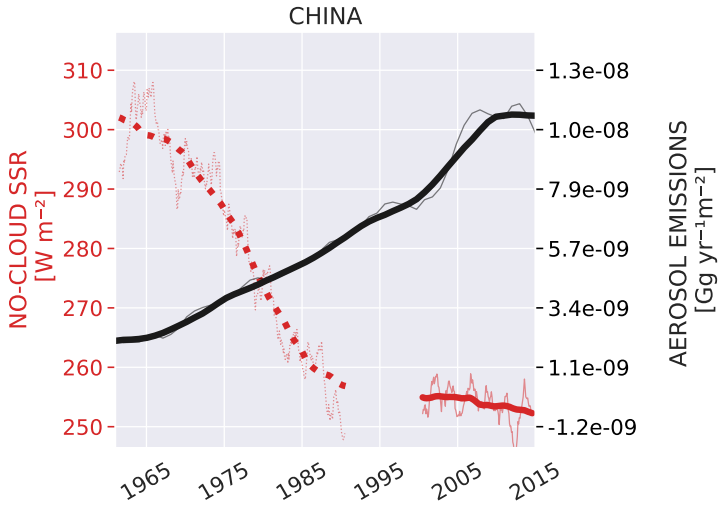

Figure 5.3: Altered version of Figure 5.2a, assuming that the ngGEBA brightening trend during the 1990s is an artifact of instrumentation (Wang and Wild 2016). The dotted, red line is the decadal trend in an altered version of no-cloud SSR – computed from the original ngGEBA all-sky SSR trend raised +9 W/m² between 1961 and 1990. The solid, red line is the same no-cloud ngGEBA as in 5.2a between 2000 and 2014. The boldface black line is the decadal trend in annual aerosol/precursor emissions (sum of SO_2, NH_3, black carbon, organic carbon, NO_x and NMVOC) from 2020 CEDS in China, the lightface is the annual data. Assumed constant cloud SSR: 109 W/m².

aftermath of the dissolution of the East bloc (Smirnov 2015), an investigation into the effect of including Russia's aerosol emissions was performed. But even when including those, the total emissions still exhibited a reduction after 2000, undermining the theory that Russia's industry caused the renewed dimming.

5.2.1 Altered no-cloud SSR in China

As explained in Section 4.1.1.3, most of the Chinese brightening trend during the 1990s might be an artifact of instrumentation change. To visualize and investigate the effects of a homogenization of ngGEBA, a crude attempt has been made to homogenize the trendline along the lines of Yang, Wang and Wild 2018, as reproduced in Figure 4.3. Figure 5.3 shows the resulting figure. Assuming this altered trendline to be correct, the aerosol emissions seem to be able to explain the entire SSR trend until around 2010, when the aerosol emissions begin decreasing. It should be noted that the rigorously computed timeline in 4.3 exhibits a brightening after 2010, which is not reproduced

in Figure 5.3. This brightening better match the emissions trendline, which exhibit a reversal around the same time.

5.2.2 Individual aerosol species effects on observed SSR

The trendlines of total aerosol/precursor emissions in Figure 5.2 are unable to explain the entirety of the observed trends in SSR. Thus, it is necessary to continue the investigation into potential causes.

The total emissions of aerosols/precursors are dominated by SO_2, NO_x and NMVOC. These species all have trends similar to the total between 1961 and 2014. In the following, more minor contributors to the total are compared to the no-cloud SSR trends in order to throw some light on these smaller trends that are not necessarily correlated with the general emission trend. It should be realized that if these relatively small contributors can explain the effects observed, their individual contributions to extinction must necessarily be much larger per mass than the species dominating the total emissions.

The first region of study is China (Figure 5.4). Although the previous section investigated an altered or homogenized version of China's SSR trend, the unaltered version is studied along with the individual species in Figure 5.4. The figure shows that emissions of NH_3, black carbon and organic carbon increase for the entirety of the dimming period in no-cloud SSR, similar to the total emission sum. In the late 1990s, organic carbon emissions reverse, but this reversal occurs after the switch to brightening in the ngGEBA trend. NH_3 and black carbon increase throughout the period 1961-2014, and cannot explain the no-cloud SSR trend after the initial dimming. For Japan, Figure 5.5 reveals that trendlines of NH_3, black carbon and organic carbon are all to some degree anticorrelated with the SSR trend between $\sim$1980 and $\sim$2000. These emissions reach a maximum almost simultaneous to the intermittent minimum around 1990 in the no-cloud SSR brightening. Acknowledging that aerosol optical properties vary between different species, the combined effect of increases in NH_3, black carbon and organic carbon may be enough to counteract the decreasing trend in the species making up the majority of the total emission sum – resulting in the intermittent dimming during the 1980s. The renewed dimming after 2000 is not

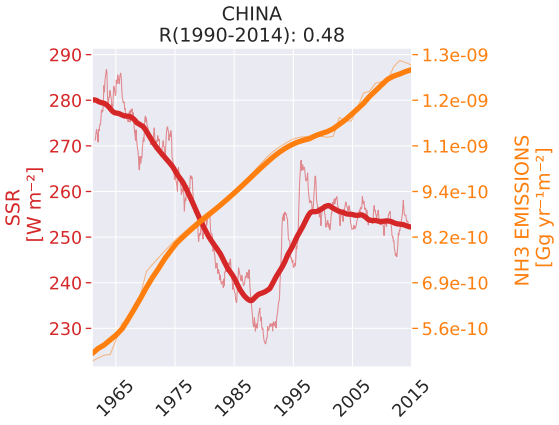

(a) Ammonia (NH_3)

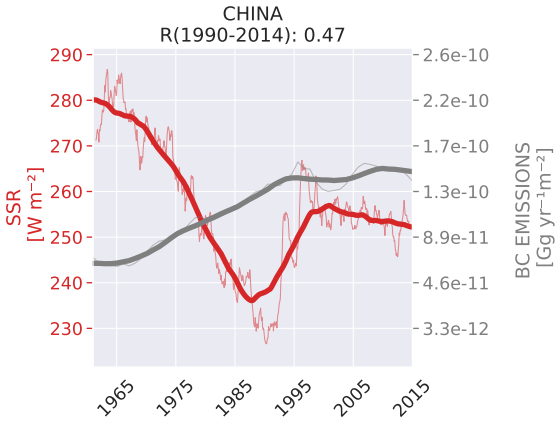

(b) Black carbon (BC)

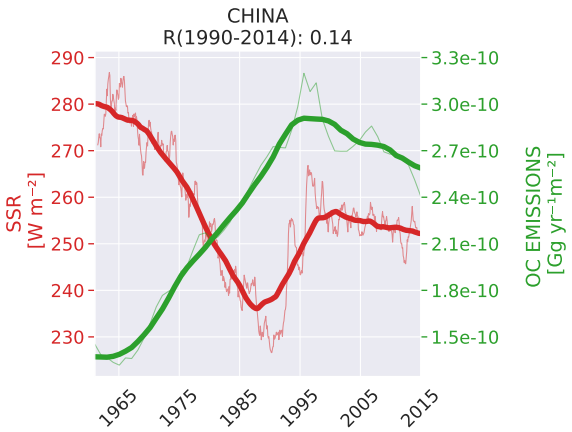

(c) Organic carbon (OC)

Figure 5.4: For China: No-cloud SSR trendlines from ngGEBA shown in red, annual emissions of individual species from 2020 CEDS are shown in orange (NH_3), grey (BC) and green (OC). Decadal running average in boldface and annual running average in lightface. Assumed constant cloud SSR: 109 W/m². Above each subfigure: Pearson's correlation coefficient (R) between the trendlines in certain time periods.

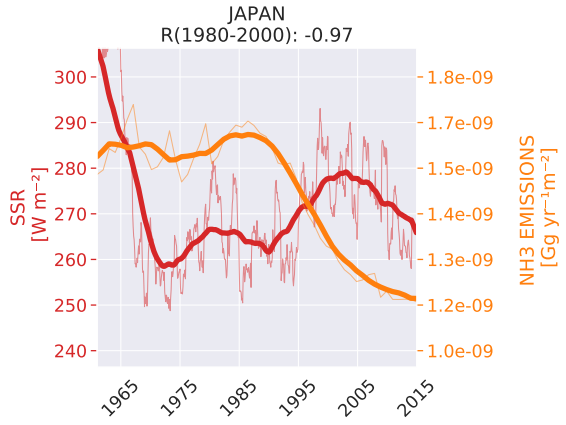

(a) Ammonia (NH_3)

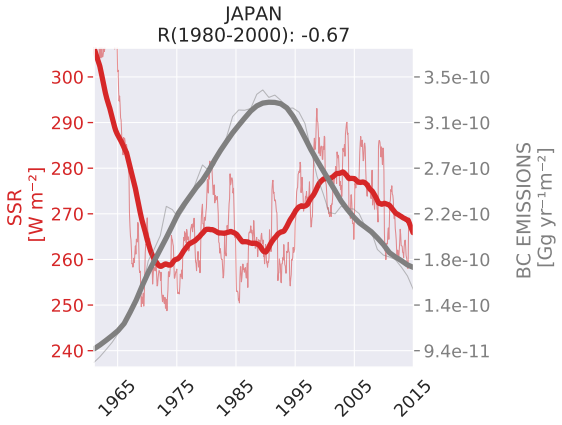

(b) Black carbon (BC)

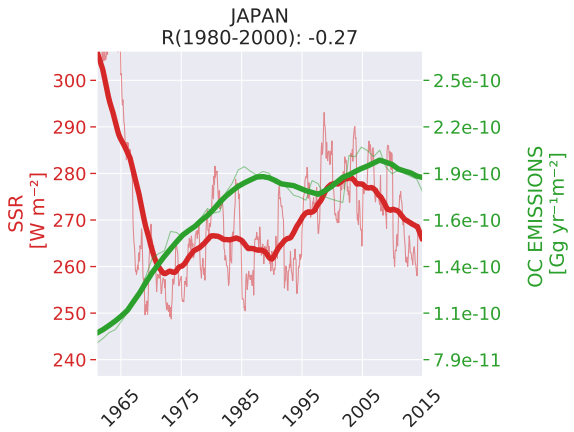

(c) Organic carbon (OC)

Figure 5.5: For Japan: No-cloud SSR trendlines from ngGEBA shown in red, annual emissions of individual species from 2020 CEDS are shown in orange (NH_3), grey (BC) and green (OC). Decadal running average in boldface and annual running average in lightface. Assumed constant cloud SSR: 109 W/m². Above each subfigure: Pearson's correlation coefficient (R) between the trendlines in certain time periods.

consistent with any of the emission trendlines. Also in Europe (Figure 5.6), the emissions of black and organic carbon exhibit interesting trendlines. The variations of black carbon emissions (Figure 5.6b) somewhat mirror those of no-cloud SSR in Europe, most clearly from the 1980s until ∼2000. The general level of aerosol emissions other than black carbon is very high up until after the 1980s (see Figure 5.2c), which could hypothetically be one reason why the effect of black carbon seems to increase from the 1980s and until ∼2000. Similar to black carbon, the organic carbon trend (Figure 5.6c) mirrors that of no-cloud SSR after the 1980s. However, organic carbon emissions furthermore continue to mirror no-cloud SSR as it exhibits the renewed dimming. As such, organic carbon is the only species which could possibly explain the apparent renewed dimming after the year 2000. A combined black- and organic carbon effect could be responsible for the trends up until 2000, but since black carbon stabilizes after 2000, only organic carbon could indicate the renewed dimming. In the United States, the stabilization between the 1970s and the late 1990s is not explained by the summed total emissions. As seen in Figure 5.2d, emissions continuously decrease in the United States after the peak emissions in the 1970s. Figure 5.7 shows that NH_3 increases throughout the period in question, while organic carbon exhibits a peak in the middle of the stabilization period. These two combined may serve as an explanation why the SSR trend is stable in the United States throughout the late 1970s and the late 1990s.

Having completed this observational study, the next sections deal instead with *simulated* SSR from Earth System Models (ESMs). The observational analysis has hopefully given somewhat of a background in possible mechanisms responsible for the observed SSR trends between 1961 and 2014, to allow for an enlightened investigation into causes of ESM simulation biases.

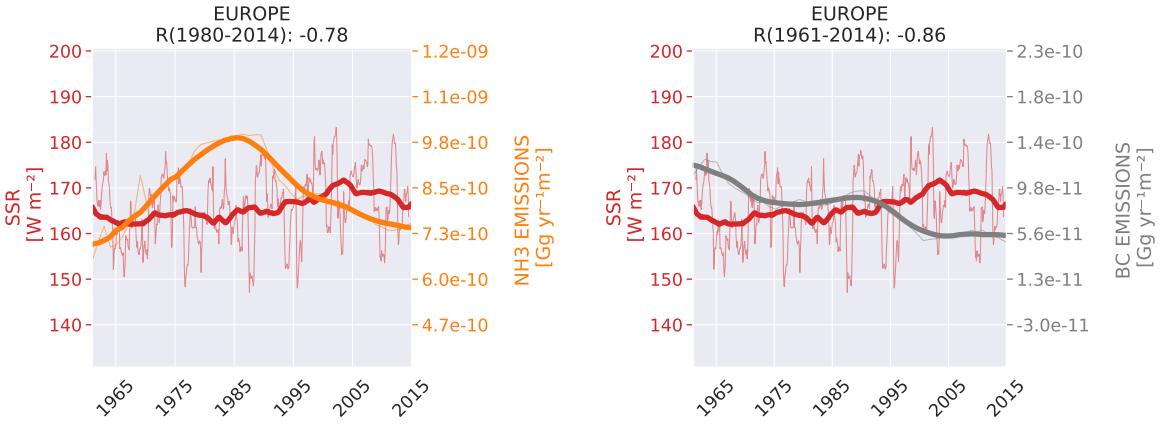

(a) Ammonia (NH_3)

(b) Black carbon (BC)

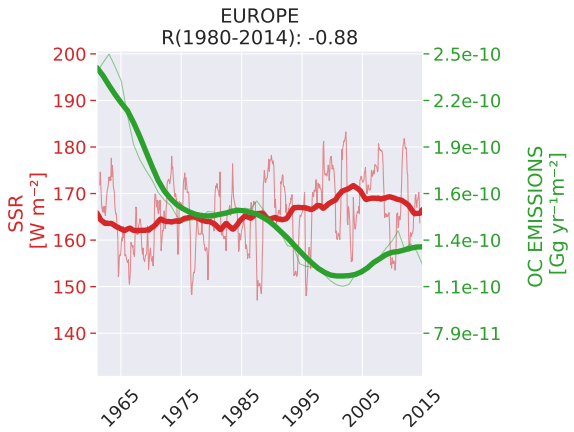

(c) Organic carbon (OC)

Figure 5.6: For Europe: No-cloud SSR trendlines from ngGEBA shown in red, annual emissions of individual species from 2020 CEDS are shown in orange (NH_3), grey (BC) and green (OC). Decadal running average in boldface and annual running average in lightface. Assumed constant cloud SSR: 109 W/m². Above each subfigure: Pearson's correlation coefficient (R) between the trendlines in certain time periods.

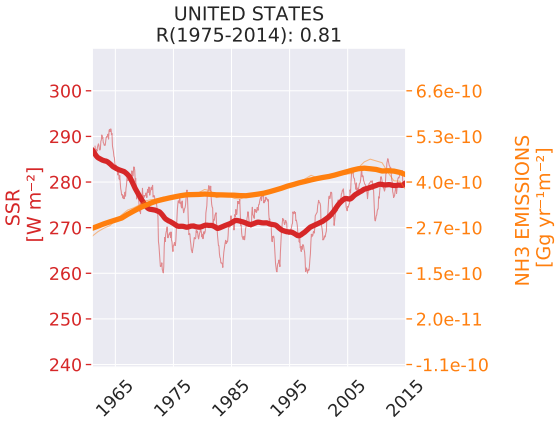

(a) Ammonia (NH_3)

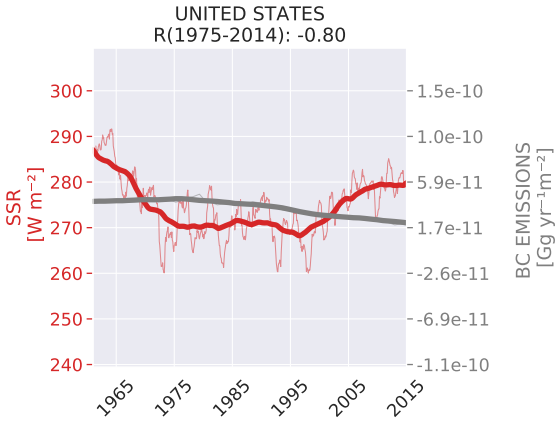

(b) Black carbon (BC)

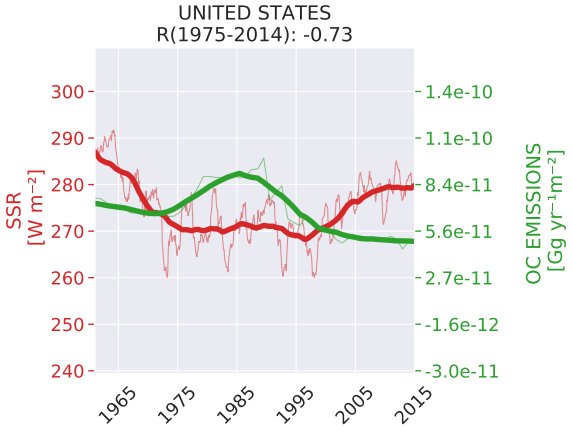

(c) Organic carbon (OC)

Figure 5.7: For the United States: No-cloud SSR trendlines from ngGEBA shown in red, annual emissions of individual species from 2020 CEDS are shown in orange (NH_3), grey (BC) and green (OC). Decadal running average in boldface and annual running average in lightface. Assumed constant cloud SSR: 109 W/m². Above each subfigure: Pearson's correlation coefficient (R) between the trendlines in certain time periods.

5.3 Bias in simulated SSR

As discussed in Section 3.5, ESMs have been found not to be able to reproduce the full extent of the dimming in SSR. The latest generation of ESMs has only partly been studied with regards to dimming and brightening (Moseid et al. 2020). This section investigates the average of 42 simulations from 42 models participating in CMIP6 manages to reproduce the all-sky SSR trend seen in ngGEBA. The ESMs whose CMIP6 historical runs are analyzed are listed in Table B.1 in Appendix B.

Figure 5.8 shows the anomalies of all-sky SSR in the CMIP6 simulation mean compared to ngGEBA, and reveals that the ESMs remain unable to reproduce the magnitude of dimming observed at ngGEBA sites in China, Japan and the United States. This was found for many regions in the previous generation of ESMs as well (Storelvmo et al. 2018; Allen, Norris and Wild 2013), and confirms for a larger set of CMIP6 models the same conclusion made for a subset of these models by Moseid et al. 2020.

The brightening trend in Europe after the 1980s is fairly well reproduced in CMIP6. This was also found for the model subset studied in Moseid et al. 2020. If it is assumed that the emission inventory of Europe accurately represents reality, this suggests that the models are, indeed, able to translate emissions into optical depth and SSR, as suggested by Moseid et al. 2020. However, this might indicate that the emission inventories of the other regions studied here (China, Japan and the United States) are erroneous. This hypothesis is later challenged when the effects of aerosol emissions on SSR are quantified and compared in Section 5.6.

In China (Figure 5.8a), even if the trend in the 1990s is the result of artifacts (see Section 4.1.1.3), the CMIP6 simulations are highly biased, showing a dimming of around 5 W/m^2 in 1961-1980 when ngGEBA shows a dimming of more than 15 W/m^2.

Having studied the all-sky trends, the following sections investigate potential causes for these biases and differences by looking instead at clear-sky and no-cloud SSR, which removes the effects on SSR due to cloud cover variations.

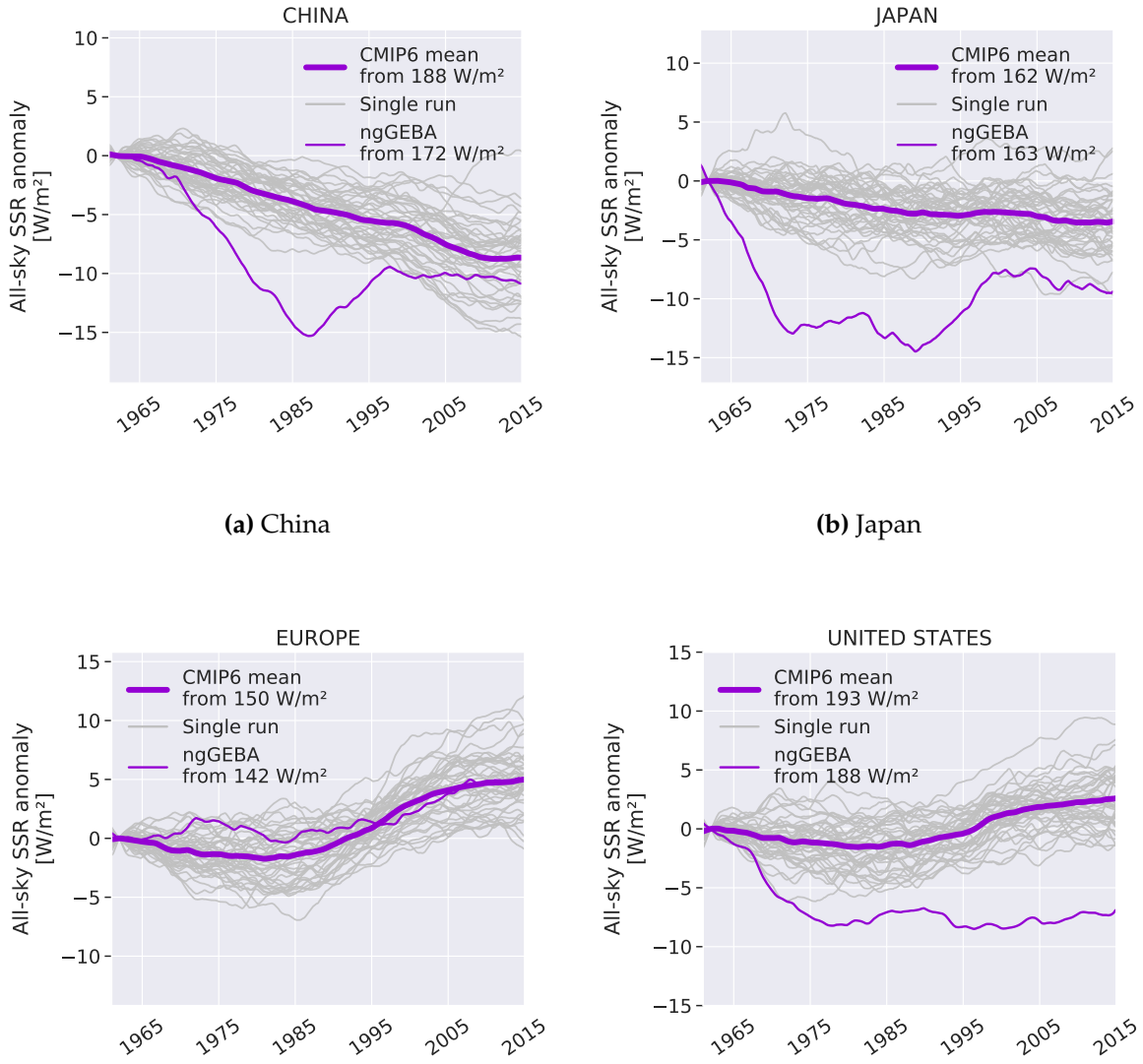

(a) China

(b) Japan

(c) Europe

(d) The United States

Figure 5.8: Decadal running means of mean simulated (CMIP6) and observed (ngGEBA) all-sky SSR anomalies between 1961 and 2014 at ngGEBA stations in four regions: Mean CMIP6 in boldface and ngGEBA in lightface. Grey lines are decadal running means of each model run included. The anomalies are computed by averaging the initial 5 years of the running mean timeseries (this average is printed after "from" in the legend items), and subtracting this mean value from each subsequent time step. Included in the computation is one CMIP6 simulation (r1i1f1p1) from each of the 42 models presented in Section 4.3.

5.4 Cloud effects on simulated SSR

This section studies the contribution from simulated cloud cover to the regional all-sky SSR trends, by comparing clear-sky, no-cloud and all-sky in the models. This analysis is equivalent to the one made on observational data in Section 5.1.

As previously stressed, one should not directly compare no-cloud SSR to clear-sky SSR, since these are not the same quantity. No-cloud SSR retains radiative effects of cloud optical property changes, for example due to ACI. In order to study how different these two quantities are, this section includes both clear-sky and no-cloud SSR computed from simulations. The choices for the constant cloud SSR (E_{cloudy}) in the computations of simulated no-cloud SSR were introduced in Section 4.6.

Figure 5.9 shows that the clear-sky SSR closely follows the all-sky SSR in all regions. In regions with simulated dimming (China and Japan), the clear-sky trendline exhibits more dimming than all-sky. This suggests that in these regions, simulated cloud cover had a weakening effect on the dimming trend in all-sky SSR. However, in regions with brightening trends (Europe and the United States), the simulated clear-sky SSR exhibits less brightening than all-sky, which suggests that simulated cloud cover has a strengthening effect on the brightening in all-sky SSR. Thus, Figure 5.9 implies that dimming trends in simulations are weakened by clouds, but brightening trends are strengthened by clouds. This is seemingly due to the fact that simulated cloud cover in all regions decreases throughout the period of study (see Figure A.9 in Appendix A, which shows simulated cloud cover compared to observed). Nonetheless, the trends in clear-sky SSR are much weaker than those found in observations, and as such, simulated clouds cannot explain the bias between CMIP6 and observed SSR.

The no-cloud SSR computed from simulation output shows stronger dimming than the clear-sky SSR in all regions, and stronger subsequent brightening in Europe and the United States. The difference from the clear-sky SSR trendline directly follows from the computations made in Section 4.6 and Figure 4.4, where it was shown how the "actual", non-constant cloud SSR (E_{cloudy}) developed the least in the United States and Europe, and the most in China and Japan. Here, in Figure 5.9, the largest deviation from clear-sky is seen in China and Japan, and the lowest in the United States and Europe.

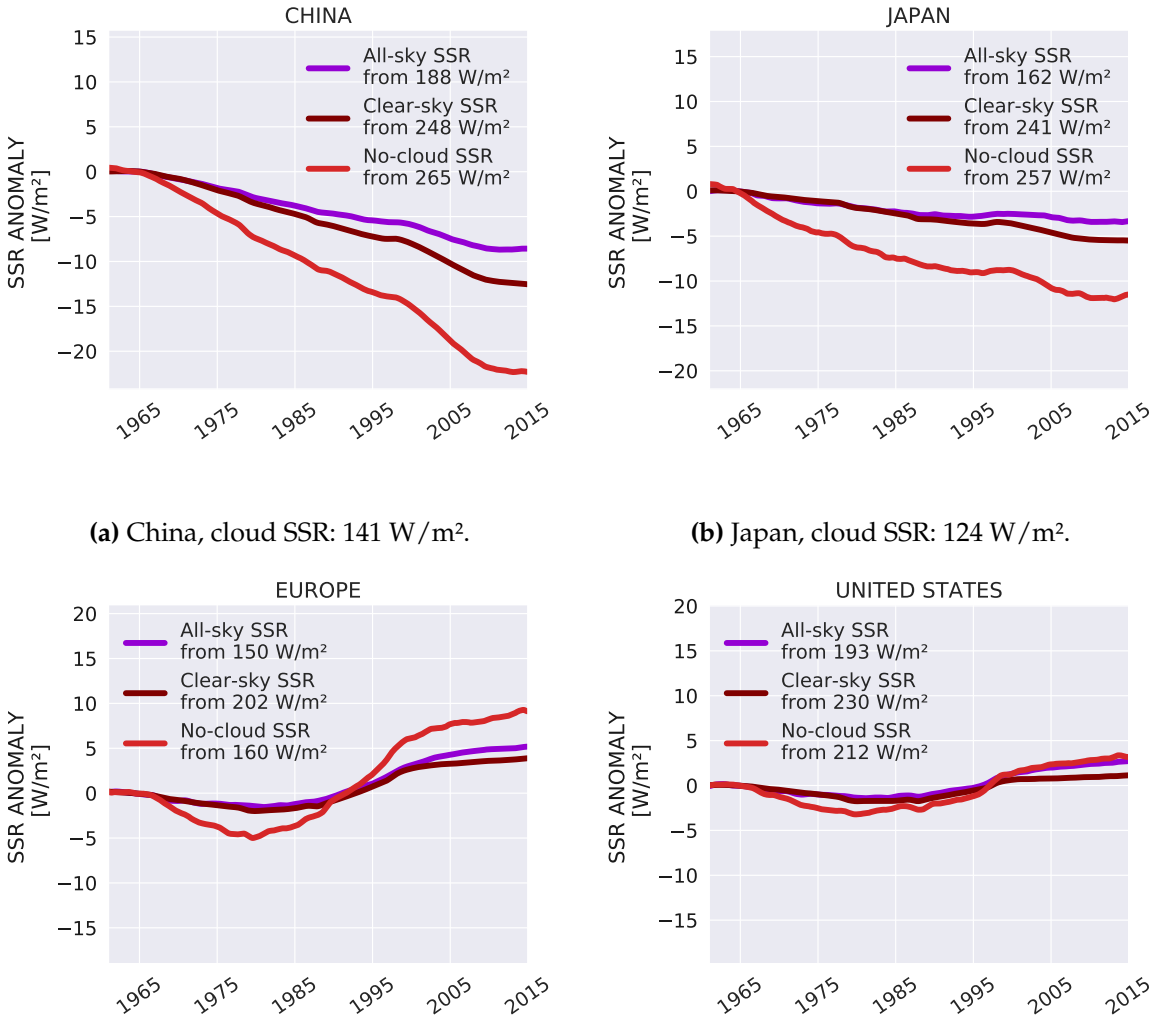

(a) China, cloud SSR: 141 W/m².

(b) Japan, cloud SSR: 124 W/m².

(c) Europe, cloud SSR: 115 W/m².

(d) The United States, cloud SSR: 152 W/m².

Figure 5.9: Decadal running means of mean simulated (CMIP6) clear-sky, no-cloud and all-sky anomalies between 1961 and 2014 at ngGEBA stations: All-sky in purple, clear-sky in maroon and no-cloud in red. The anomalies are computed by averaging the initial 5 years of the running mean time series (this average is printed after "from" in each legend item), and subtracting this mean value from each subsequent time step. Assumed constant cloud SSR is indicated below each subfigure. Included in the computation is one CMIP6 simulation (r1i1f1p1) from each of the 42 models presented in Section 4.3.

The magnified dimming and brightening in no-cloud SSR compared to clear-sky SSR (Figure 5.9) can be understood as follows: Clear-sky SSR experiences no contribution from ACI, meaning that increased emissions (such as in China) will affect no-cloud SSR by increasing cloud scattering, but not clear-sky SSR since the clouds are fully removed. By the same logic, decreased emissions (such as in the United States) will be felt more strongly by no-cloud SSR, since the scattering efficiency of clouds decrease with decreasing emissions.

5.5 Aerosol effects on simulated SSR

In this section, an investigation is made into what effects aerosol emissions have on the dimming and brightening that is present in the simulations, regardless of how these compare to observations. It should be noted that the aerosol emissions shown here are not exactly the same as those studied in the observational analysis in Section 5.2, because the CMIP6 simulations are run using an older version of CEDS aerosol emissions, and the purpose of this section is to study what effect these input emissions have on no-cloud SSR.

It was found in Section 5.3 that the simulated SSR trend in the CMIP6 simulations exhibits a too-weak dimming in China. Nonetheless, a relatively slight dimming was evident. Now, the question is, did aerosol emissions cause the slight dimming in the simulations? Figure 5.10a shows a comparison between simulated no-cloud SSR and input aerosol emissions. It is evident from the figure that the no-cloud SSR trend closely mirrors that of the input aerosol emissions, suggesting a strong dependence. Throughout the period 1961-2014, the trendlines are roughly perfectly anticorrelated, as shown in the correlation coefficients at the top of the figure. A clear anticorrelation was found also in the observational study for the period 1961-1990 (Figure 5.2a). And if the altered trendline (Figure 5.3) is assumed correct, the observed trendlines in China exhibit a clear anticorrelation until 2010. In this scenario, the bias between observed and simulated SSR may be caused by a model issue with translating emissions into a realistically high optical depth, or that the magnitude of emissions is simply too low.

Section 5.3 showed that the simulated dimming in Japan was weaker than observed dimming, and Section 5.4 found that weakening of the trend by cloud cover was not

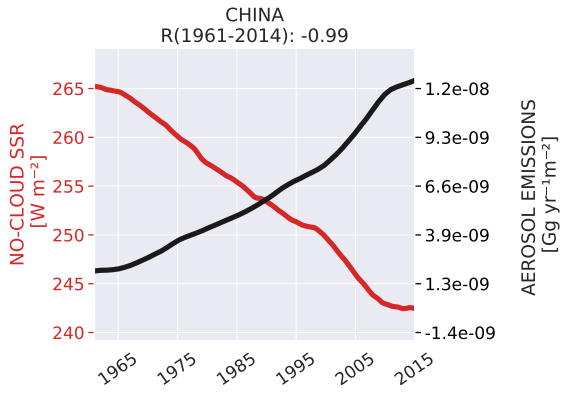

(a) China, cloud SSR: 141 W/m².

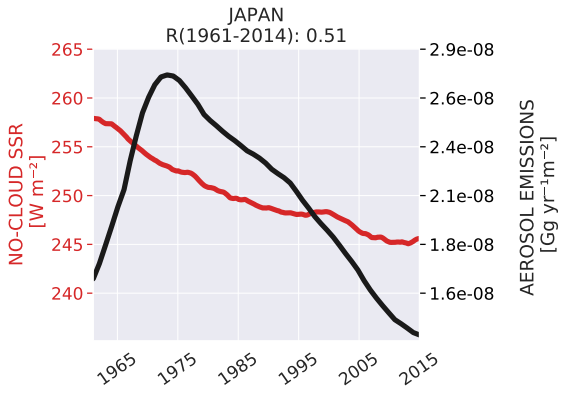

(b) Japan, cloud SSR: 124 W/m².

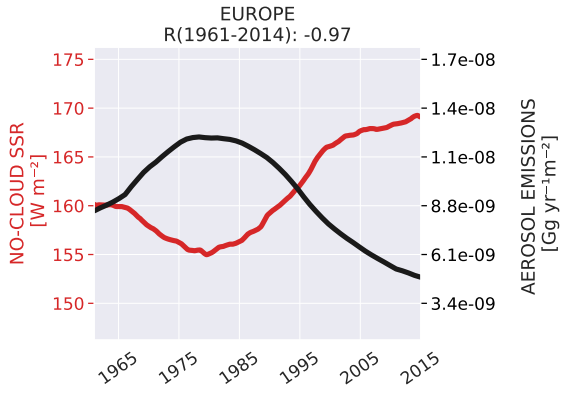

(c) Europe, cloud SSR: 115 W/m².

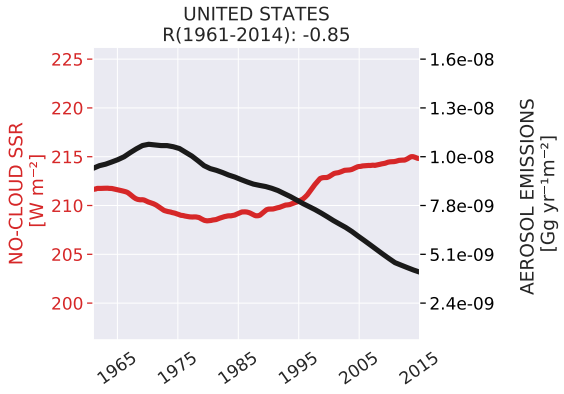

(d) The United States, cloud SSR: 152 W/m².

Figure 5.10: Decadal running means of mean simulated (CMIP6) no-cloud SSR and input aerosol emissions (CMIP6 CEDS, sum of SO_2, NH_3, black carbon, organic carbon, NO_x and NMVOC) between 1961 and 2014 at ngGEBA stations: No-cloud SSR in red; aerosol emissions in black. At the top of each subfigure, Pearson's correlation coefficient between the trendlines is shown for the period 1961-2014. Assumed constant cloud SSR is indicated below each subfigure. Included in the no-cloud SSR mean is one CMIP6 simulation (r1i1f1p1) from each of the 42 models presented in Section 4.3.

the main cause for bias between the simulations and observations. In addition to the too-weak magnitude of dimming, the simulated SSR trend is continuously negative throughout the period 1961-2014, which is not seen in observations. The remaining question herein is what effect the input aerosol emissions have on the simulated SSR, and Figure 5.10b reveals that there is no clear relationship between the trendlines of no-cloud SSR and aerosol emissions. Recalling the suggestion from Section 5.2 that there might be aerosol transport from mainland Asia affecting the *observed* SSR trend, it is also possible that the simulations transport extinction agents from outside of Japan in the wrong way. To rephrase, Figure 5.10b reveals that the effect of the input aerosol emissions on *simulated* SSR is not clear, and hypothetically, there might be erroneous transport in the simulations.

For Europe (Figure 5.10c), the previous section concluded that the all-sky SSR trend is well reproduced by the models. Here, the simulated no-cloud SSR trend is studied along with the input aerosol emissions, to investigate the relationship between the two variables in the simulations. Figure 5.10c reveals that simulated no-cloud SSR and aerosol emissions are almost perfectly anticorrelated, suggesting a clear, causal relationship in the simulations. This was not the case in the observational study performed.

Finally, for the United States (Figure 5.10d), the comparison between aerosol emissions and simulated clear-sky SSR looks quite similar to that between the observed no-cloud SSR and aerosol emissions (Figure 5.2d). The two trendlines mirror each other quite closely, although their anticorrelation is not perfect. The initial increase in aerosol emissions is more rapid than the decrease in SSR, and after 2000, the no-cloud SSR exhibits a stabilization where the aerosol emissions continue to decrease. It is unclear what parts of the simulation these inconsistencies may be attributed to.

5.6 Apparent effect of aerosols on observed and simulated SSR

The purpose of this section is to get a sense of the *apparent* effect of the sum of emitted aerosols and precursors on SSR, in both observations and simulations. To estimate

these apparent effects, the following computation is made:

$$\text{Apparent effect} = \frac{\Delta(\text{NO-CLOUD SSR})}{\Delta(\text{EMISSIONS})} \tag{5.1}$$

This value allows for comparison and quantification of the difference between regions and periods and between observations and simulations. Table 5.1 shows the result of these computations, made for periods of time when the general trend in no-cloud SSR may be argued to have been caused by a trend in aerosol emissions. In other words, during the periods chosen, trendlines of no-cloud SSR and emissions are anticorrelated. See Figure 5.2 for the observed no-cloud SSR trendlines, and Figure 5.10 for the CMIP6 no-cloud SSR trendlines.

Looking first at observations (in Table 5.1), it is clear that China has an order of magnitude stronger apparent effect than any other region, based on observations. Europe's apparent effect is the lowest. These variations between regions could have been due to the different general levels of aerosols in the periods chosen. It is known that the effect of aerosols on SSR is higher when the aerosol load is lower, and vice versa (Boucher 2015). In China, the emissions of aerosols started quite low in 1961 (as shown in "emission span" column in Table 5.1), as opposed to Japan, Europe and the United States, and this could serve as an explanation for the higher effect upon SSR in China. However, Table 5.1 also shows that the opposite is true in the United States. There, the effect of aerosol emissions on SSR is slightly higher between 1961 and 1975 than it is between 1996 and 2014 – even though the United States reached its peak emissions during the 1970s, and mean emissions were lower during the period 1996-2014 (see "emission span" column in Table 5.1). It is possible that the change in emissions is not large enough in the United States between the periods 1961-1975 and 1996-2014 for this effect to be noticeable here, and the uncertainty of the measured data is also an important factor to keep in mind. The small difference between the two periods in the United States might thereby be due to the limited accuracy of the data studied, or possibly changes in the composition of the aerosol sum.

It was previously concluded (in Section 5.3) that CMIP6 simulations are unable to reproduce the correct dimming and brightening trends in China, Japan and the United States during 1961-2014, but that the European SSR trend is fairly well reproduced. The

REG.	PERIOD	EMISSION SPAN $[\frac{\text{Gg}}{\text{yr m}^2}]$	OBSERVATIONS $\frac{\Delta\text{(NO-CLOUD SSR)}}{\Delta\text{(EMISSIONS)}}$ $[\frac{\text{W}}{\text{Gg/yr}}]$	CMIP6 $\frac{\Delta\text{(NO-CLOUD SSR)}}{\Delta\text{(EMISSIONS)}}$ $[\frac{\text{W}}{\text{Gg/yr}}]$
China	1961-1988	from 2×10^{-9} to 6×10^{-9}	-1.2×10^{10}	-1.6×10^{9}
Japan	1961-1972	from 2×10^{-8} to 3×10^{-8}	-4.3×10^{9}	-9.7×10^{8}
Europe	1995-2005	from $[9-10] \times 10^{-9}$ to $[6-7] \times 10^{-9}$	-5.8×10^{8}	-8.7×10^{8}
U.S.	1961-1971	from $[8-10] \times 10^{-9}$ to 1×10^{-8}	-6.4×10^{9}	-5.8×10^{8}
	1996-2014	from $[7-8] \times 10^{-9}$ to 4×10^{-9}	-3.6×10^{9}	-4.2×10^{8}

Table 5.1: Apparent effects of emissions of aerosols and precursors on no-cloud SSR, computed from ngGEBA observations, CRU TS v4.02 cloud cover, CMIP6 SSR and the 2020 pre-release and CMIP6 CEDS aerosol emissions. Regions are China, Japan, Europe and the United States (U.S.), and periods are chosen based on constancy in observed trend of no-cloud SSR and emissions. All periods in the observations computations are also included in the CMIP6 computations, to allow for a like-for-like comparison. The emission span approximations are made from the CMIP6 CEDS and the 2020 pre-released CEDS, which mostly agree on general level of emissions. The procedure to compute no-cloud SSR is described in Section 4.6.

apparent effects in CMIP6 and observations listed in Table 5.1 offers an explanation: Whereas all regions except Europe exhibit a *lower* apparent effect in CMIP6 than in observations for the same time periods, the simulated apparent effect for Europe is *higher* in CMIP6 compared to observed. This undermines the possibility that the cause of bias in regions other than Europe is simply erroneous emission inventory, and suggests that there are substantial regional differences in how the radiative effects of emissions are computed in ESMs.

That said, the apparent effects listed in Table 5.1 cannot indicate what the actual causes of ESM bias are, since they are calculated from model output: The apparent effects are not some ESM input variable that can easily be changed – it is computed from variables that result from the simulations. However, this analysis does somewhat narrow down the potential causes of bias, and it weakens the hypothesis that the problem lies mainly in input variables such as emission inventory.

Chapter 6

Conclusions

This final chapter summarizes the main findings of this work, and suggests topics and methods for future research related to this thesis' subject matter.

6.1 Main findings

The regions in question were China, Japan, Europe and the United States, and the period studied was 1961-2014. Following are the main conclusions of the present thesis:

1. In general, observed all-sky SSR trends were weakened by cloud cover, but long-term trends in SSR were not caused by cloud cover variations. However, certain SSR trends were found to have been almost completely masked by cloud cover: In China, Japan and Europe, a renewed dimming trend after 2000 was found when removing the effects of cloud variations from the SSR trends, and in the United States, a brightening after 1995 was found.

2. Aerosol emissions appear to have caused the dimming early in the time period in China, Japan and the United States, but not Europe, where the initial dimming is not completely captured by the ngGEBA data. The trends following the initial dimming were not found to be directly connected to aerosol emission trends in Japan, Europe and the United States. However, composition changes in the aerosol emissions may to a degree be able to indicate the brightening

in all regions except China. In China, the brightening trend in the 1990s seen in ngGEBA cannot be explained by the aerosol emission trend. However, recent papers claim the Chinese SSR data contains due to a transition to new instrumentation. An attempt to crudely correct for this transition illustrates that the no-cloud SSR trends can mostly be attributed to the aerosol emission trend.

3. It was found that Earth System Models (ESMs) remain unable to reproduce the magnitude of observed trends in all-sky SSR in China, Japan and the United States, but that they are able to closely simulate observed dimming and brightening in Europe. This regional difference in ability to reproduce observed trends was further investigated (see point 6 for conclusions).

4. Simulated cloud cover was found to weaken simulated dimming trends, and to strengthen simulated brightening trends.

5. Input aerosol emissions were found to mirror the trends in simulated clear-sky SSR in China, Europe and the United States, suggesting causality in the simulations. In Japan, the simulated no-cloud SSR was found to exhibit no anticorrelation with the aerosol emission trends, suggesting that the no-cloud SSR trend in Japan is largely affected by simulated transport of aerosols.

6. The apparent effect of input aerosol emissions on SSR was found to be much larger in Europe than the other regions, which serves as an explanation why the European SSR trends are simulated well, but none of the others are.

6.2 Further study

More studies are necessary in order to fully uncover the mechanisms behind observed dimming and brightening and to understand the continuing biases in ESM simulations, as the relative roles of aerosols and clouds are still not completely clear for the dimming/brightening periods in different regions. A tough challenge in this field of study is the lack of data coverage, and the necessity to use proxy measurements and synthetic data. Therefore, it is especially important to continually assess the quality of measured data of radiation, clouds and aerosols. This section provides concrete ideas for further study related to the theme of this thesis.

6.2.1 Data assessment and improvement

This study has made use of several different sources of data, many of them with global coverage. However, as discussed earlier, a lot of the data has synthetic components, or is based on proxy measurements, and this poses an uncertainty issue. In the opinion of the present author, further studies are necessary to assess the validity and accuracy of the datasets used in this thesis. Ideas for study and improvement are listed below:

- Investigation of cloud cover data in CRU: The cloud cover data used in this thesis, from CRU TS v4.02 – while unique in its time range and areal coverage – is highly uncertain. The sources of cloud data are varied throughout the period, and the cloud cover is measured and computed in several different ways. As explored in the appendices(Section E.2), one of the proxies used to compute cloud cover is sun hours, which is intrinsically problematic because a sun hour cannot be recorded when there are sufficiently high amounts of aerosols present in the atmosphere. Thus, the cloud cover data computed from sun hours also includes high pollution periods. Another proxy used is diurnal temperature range, which can be uncertain due to changes in the greenhouse effect, which has a direct effect on the diurnal temperature range. Therefore, it is necessary to do a substantial investigation into the cloud cover data in CRU, to analyze the possibility that these proxies give biased cloud cover values in CRU. Such an analysis would allow for a recreation of the data set, taking into account these sources of error.

- Investigation of the robustness of machine learning used to create ngGEBA: The SSR data used in this thesis, while based on the Global Energy Balance Archive, is filled in using machine learning. Thus, the data set (dubbed ngGEBA in this thesis) is partly synthetic. However, it has not been analyzed properly for robustness, and this should be done in order to verify its validity. In this effort, a paper should be published along with the data set itself, in order for the scientific community to be able to make use of it.

- Interpolation of GEBA onto a grid: The GEBA data set is a station-based data set, and the possibility should be explored for interpolating the data onto a continental grid. A successful gridding of GEBA would provide the scientific community with a highly valuable resource for the purpose of studying aerosols

and clouds and their effects on radiation, among many other applications.

6.2.2 Further analysis

The analysis in this thesis was limited in its ambition due to time limitations applied to master thesis projects. However, several ideas for further analysis have appeared during the writing of the thesis, and these ideas are listed below:

- Improvements to the no-cloud SSR computation: The computation of no-cloud SSR could be improved upon, taking into account differences and changes in cloud optical depths around the world. As described in Matuszko 2012, different cloud types heavily influence the SSR below a cloud. Since different cloud types are more or less prevalent depending on the local climate, the assumption made here of a certain average "cloud SSR" for all regions is clearly erroneous. It would be interesting to find out how sensitive the conclusions made here are to improvements upon the method of computation of no-cloud SSR.
- Analysis of more regions: In this study, China, Japan, Europe and the United States were analyzed. One issue with performing the analysis with more of a global coverage is, however, the limited spatial coverage of ngGEBA in many regions (see Figure 4.1 in Methods chapter).
- Analysis of more CMIP6 model products: This thesis exclusively studied historical runs of all-sky SSR, clear-sky SSR and cloud cover, which has limited potential in terms of conclusive results regarding cloud cover. For instance, there exists more resolved cloud information than cloud cover fraction, such as column liquid- and ice water path, which could enlighten the study of cloud effects on SSR.
- A study of the correlation between aerosol emissions and aerosol optical depth (AOD): There exist gridded datasets of AOD for recent decades (satellite era) which can be compared to aerosol emissions in order to find out how good of a proxy emissions are in different regions. This could either strengthen or weaken conclusions about the effect of aerosols on SSR in years prior to the satellite era, based on how good of a proxy emissions are found to be.

Appendix A

Additional figures

A.1 No-cloud/all-sky comparison: Varying cloud SSR

This section provides figures comparing ngGEBA all-sky SSR and ngGEBA no-cloud SSR, equivalent to those shown in Section 5.1, except with three different assumptions for the constant cloud SSR. To facilitate for comparison with the cloud SSR utilized in Section 5.1, 109 W/m² is reproduced here, along with 90 W/m² and 128 W/m². It should be noted that the figures for Europe (Figure A.3) and the United States (Figure A.4) have re-scaled axes in this appendix, as this allows for more detailed analysis of the trends in Europe and the United States than was possible when all vertical scales were identical. However, this means that the apparent magnitudes of variations in the figures are not directly comparable to those for China (Figure A.1) and Japan (Figure A.2).

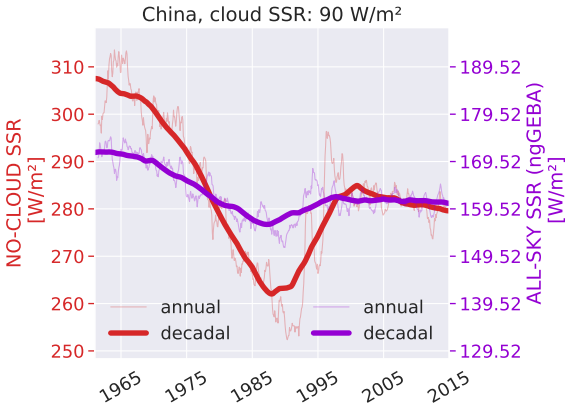

(a) Cloud SSR=90

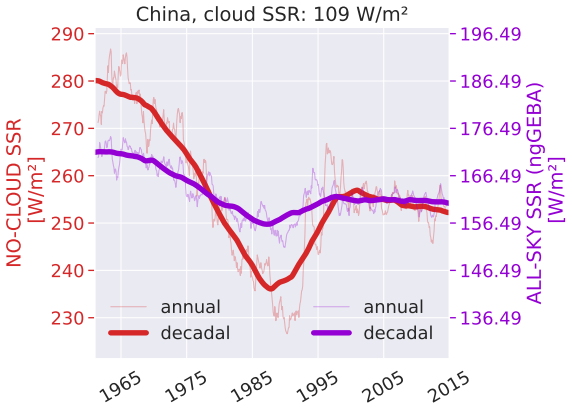

(b) Cloud SSR=109

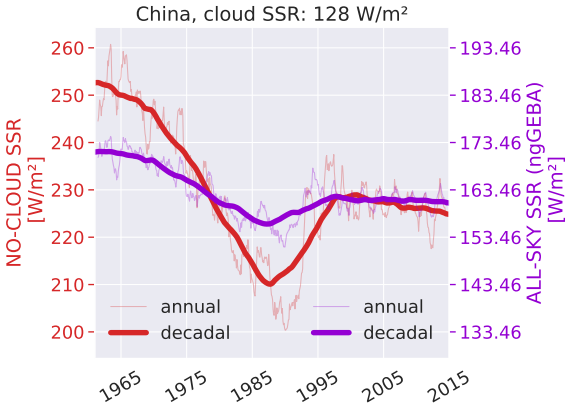

(c) Cloud SSR=128

Figure A.1: China

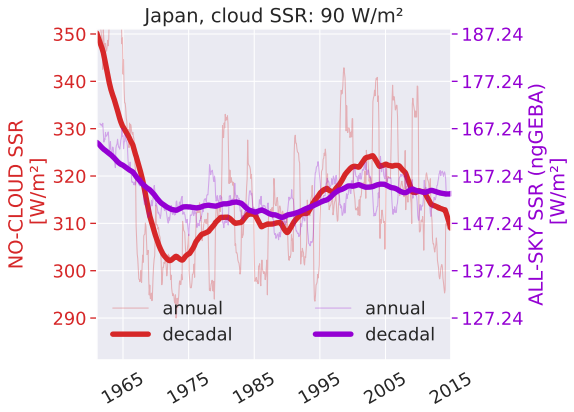

(a) Cloud SSR=90

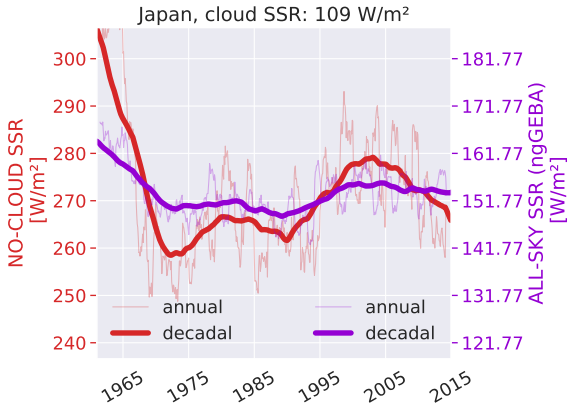

(b) Cloud SSR=109

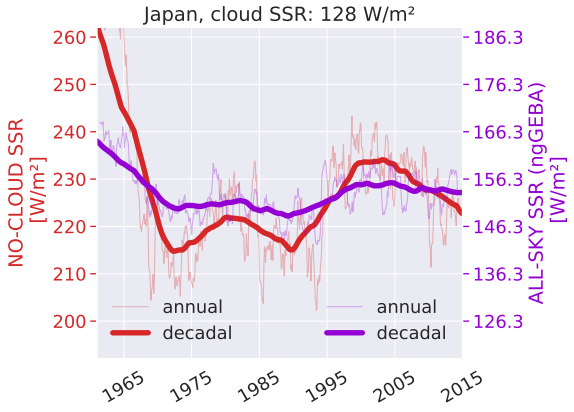

(c) Cloud SSR=128

Figure A.2: Japan

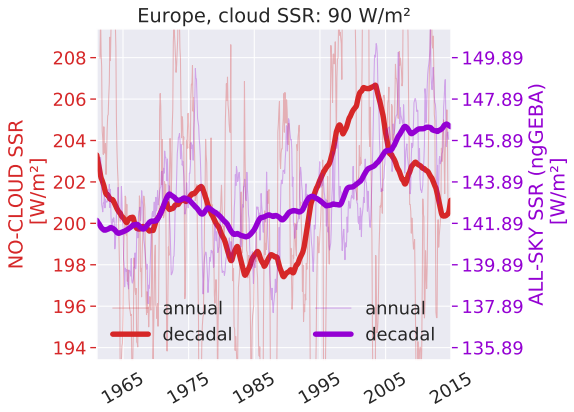

(a) Cloud SSR=90

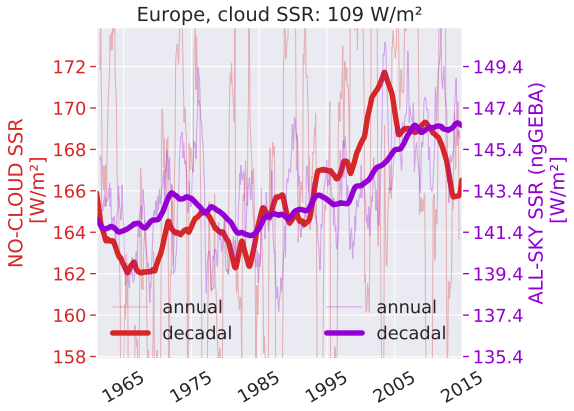

(b) Cloud SSR=109

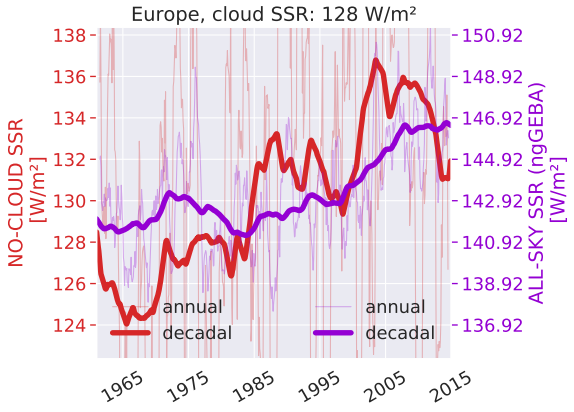

(c) Cloud SSR=128

Figure A.3: Europe

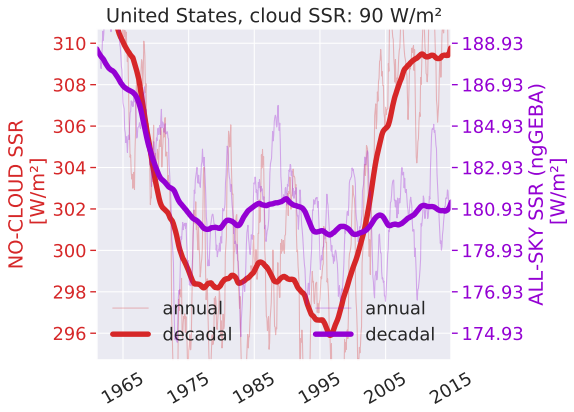

(a) Cloud SSR=90

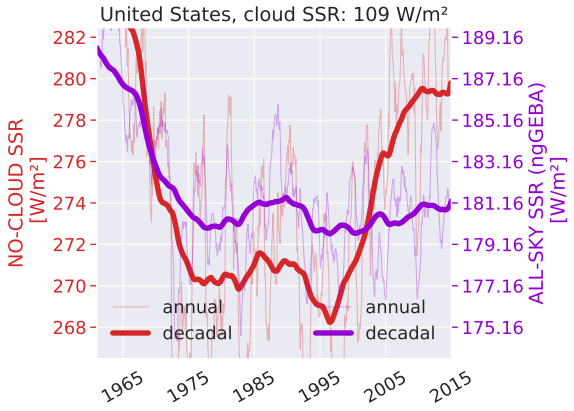

(b) Cloud SSR=109

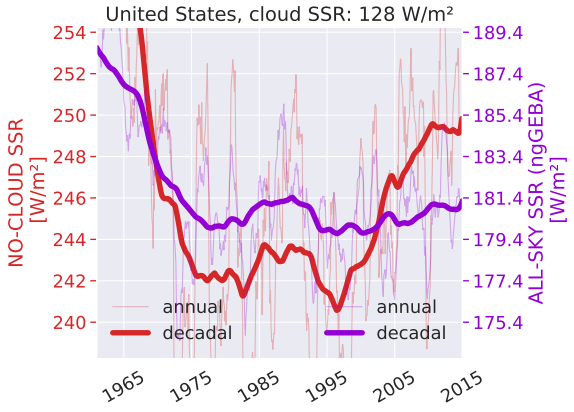

(c) Cloud SSR=128

Figure A.4: The United States

A.2 No-cloud SSR compared with each aerosol/precursor species

This section includes figures comparing no-cloud SSR trendlines to trendlines of emissions of each of the aerosol/precursor species not included in Section 5.5. The following figures are equivalent to those included in Section 5.2, only with aerosol species SO_2, NO_x and NMVOC.

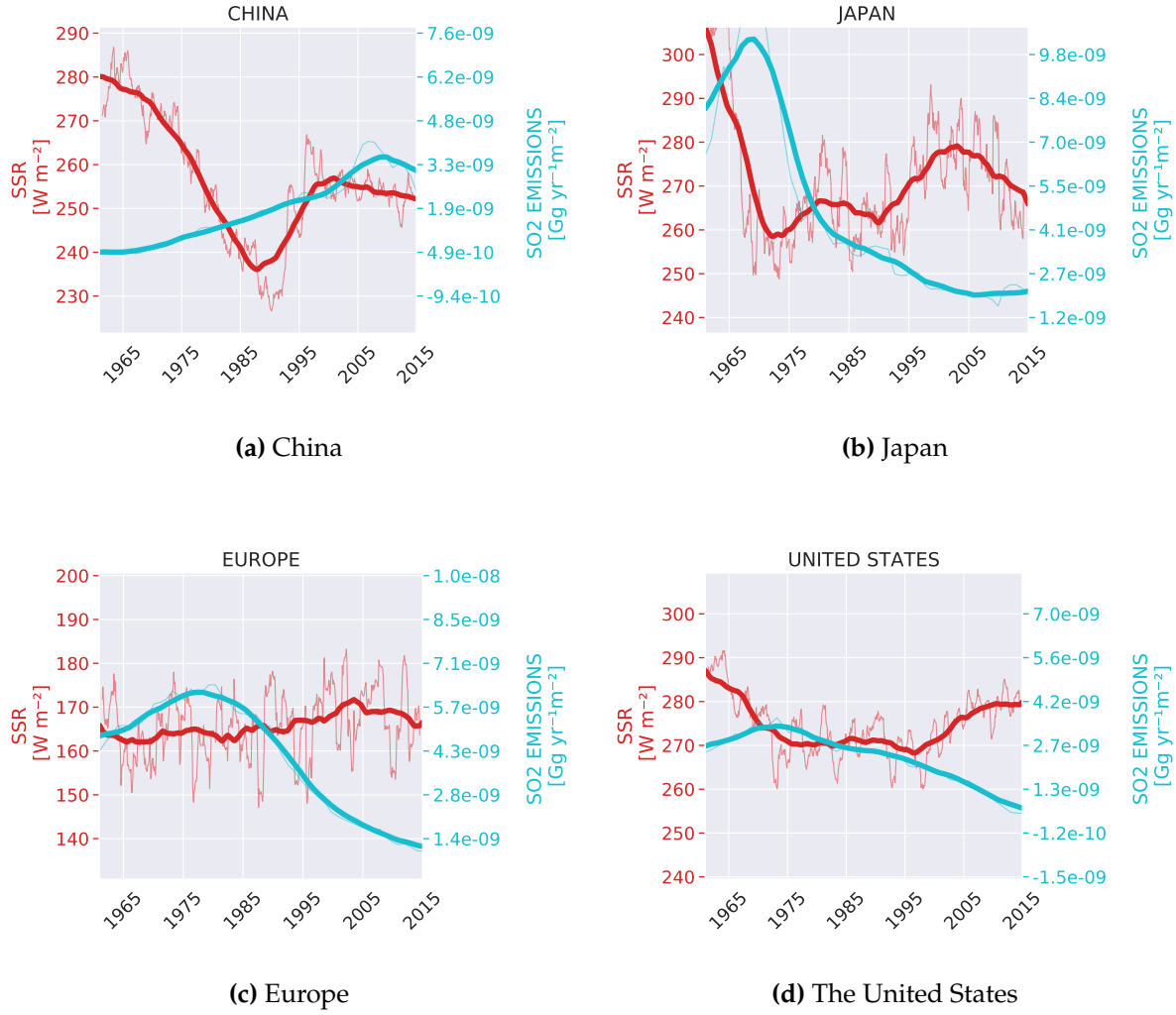

(a) China

(b) Japan

(c) Europe

(d) The United States

Figure A.5: No-cloud SSR trendlines from ngGEBA shown in red, with decadal running average in boldface and annual running average in lightface. Decadal trend in annual SO2 emissions from 2020 CEDS are shown in cyan.

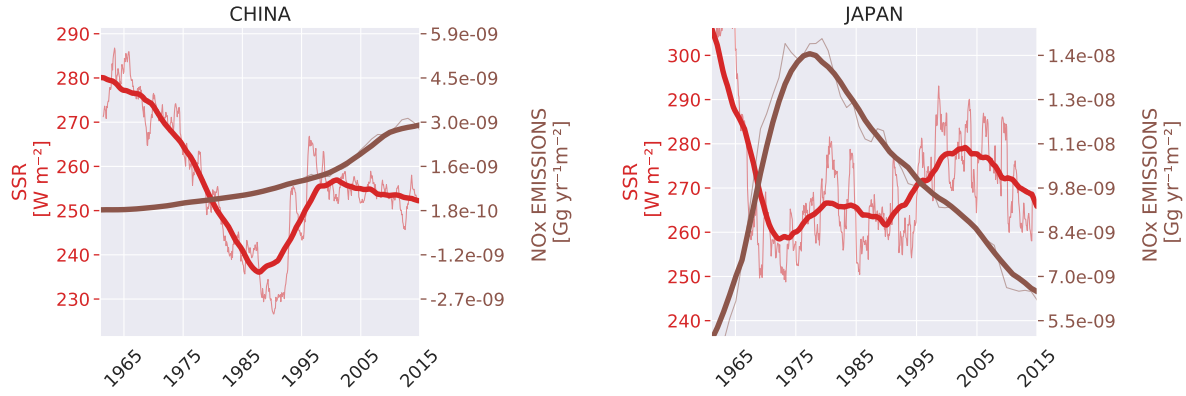

(a) China

(b) Japan

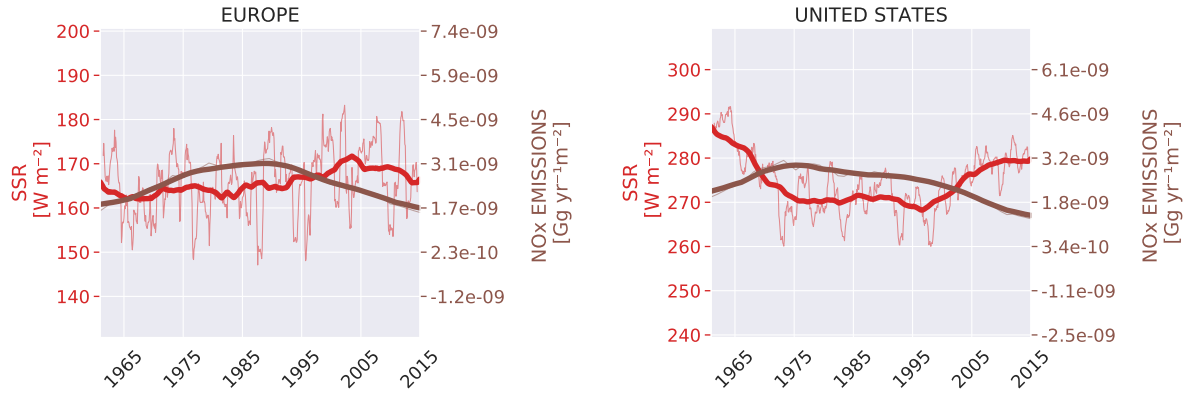

(c) Europe

(d) The United States

Figure A.6: No-cloud SSR trendlines from ngGEBA shown in red, with decadal running average in boldface and annual running average in lightface. Decadal trend in annual nitrogen oxide (NOx) emissions from 2020 CEDS are shown in brown.

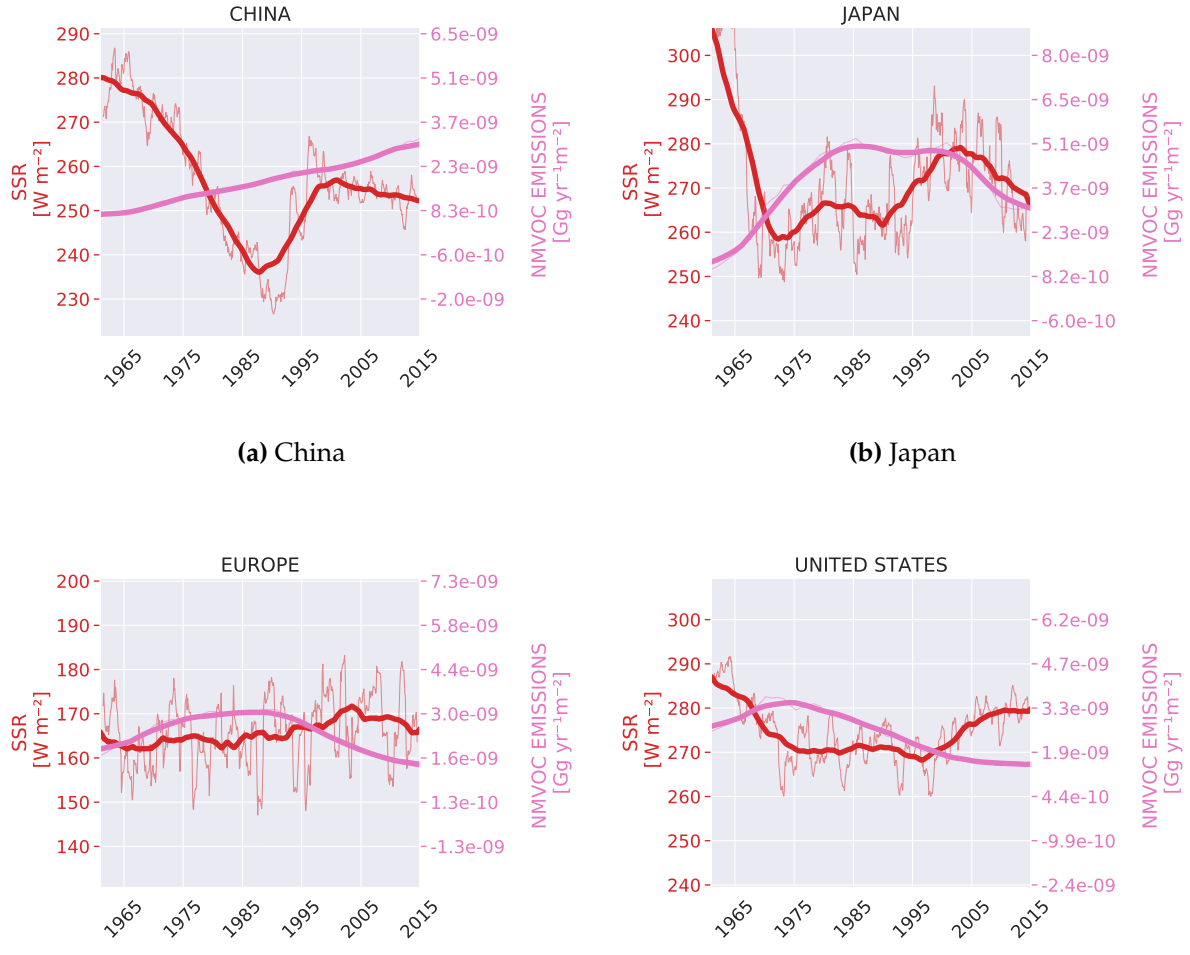

(a) China

(b) Japan

(c) Europe

(d) The United States

Figure A.7: No-cloud SSR trendlines from ngGEBA shown in red, with decadal running average in boldface and annual running average in lightface. Decadal trend in annual non-methane volatile organic compound (NMVOC) emissions from 2020 CEDS are shown in pink.

A.3 No-cloud compared to all-sky using ISCCP

This section shows the same analysis of all-sky and no-cloud SSR using ngGEBA as shown in Section 5.1, except in this appendix section ISCCP is used as the source of cloud cover data to produce the no-cloud SSR. The procedure to create no-cloud SSR from SSR and cloud cover data is described in Section 4.6. Here, the constant cloud SSR is set to 109 W/m².

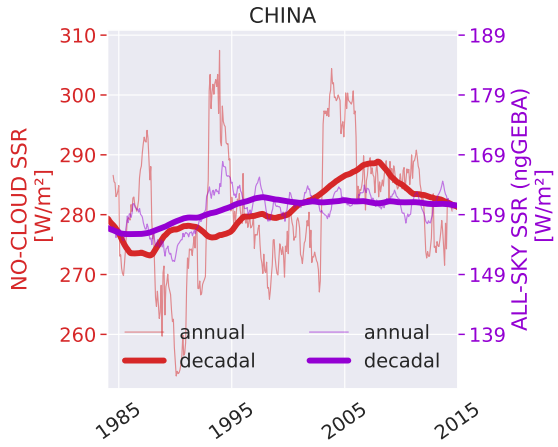

(a) China

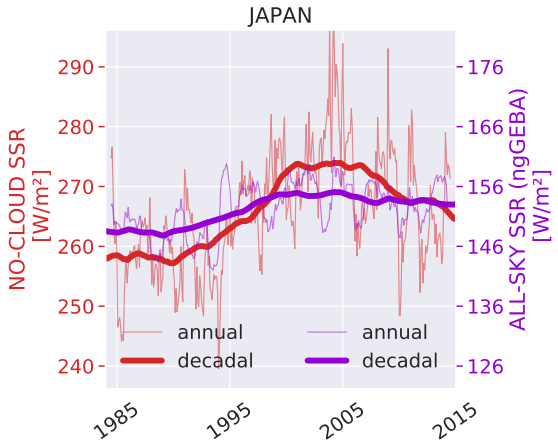

(b) Japan

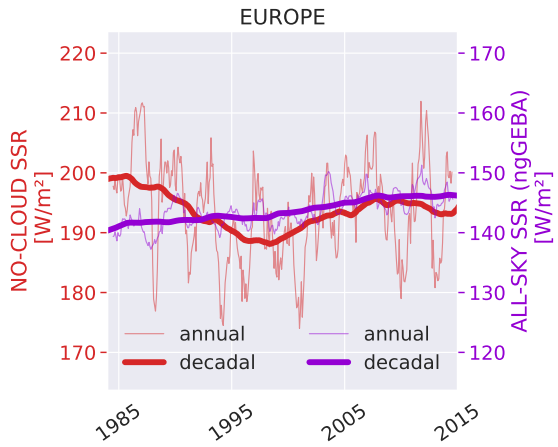

(c) Europe

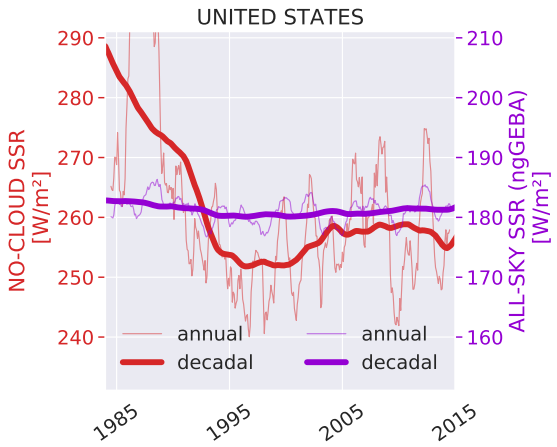

(d) The United States

A.4 Simulated cloud cover anomalies

This section shows the evolution of cloud cover in observations and simulations.

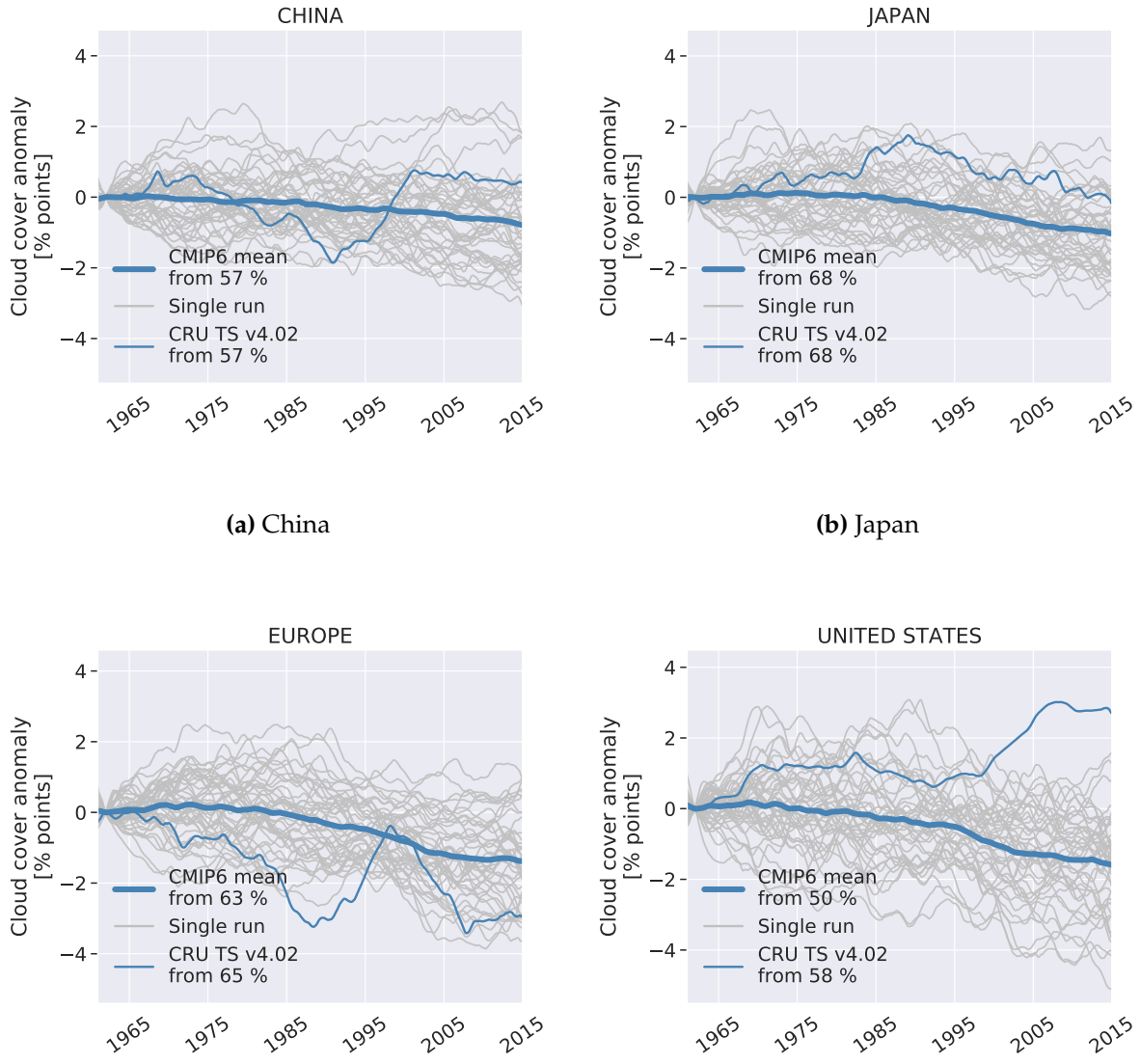

(a) China

(b) Japan

(c) Europe

(d) The United States

Figure A.9: Decadal running means of mean simulated (CMIP6) and observed (CRU TS v4.02) cloud cover anomalies between 1961 and 2014 at ngGEBA stations in four regions. Mean CMIP6 in boldface and CRU TS v4.02 in lightface. Grey lines are decadal running means of each model run included. The anomalies are computed by averaging the initial 5 years of the running mean time series (this average is printed after "from" in each legend item), and subtracting this mean value from each subsequent time step. Included in the computation is one CMIP6 simulation (r1i1f1p1) from each of the 42 models tabulated in Table B.1 in Appendix B.

Appendix B

Sources of data

This appendix provides the sources of the data used within this thesis. Per the completion of this thesis (November 2020), the links in this appendix bring the user to the sources of data. However, the present author cannot guarantee these links are live in the future.

B.1 ngGEBA and GEBA

ngGEBA is not published online. Per the completion of this thesis, this data set is only available upon request from Trude Storelvmo (trude.storelvmo@geo.uio.no).

The original GEBA data set is available for download upon registration and request on ETH Zürich's website. Original GEBA includes more stations than ngGEBA, but many station time series contain temporal gaps):
https://geba.ethz.ch/data-retrieval.html

B.2 CRU TS v4.02

The cloud cover data set is available from the University of East Anglia's website:
https://crudata.uea.ac.uk/cru/data/hrg/

B.3 ISCCP H-series

The satellite-based cloud cover data is available for download from the NOAA website (for the same data used herein, choose “ISCCP HGM/HGH”):
https://www.ncdc.noaa.gov/isccp/isccp-data-access/isccp-data

B.4 CEDS Emissions data

CEDS gridded aerosol emissions data for CMIP6 is available for download from the ESGF website "input4MIPs Data Search" (the variables studied herein are “SO2_em_anthro”, “BC_em_anthro”, “NH3_em_anthro” and “OC_em_anthro”):
https://esgf-node.llnl.gov/search/input4mips/

Regionally summed emissions of the 2020 pre-release of CEDS are available as CSV files from the CEDS GitHub on the following URL: https://github.com/JGCRI/CEDS/.

B.5 CMIP6 Data

The historical data from CMIP6 ESMs can be downloaded from the ESGF website "cmip6 Data Search" (for the same data used herein, choose Experiment ID "historical", Variant Label "r1i1p1f1", Table ID "Amon", Frequency "mon" and Variables "rsds", "rsdscs" and "clt"):
https://esgf-node.llnl.gov/search/cmip6/

Table B.1 contains all ESMs included in this thesis, along with their respective nominal resolutions.

ESM name	Nominal resolution	ESM name	Nominal resolution
CESM2-FV2	250 km	KIOST-ESM	250 km
CESM2-WACCM-FV2	100 km	MPI-ESM1-2-LR	250 km
FGOALS-g3	250 km	INM-CM4-8	100 km
E3SM-1-0	100 km	INM-CM5-0	100 km
FGOALS-f3-L	100 km	MPI-ESM-1-2-HAM	250 km
NESM3	250 km	IITM-ESM	250 km
SAM0-UNICON	100 km	MPI-ESM1-2-HR	100 km
BCC-CSM2-MR	100 km	AWI-ESM-1-1-LR	250 km
CanESM5	500 km	CMCC-CM2-HR4	100 km
MRI-ESM2-0	100 km	AWI-CM-1-1-MR	100 km
CESM2-WACCM	100 km	CMCC-CM2-SR5	100 km
CESM2	100 km	TaiESM1	100 km
MIROC6	250 km	IPSL-CM6A-LR	250 km
BCC-ESM1	250 km	ACCESS-CM2	250 km
E3SM-1-1	100 km	ACCESS-ESM1-5	250 km
ESM2-0	100 km	GFDL-ESM4	100 km
GISS-E2-1-G	250 km	NorESM2-LM	250 km
GISS-E2-1-H	250 km	NorESM2-MM	100 km
KACE-1-0-G	250 km	EC-Earth3	100 km
E3SM-1-1-ECA	100 km	EC-Earth3-Veg	100 km
CIESM	100 km	EC-Earth3-Veg-LR	250 km

Table B.1: The 42 Earth System Models (ESMs) that are analysed in this thesis. All these ESMs participate in CMIP6 and have provided historical runs for surface solar radiation, clear-sky surface solar radiation and cloud area fraction. For each model, one ensemble member has been included in the analysis in this thesis, r1i1f1p1.

Appendix C

Python scripting

The data parsing, processing and visualization herein has been performed exclusively using Python and Python packages. This appendix presents some of the most important methods used for handling the data with Python. It should be noted that the present author cannot guarantee for future behavior of these packages and libraries.

C.1 Collocation using xarray

All time series analyzed herein are collocated with the ngGEBA station data. The datasets are first opened and made into Datasets using the xarray (Hoyer and Hamman 2017) library function "open_mfdataset". Furthermore, the resulting Dataset is collocated with the ngGEBA stations using a Nearest Neighbour method: xarray's "nearest". The following bit of Python code shows the general procedure:

```
import xarray as xr
# geba_lats are geba latitudes; geba_lons are geba longitudes
data=xr.open_mfdataset("dataset.nc")
data=data.sel(lat=geba_lats, lon=geba_lons, method='nearest')
```

C.2 The pandas library

Dataframes were created using the pandas library (Development Team 2020). Dataframes are useful in that many different timeseries can be put into the same system,

which often makes a code neat and easy to read. Also, computations can easily be performed on the whole system at once (e.g. to look for correlation coefficients).

The pandas library is also highly compatible with xarray Datasets, and many pandas functions can be directly utilized on xarray Datasets. An example of this compatibility is the usage of the pandas function *rolling* on an xarray Dataset in Section C.3 below.

C.3 Computing decadal and annual running means

The pandas library contains a function for computing running means from DataFrames or Series. This function has been utilized herein to compute the running means in each plot. Following is the general procedure used in this thesis to create a decadal mean of the variable "variable" from the xarray Dataset "data", which has a monthly resolution:

```
import pandas as pd
timeseries=data['variable']
annual=timeseries.rolling(window=12,center=True).mean()
decadal=annual.rolling(window=12*10,center=True,min_periods=12).mean()
```

The reason why the decadal running mean is computed from the annual running mean, is for the purpose of handling the endpoints of the timeseries, where the decadal mean cannot be computed. The parameter "min_periods" determines the minimum number of data points necessary to include in the running mean at the endpoints. By computing the decadal mean from the annual mean, one ensures that the endpoints are only as noisy as the annual mean is.

C.4 Computing anomalies

In this thesis, anomaly plots have been used in order to highlight the evolution of two variables against each other, regardless of their starting level. Anomalies can be computed in different ways, but only one method is used in this work: First, the initial 5 years of the timeseries is averaged, and second, this initial average is substracted from each subsequent time step. Following is an example script, where the pandas Series "timeseries" contains data between 1961 and 2014:

```
import pandas as pd
initial_mean=timeseries[:'1966'].mean()
anomaly_timeseries=timeseries-initial_mean
```

C.5 Plotting and styling of plots

To create figures, the matplotlib package (Hunter 2007) was used. The styling of the plots was performed using the seaborn library (Waskom et al. 2017). Example code:

```
import matplotlib.pyplot as plt
sns.set(font_scale=1.5) #the font_scale ensures large font on plots
sns.set_style("dark",{"xtick.bottom":True});
sns.set_style({"ytick.left": True})
```

Appendix D

Terminology

D.1 Glossary

Aerosol optical depth (AOD): The optical depth due to aerosol presence. This value can be computed for different wavelengths of radiation, and then quantifies the amount of downwelling radiation of that wavelength that is extinguished by aerosols in the atmospheric column. The aerosol optical depth is affected differently by aerosol species of different optical properties.

Brightening: An increasing trend in SSR, often referring to the specific such trend observed between the 1980s and present day in certain regions of the world.

Coupled Model Intercomparison Project, Phase 6 (CMIP6): Sixth version (phase) of a project organized by the World Climate Research Programme, meant to compare results from different climate models by designing specific experiments for each models to conduct. The next assessment report (AR6), which contains published work based on CMIP6, is planned for publication in 2021.

Dimming: Also called "global dimming": A decreasing trend in SSR, usually referring to a specific such trend observed globally between the 1950s and the 1980s. The label "global" in "global dimming" comes from the term global radiation, which is the sum of direct and diffuse radiation. For clarity in this thesis, global dimming is usually called "dimming".

Optical depth: The amount of downwelling radiation that is extinguished by

atmospheric particles and gases. Can be computed from SSR data using the Beer-Lambert law, see Chapter 2.

Surface solar radiation (SSR): The amount of radiation that reaches the surface. It is defined in terms of power per area, usually with the unit W/m^2.

D.2 Acronyms

ACI: Aerosol-cloud interactions

AOD: Aerosol optical depth

AR5: Assessment Report 5 by the IPCC, published in 2014.

ARI: Aerosol-radiation interactions

ASI: Aerosol-surface interactions

BC: Black carbon

CEDS: Community emissions data system

CMIP5: Coupled Model Intercomparison Project, phase 5.

CMIP6: Coupled Model Intercomparison Project, phase 6.

CRU: Climatic Research Unit (of the University of East Anglia)

CRU TS: Climatic Research Unit time series

ESM: Earth System Model

GEBA: Global Energy Balance Archive

IPCC: Intergovernmental Panel on Climate Change

ISCCP: International Satellite Cloud Climatology Project

LOESS: Locally estimated scatterplot smoothing

OC: Organic carbon

SSR: Surface solar radiation

SST: Sea surface temperature

TOA: Top of the atmosphere

Appendix E

Cloud cover data investigation

E.1 Relevance of cloud cover data

CRU TS v4.02 dataset is used as the source of cloud cover data in the main body of this thesis. It has a unique temporal coverage, containing data from 1901 until present day. In this section, CRU is compared to satellite data from ISCCP, which has data between mid-1983 and 2017. The regions that are investigated in this thesis are China, Japan, Europe and the United States, due to the relatively good coverage of ngGEBA stations in these regions. The cloud cover datasets are collocated and averaged over the station locations.

Figure E.1 shows comparisons between CRU and ISCCP for the four regions. Generally, it is obvious that there are large discrepancies in the level of cloudiness between the two datasets. In China, Japan and the United States, ISCCP shows a much higher cloud cover than CRU, and in the Europe, ISCCP shows a generally lower cloud cover than CRU. As is revealed from the correlation coefficients printed at the top of each subfigure in Figure E.1, the trends are also not correlated across the regions, except in Japan. This comparison between CRU and ISCCP does not substantiate the validity of CRU.

This discussion induces doubt in the accuracy of CRU TS v4.02, if one assumes that ISCCP offers better or more accurate data at the ngGEBA sites. Now, it is also necessary to determine the quality of each of the datasets individually. Following is such an

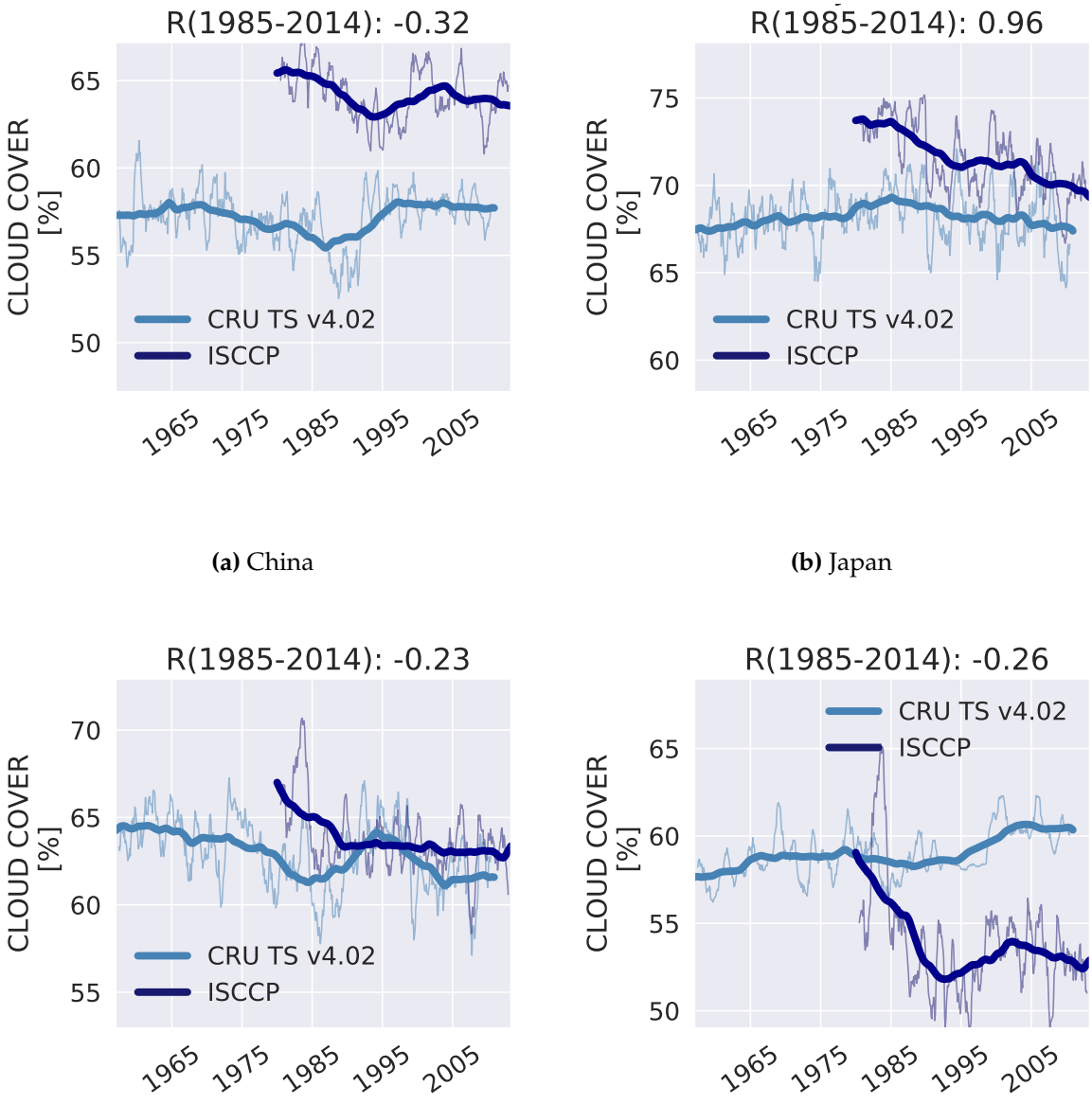

(a) China

(b) Japan

(c) Europe

(d) The United States

Figure E.1: Comparison of CRU TS v4.02 cloud cover time series (1961-2014) and ISCCP cloud area fraction time series (1984-2017) collocated to ngGEBA station locations in four regions. Pearson's correlation coefficient (R) computed between the decadal running mean trendlines is shown above each figure.

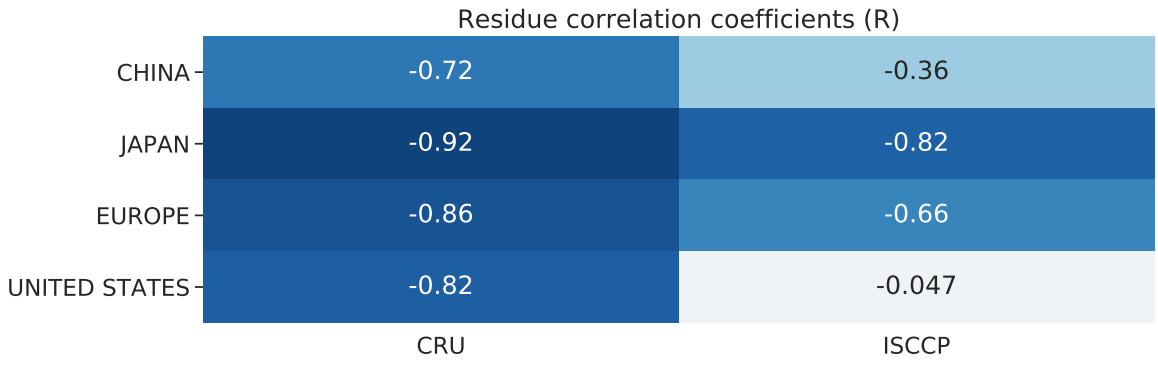

Figure E.2: Pearson's correlation coefficient between computed residues (annual running average time series minus decadal running average time series) from ngGEBA SSR time series and cloud cover from (left) CRU TS v4.02 and (right) ISCCP at ngGEBA stations in China, Japan, Europe and the United States. Computed from trends created for the period 1985-2014.

assessment, utilizing the SSR data from ngGEBA.

There is an obvious relationship between SSR and cloud cover: Higher cloud cover will cause the SSR to be lower than in clear-sky conditions. Considering other atmospheric components that affect SSR, these do not change quickly enough to have the short-term effect that clouds have. Therefore, after removing long-term variations, Pearson's correlation coefficient should be close to -1 between SSR and cloud cover. A computation of the correlation coefficient should in other words uncover an anticorrelational relationship between two collocated datasets of cloud cover and SSR. As such, this computation can indicate the relevance of a cloud cover dataset in a case where the SSR data is assumed accurate. It should be noted, though, that a correlational relationship between short-term SSR and cloud cover could in theory be an artifact, due to the measurement method of either variable.

Figure E.2 shows Pearson's correlation coefficient between SSR residues and cloud cover residues (annual average time series minus decadal average time series). These results substantiate the validity of CRU cloud cover for the purpose of this analysis, because the relationship between SSR and CRU at ngGEBA stations is quite clearly anticorrelational. However, SSR and ISCCP do not exhibit an equally clear anticorrelational relationship, which undermines the validity of ISCCP cloud cover at ngGEBA stations.

An explanation of why ISCCP does not anticorrelate with ngGEBA in the short-term may have to do with the fact that ngGEBA is station data. ISCCP is a gridded dataset with satellite imagery as its source, where the entire areas of the gridboxes are weighted to the same degree. CRU, on the other hand, is based on station data like ngGEBA, and the majority of stations are located in the same general areas as the ngGEBA stations. It should therefore be noted that this comparison between CRU and ISCCP is strictly relevant for the locations of ngGEBA stations, and in the regions studied herein. Furthermore, this analysis cannot be viewed as a complete evaluation of the differences and relative quality of the two datasets.

Nonetheless, for the analysis in this thesis, the cloud cover data from CRU is arguably superior to that from ISCCP, since the objective is to look for relationships between cloud cover and SSR. The source of cloud cover data in the main body of this thesis is CRU. However, Section A.3 contains some analysis where ISCCP is used as the source of cloud cover data.

E.2 Sun hour conversion: Maximum optical depth for a "cloud"

As stated when introducing CRU in Section 4.1.2, the CRU cloud cover data is partly based on proxies from sun hour measurements. It should be noted that it is unclear what fraction of CRU data is based on these measurements in the period 1961-2014.

The conversion procedure between sun hours and cloud cover is as follows: First, the daily sun hours are converted to sun fraction by dividing by the maximum possible sun hours. Thereafter, sun fraction is converted to cloud cover percentage (Harris, Jones et al. 2014). The procedure to convert from sun fraction to cloud cover is reproduced in Table E.1. Each calculation goes via cloud cover oktas, but is converted to percentage by the very last factor. This means that the fraction of CRU which is computed from sun hours is a measure of the percentage of daytime during which the measuring instrument is in the shadow of a cloud. What constitutes a sun hour in CRU is important to note, because for those stations at which the cloud cover is derived from sun hours, a sun hour indirectly defines how thick the optical depth must be in order

if sun frac >= 0.95	cloud cover = 0.0 [%]
if 0.95 > sun frac > 0.35	(0.95-sun frac)*100*(10/8) [%]
if 0.35 > sun frac >= 0.15	((0.35-sun frac)*50+60)*(10/8) [%]
if 0.15 > sun frac > 0.00	((0.15-sun frac)*100+70)*(10/8) [%]
maximum cloud cover is 100 %	

Table E.1: Conversion from recorded sun fraction (*sun frac*) to cloud cover in CRU TS. Adapted from Harris, Jones et al. 2014.

for a "cloud" to be recorded.

The CRU cloud cover data is partly based on sun hour measurements. Assuming WMO's guidelines for measurements of sun hours, these instruments record sun for measurements above a threshold of 120 W/m² (WMO 2008). This, in turn, means that a recorded cloud must be thick enough that less than 120 W/m² reaches the measurement instrument. This threshold was originally set so due to this being calculated to be the average threshold for Campbell-Stokes sunshine recorders (WMO 2008). These instruments are made up of a glass bulb which focuses sunlight down on a piece of paper: Whenever the paper is burnt, sun hours are recorded, and before the next morning, the piece of paper is switched out. On average, 120 W/m² of sunlight is necessary for the sunlight to burn through the paper.

In theory, then, assuming 120 W/m² is the threshold, it is possible to calculate the necessary optical depth for a cloud to be recorded. Optical depth, as described in Section 2.1, can be defined in terms of incoming radiation. Restating the Beer-Lambert law:

$$E_{surf} = E_{toa} \exp(-\tau / \cos\phi), \tag{2.6}$$

where E_{surf} is the incoming solar radiation at the surface (what an SSR instrument would measure), E_{toa} is the incoming solar radiation at the top of the atmosphere, τ is the optical depth through the atmospheric column and ϕ is the solar zenith angle (the angle between the zenith and the Sun's center).

Rephrasing it, the optical depth is described by:

Solar zenith angle	Optical depth threshold
0°	2.4
30°	2.3
45°	2.1
60°	1.7
75°	1.1
80°	0.68

Table E.2: Idealized calculations of optical depth maxima for recording an SSR of at least 120 W/m² at different solar zenith angles. This represents a potential source of error in the usage of sun hour as a proxy for cloud cover, as described in Section E.2.

$$\tau = -\ln(\frac{E_{surf}}{E_{toa}})\cos\phi$$

Now, if the threshold for a cloud to be recorded in CRU, 120 W/m², is substituted into this equation, it reads:

$$\tau_{thres} = -\ln(\frac{120W/m^2}{E_{toa}})\cos\phi$$

Thus, for higher solar zenith angles, the optical depth threshold, τ_{thres}, will decrease accordingly. Furthermore, assuming E_{toa} to be $\cos\phi \times 1362$ W/m²:

$$\tau_{thres} = -\ln(\frac{120W/m^2}{\cos\phi \times 1362W/m^2})$$

Table E.2 shows the value of τ_{thres} computed for different solar zenith angles. The table shows AOD values that are achievable in especially polluted periods and regions, particularly for large solar zenith angles. This suggests that erroneous cloud cover measurements due to AOD may be part of the CRU cloud cover data.

Bibliography

Abakumova, GM et al. (1996). 'Evaluation of long-term changes in radiation, cloudiness, and surface temperature on the territory of the former Soviet Union'. In: *Journal of Climate* 9.6, pp. 1319–1327.

Allen, RJ, JR Norris and Martin Wild (2013). 'Evaluation of multidecadal variability in CMIP5 surface solar radiation and inferred underestimation of aerosol direct effects over Europe, China, Japan, and India'. In: *Journal of Geophysical Research: Atmospheres* 118.12, pp. 6311–6336.

Augustine, JA (2020). 'An update on brightening and dimming in the United States'. In: *EGU General Assembly Conference Abstracts*, p. 2453.

Augustine, JA and Ellsworth G Dutton (2013). 'Variability of the surface radiation budget over the United States from 1996 through 2011 from high-quality measurements'. In: *Journal of Geophysical Research: Atmospheres* 118.1, pp. 43–53.

Boucher, O (2015). *Atmospheric aerosols*. Springer.

Boucher, O et al. (2013). 'Clouds and Aerosols'. In: *Climate Change 2013: The Physical Science Basis. Contribution of Working Group I to the Fifth Assessment Report of the Intergovernmental Panel on Climate Change*. Ed. by T.F. Stocker et al. Cambridge, United Kingdom and New York, NY, USA: Cambridge University Press. Chap. 7, pp. 571–658. ISBN: ISBN 978-1-107-66182-0. URL: www.climatechange2013.org.

Breiman, Leo (2001). 'Random forests'. In: *Machine learning* 45.1, pp. 5–32.

Calbó, J and A Sanchez-Lorenzo (2009). 'Cloudiness climatology in the Iberian Peninsula from three global gridded datasets (ISCCP, CRU TS 2.1, ERA-40)'. In: *Theoretical and applied climatology* 96.1-2, pp. 105–115.

Charlson, Robert J et al. (1992). 'Climate forcing by anthropogenic aerosols'. In: *Science* 255.5043, pp. 423–430.

Columbia, University (2020). *The Meiji Restoration and Modernization*. http://afe.easia.columbia.edu/special/japan_1750_meiji.htm. Accessed: 2020-10-02.

Cronin, Timothy W (2014). 'On the choice of average solar zenith angle'. In: *Journal of the Atmospheric Sciences* 71.8, pp. 2994–3003.

Development Team, The pandas (Feb. 2020). *pandas-dev/pandas: Pandas*. Version latest. DOI: **10.5281/zenodo.3509134**. URL: https://doi.org/10.5281/zenodo.3509134.

Dwyer, John G, Joel R Norris and Christian Ruckstuhl (2010). 'Do climate models reproduce observed solar dimming and brightening over China and Japan?' In: *Journal of Geophysical Research: Atmospheres* 115.D7.

Hansen, James et al. (2011). 'Earth's energy imbalance and implications'. In: *arXiv preprint arXiv:1105.1140*.

Harris, Ian, Philip D Jones et al. (2014). 'Updated high-resolution grids of monthly climatic observations–the CRU TS3. 10 Dataset'. In: *International journal of climatology* 34.3, pp. 623–642.

Harris, Ian, Timothy J Osborn et al. (2020). 'Version 4 of the CRU TS monthly high-resolution gridded multivariate climate dataset'. In: *Scientific data* 7.1, pp. 1–18.

Hartmann, D.L. (1994). *Global physical climatology*. Vol. 103. Academic Press.

Hartmann, D.L. et al. (2013). 'Observations: Atmosphere and Surface'. In: *Climate Change 2013: The Physical Science Basis. Contribution of Working Group I to the Fifth Assessment Report of the Intergovernmental Panel on Climate Change*. Ed. by T.F. Stocker et al. Cambridge, United Kingdom and New York, NY, USA: Cambridge University Press. Chap. 2, pp. 159–254. ISBN: ISBN 978-1-107-66182-0. DOI: **10.1017/CBO9781107415324.008**. URL: www.climatechange2013.org.

Hoyer, Stephan and Joe Hamman (2017). 'xarray: ND labeled arrays and datasets in Python'. In: *Journal of Open Research Software* 5.1.

Hoyt, Douglas V and Kenneth H Schatten (1993). 'A discussion of plausible solar irradiance variations, 1700-1992'. In: *Journal of Geophysical Research: Space Physics* 98.A11, pp. 18895–18906.

Huang, Qunhui (2018). *China's Industrialization Process*. Springer.

Hunter, J. D. (2007). 'Matplotlib: A 2D graphics environment'. In: *Computing in Science & Engineering* 9.3, pp. 90–95. DOI: **10.1109/MCSE.2007.55**.

Jiang, Zhihong et al. (2017). 'Impact of Chinese urbanization and aerosol emissions on the East Asian summer monsoon'. In: *Journal of Climate* 30.3, pp. 1019–1039.

Juckes, Martin et al. (2020). 'Implementing FAIR Principles in the IPCC Assessment Process'. In: *EGU General Assembly Conference Abstracts*, p. 10778.

Koch, D and AD Del Genio (2010). 'Black carbon semi-direct effects on cloud cover: review and synthesis.' In: *Atmospheric Chemistry & Physics* 10.16.

Krüger, Olaf, Roman Marks and Hartmut Graßl (2004). 'Influence of pollution on cloud reflectance'. In: *Journal of Geophysical Research: Atmospheres* 109.D24.

Lamb, Dennis and Johannes Verlinde (2011). *Physics and chemistry of clouds*. Cambridge University Press.

Leckner, Bo (1978). 'The spectral distribution of solar radiation at the earth's surface—elements of a model'. In: *Solar energy* 20.2, pp. 143–150.

Liley, JB (2009). 'New Zealand dimming and brightening'. In: *Journal of Geophysical Research: Atmospheres* 114.D10.

Long, Charles N et al. (2009). 'Significant decadal brightening of downwelling shortwave in the continental United States'. In: *Journal of Geophysical Research: Atmospheres* 114.D10.

Matuszko, Dorota (2012). 'Influence of the extent and genera of cloud cover on solar radiation intensity'. In: *International Journal of climatology* 32.15, pp. 2403–2414.

McDuffie, Erin E et al. (2020). 'A global anthropogenic emission inventory of atmospheric pollutants from sector-and fuel-specific sources (1970–2017): An application of the Community Emissions Data System (CEDS)'. In: *Earth System Science Data Discussions*, pp. 1–49.

Meehl, Gerald A et al. (2000). 'The coupled model intercomparison project (CMIP)'. In: *Bulletin of the American Meteorological Society* 81.2, pp. 313–318.

Mishchenko, Michael I et al. (2007). 'Long-term satellite record reveals likely recent aerosol trend'. In: *Science* 315.5818, pp. 1543–1543.

Mitchell, JFB, CA Senior and WJ Ingram (1989). 'C02 and climate: A missing feedback'. In: *Nature* 341, pp. 132–134.

Moseid, Kine Onsum et al. (2020). 'Bias in CMIP6 models compared to observed regional dimming and brightening trends (1961–2014)'. In: *Atmospheric Chemistry and Physics Discussions*, pp. 1–20.

Myhre, G, CEL Myhre et al. (2013). 'Aerosols and their relation to global climate and climate sensitivity'. In: *Nature Education Knowledge* 4.5, p. 7.

Myhre, G., D. Shindell et al. (2013). 'Anthropogenic and Natural Radiative Forcing'. In: *Climate Change 2013: The Physical Science Basis. Contribution of Working Group I to the Fifth Assessment Report of the Intergovernmental Panel on Climate Change*. Ed. by T.F. Stocker et al. Cambridge, United Kingdom and New York, NY, USA: Cambridge University Press. Chap. 8, pp. 659–740. ISBN: ISBN 978-1-107-66182-0. DOI: **10.1017/CBO9781107415324.018**. URL: www.climatechange2013.org.

NASA (1999). 'Clouds and the Energy Cycle'. In: *The Earth Science Enterprise Series, August*.

NCAR (2017). *TBASE global digital elevation data (*$0.5^\circ \times 0.5^\circ$*)*. URL: http://research.jisao.washington.edu/data_sets/elevation/.

Norris, JR, RJ Allen et al. (2016). 'Evidence for climate change in the satellite cloud record'. In: *Nature* 536.7614, pp. 72–75.

Norris, JR and Martin Wild (2007). 'Trends in aerosol radiative effects over Europe inferred from observed cloud cover, solar "dimming," and solar "brightening"'. In: *Journal of Geophysical Research: Atmospheres* 112.D8.

— (2009). 'Trends in aerosol radiative effects over China and Japan inferred from observed cloud cover, solar "dimming," and solar "brightening"'. In: *Journal of Geophysical Research: Atmospheres* 114.D10.

Ohmura, Atsumu and Herbert Lang (1989). *IRS'88: Current Problems in Atmospheric Radiation: Secular variation of global radiation in Europe*.

Parding, Kajsa (2014). 'Decadal solar irradiance variability in northern Europe'. In:

Pfeifroth, Uwe et al. (2018). 'Trends and variability of surface solar radiation in Europe based on surface-and satellite-based data records'. In: *Journal of Geophysical Research: Atmospheres* 123.3, pp. 1735–1754.

Rossow, William B and Robert A Schiffer (1999). 'Advances in understanding clouds from ISCCP'. In: *Bulletin of the American Meteorological Society* 80.11, pp. 2261–2288.

Russak, V (1990). 'Trends of solar radiation, cloudiness and atmospheric transparency during recent decades in Estonia'. In: *Tellus B* 42.2, pp. 206–210.

Sanchez-Lorenzo, Arturo et al. (2009). 'Dimming/brightening over the Iberian Peninsula: Trends in sunshine duration and cloud cover and their relations with atmospheric circulation'. In: *Journal of Geophysical Research: Atmospheres* 114.D10.

Schwarz, Matthias et al. (2020). 'Changes in atmospheric shortwave absorption as important driver of dimming and brightening'. In: *Nature Geoscience* 13.2, pp. 110–115.

SEDAC, NASA (2017). *GRUMP dataset for urban/rural areas*. DOI: http://dx.doi.org/10.7927/H4MW2F2J.

Sliggers, Johan, Willem Kakebeeke and United Nations (2004). 'Clearing the air: 25 years of the Convention on Long-range Transboundary Air Pollution'. In:

Smirnov, Sergey (2015). 'Economic Fluctuations in Russia (from the late 1920s to 2015)'. In: *Russian Journal of Economics* 1.2, pp. 130–153.

Smith, Steven J et al. (2015). 'A Community Emissions Data System (CEDS): Emissions For CMIP6 and Beyond'. In: *Proceedings of the 2015 International Emission Inventory Conference, San Diego, CA, USA*, pp. 12–16.

Soni, VK, G Pandithurai and DS Pai (2016). 'Is there a transition of solar radiation from dimming to brightening over India?' In: *Atmospheric Research* 169, pp. 209–224.

Stanhill, G and S Cohen (2001). 'Global dimming: a review of the evidence for a widespread and significant reduction in global radiation with discussion of its probable causes and possible agricultural consequences'. In: *Agricultural and forest meteorology* 107.4, pp. 255–278.

Stanhill, G and JD Kalma (1995). 'Solar dimming and urban heating at Hong Kong'. In: *International Journal of Climatology* 15.8, pp. 933–941.

Stanhill, G and S Moreshet (1994). 'Global radiation climate change at seven sites remote from surface sources of pollution'. In: *Climatic Change* 26.1, pp. 89–103.

Stanhill, Gerald, Ori Achiman et al. (2014). 'The cause of solar dimming and brightening at the Earth's surface during the last half century: Evidence from measurements of sunshine duration'. In: *Journal of Geophysical Research: Atmospheres* 119.18, pp. 10–902.

Stevens, Bjorn (2015). 'Rethinking the lower bound on aerosol radiative forcing'. In: *Journal of Climate* 28.12, pp. 4794–4819.

Storelvmo, Trude et al. (2018). 'Lethargic response to aerosol emissions in current climate models'. In: *Geophysical Research Letters* 45.18, pp. 9814–9823.

Streets, David G, Ye Wu and Mian Chin (2006). 'Two-decadal aerosol trends as a likely explanation of the global dimming/brightening transition'. In: *Geophysical Research Letters* 33.15.

Sullivan, Timothy J et al. (2018). 'Air pollution success stories in the United States: The value of long-term observations'. In: *Environmental science & policy* 84, pp. 69–73.

Swinehart, Donald F (1962). 'The beer-lambert law'. In: *Journal of chemical education* 39.7, p. 333.

Twomey, Sean (1977). 'The influence of pollution on the shortwave albedo of clouds'. In: *Journal of the atmospheric sciences* 34.7, pp. 1149–1152.

Wakamatsu, Shinji, Tazuko Morikawa and Akiyoshi Ito (2013). 'Air Pollution Trends in Japan between 1970 and 2012 and Impact of Urban Air Pollution Countermeasures.' In: *Asian Journal of Atmospheric Environment (AJAE)* 7.4.

Wang, Yawen and Martin Wild (2016). 'A new look at solar dimming and brightening in China'. In: *Geophysical Research Letters* 43.22, pp. 11–777.

Waskom, Michael et al. (Sept. 2017). *mwaskom/seaborn: v0.8.1 (September 2017)*. Version v0.8.1. DOI: **10.5281/zenodo.883859**. URL: https://doi.org/10.5281/zenodo.883859.

Wild, Martin (2009). 'Global dimming and brightening: A review'. In: *Journal of Geophysical Research: Atmospheres* 114.D10.

— (2012). 'Enlightening global dimming and brightening'. In: *Bulletin of the American Meteorological Society* 93.1, pp. 27–37.

— (2016). 'Decadal changes in radiative fluxes at land and ocean surfaces and their relevance for global warming'. In: *Wiley Interdisciplinary Reviews: Climate Change* 7.1, pp. 91–107.

— (2nd Nov. 2020). Personal communication.

Wild, Martin, Doris Folini, Maria Z Hakuba et al. (2015). 'The energy balance over land and oceans: an assessment based on direct observations and CMIP5 climate models'. In: *Climate Dynamics* 44.11-12, pp. 3393–3429.

Wild, Martin, Doris Folini, Christoph Schär et al. (2013). 'The global energy balance from a surface perspective'. In: *Climate dynamics* 40.11-12, pp. 3107–3134.

Wild, Martin, Hans Gilgen et al. (2005). 'From dimming to brightening: Decadal changes in solar radiation at Earth's surface'. In: *Science* 308.5723, pp. 847–850.

Wild, Martin, Atsumu Ohmura et al. (2017). 'The Global Energy Balance Archive (GEBA) version 2017: A database for worldwide measured surface energy fluxes'. In: *Earth System Science Data* 9.2, pp. 601–613.

Willson, Richard C and Alexander V Mordvinov (2003). 'Secular total solar irradiance trend during solar cycles 21–23'. In: *Geophysical Research Letters* 30.5.

WMO (2008). 'Measurement of sunshine duration'. In:

Yang, Su, Xiaolan L Wang and Martin Wild (2018). 'Homogenization and trend analysis of the 1958–2016 in situ surface solar radiation records in China'. In: *Journal of Climate* 31.11, pp. 4529–4541.

Zerefos, CS et al. (2009). 'Solar dimming and brightening over Thessaloniki, Greece, and Beijing, China'. In: *Tellus B: Chemical and Physical Meteorology* 61.4, pp. 657–665.